Study of the Velocity Dependence of the Adiabatic Rapid Passage (ARP) Optical Force in Helium

A Dissertation Presented

by

John David Elgin

to

The Graduate School

in Partial Fulfillment of the Requirements

for the Degree of

Doctor of Philosophy

in

Physics and Astronomy

Stony Brook University

August 2015

Stony Brook University

The Graduate School

John David Elgin

We, the dissertation committee for the above candidate for the Doctor of Philosophy degree, hereby recommend acceptance of this dissertation.

Harold Metcalf – Dissertation Advisor
Distinguished Teaching Professor, Department of Physics and Astronomy

Matthew Dawber – Chairperson of Defense
Associate Professor, Department of Physics and Astronomy

Tzu-Chieh Wei
Assistant Professor, Department of Physics and Astronomy

Trevor Sears
Professor, Department of Chemistry
Stony Brook University

This dissertation is accepted by the Graduate School.

Charles Taber
Dean of the Graduate School

Abstract of the Dissertation

Study of the Velocity Dependence of the Adiabatic Rapid Passage (ARP) Optical Force in Helium

by

John David Elgin

Doctor of Philosophy

in

Physics and Astronomy

Stony Brook University

2015

The use of optical forces to precisely control the motion of atoms has played a major role in expanding the field of atomic physics. However, in a majority of experiments, these optical forces are limited in strength by the inherent properties of the chosen atoms, mainly the rates of spontaneous emission, required to return the atoms to their ground state. It has been shown that the process of absorption, followed by stimulated-emission, can be used to provide a more rapid return to the atomic ground state. Through careful design of the experiment, a coherent exchange of momentum can take place, exerting a large force on the atoms.

Adiabatic Rapid Passage (ARP) is a technique commonly used in the magnetic resonance community for the population inversion of a two-level spin system. This technique has been expanded to the optical regime and used to invert the electronic states of an atomic system, allowing for control over both absorption and stimulated emission. It has been previously demonstrated that this scheme can be used to generate large forces on stationary atoms.

An in-depth study of this ARP force will be presented with a strong emphasis on experiments designed to measure the dependence of the ARP force on atomic velocity. The experiments use the $2^3S \rightarrow 2^3P$ transition in Helium at $\lambda = 1.083\,\mu$m, and results show, that by using a properly-tailored pulse sequence, the ARP force can exerts a large force on atoms over a large velocity range, making it a potential candidate to decelerate neutral atomic (or molecular) beams

Numerical simulations of multiple ARP processes on two-level atoms were run with the hopes of gaining further insight into the subsequent force. These simulations have unveiled some interesting questions about the ARP process. These questions pertain to spontaneous emission's effect on the force and the influence of the phase of the optical pulses on the atomic state.

While the simulations exhibit some overall similarities with the experimental results quantitative agreement is generally poor. Explanation for this disagreement is presented along with a roadmap for future work.

For all those who have
supported, encouraged, and inspired me through my years.

Contents

List of Tables

List of Figures

Chapter 1

Introduction

Since its inception, laser cooling has been a powerful tool in the atomic physics community. It has many profound uses ranging from high resolution spectroscopy to atomic clocks. It has been used to observe exotic phases in dilute ultra cold atomic gases including Bose-Einstein Condensates (BEC) [1–4]. All of these experiments rely on the radiative force derived from momentum exchange between the atoms and the light field. This can slow the atoms and then optical molasses can be used to begin the cooling process, a concept first proposed in the late 1970's and put into practice in the early 1980's [5–10]. For both slowing and cooling, the force relies on spontaneous emission to return an optically excited atom to its ground state, and as such this rate of return limits the strength of the force.

As the field of atomic physics has grown there has been greater interest in the miniaturization of cold atom experiments and also a desire to create cold molecules. The pursuit of miniaturization is also limited by the spontaneous decay rate of the chosen atoms. However, recent experiments have shown that a process of absorption followed by stimulated emission can be used to provide a more rapid return of the atom to its ground state. These experiments make use of polychromatic light and have shown that optical forces much stronger than the standard radiative force are achievable [11–14]. These forces are of interest to the atomic physics community, because they not only exert strong forces on atoms over a short interaction length, but also they tend to interact with atoms over a larger velocity range. They are a fully stimulated process and do not require a "cycling transition". As such, they are good candidates for the laser cooling of molecules [15, 16].

This thesis will present the work performed in the study of the adiabatic rapid passage

(ARP) optical force with a strong emphasis on the velocity dependence of this force. It is worth noting though that while the experiment was designed to measure the velocity dependence, the work has unearthed many questions related to the ARP process, outside of the scope of the initial goal. Chapter 1 will establish the fundamentals necessary to understand the work starting from the theory of a two-level atom and progressing to an overview of optical forces. Chapter 2 will look closely at the theory behind ARP, how a force results from ARP, and the effect of multiple ARP sequences on a two-level system. Chapter 3 will outline the vacuum and optical system used in the experiments, while Chapter 4 will outline how the experimental velocity-dependent measurements were performed. Chapter 5 will outline the numerical simulations of the ARP process and present some interesting results. Finally, Chap. 6 will present the latest experimental results compare them to the numerical simulations. It will also lay out future directions for ARP experiments, based on these results.

1.1 Two-Level Atom

The two-level atom model provides a simple yet powerful means of analyzing atom-light interactions. This section will develop this model starting from the time-dependent Schrödinger equation (TDSE) and present some of the information that results from the analysis. This work closely follows the derivations done in Ref. [17].

Starting with the TDSE and assuming only that the light field is a classical electromagnetic wave, then

$$\mathcal{H}\Psi(\mathbf{r},t) = i\hbar\frac{\partial}{\partial t}\left(\Psi(\mathbf{r},t)\right) \tag{1.1}$$

$$\mathcal{H} = \mathcal{H}_0 + \mathcal{H}'(t) \tag{1.2}$$

where $\mathcal{H}_0$ is the field-free atomic Hamiltonian and $\mathcal{H}'(t)$ describes the interaction with the light field. Following the steps in [17], the TDSE can be rewritten into the form

$$i\hbar\frac{d}{dt}\left(c_j(t)\right) = \sum_k c_k(t)\mathcal{H}'_{jk}(t)e^{i\omega_{jk}t} \tag{1.3}$$

At this point this is an exact solution to the TDSE. However, in order to obtain an analytical

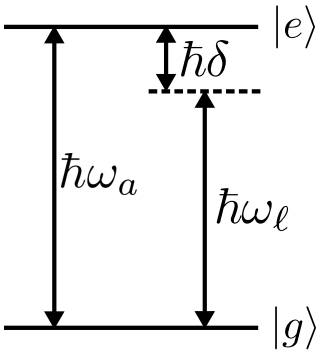

Figure 1.1: Energy level diagram of a two-level atom showing the energy separation $\hbar\omega_a$ between the ground state $|g\rangle$ and excited state $|e\rangle$. The laser's energy is given by $\hbar\omega_\ell$ and it can be detuned $\delta \equiv \omega_\ell - \omega_a$ from the atomic resonance. Modified from [18].

solution it is necessary to make some approximations based on the system being solved.

1.1.1 Rabi Oscillations

Consider a two-level system like the one depicted in Fig. 1.1. For this system, the the TDSE reduces to the follow coupled differential equations

$$i\hbar\dot{c_g}(t) = c_e(t)\mathcal{H}'_{ge}(t)e^{-i\omega_a t} \tag{1.4a}$$

$$i\hbar\dot{c_e}(t) = c_g(t)\mathcal{H}'_{eg}(t)e^{i\omega_a t} \tag{1.4b}$$

where ω_a is the atomic resonance frequency, and $\mathcal{H}'_{ge} \equiv \langle g|\mathcal{H}'(t)|e\rangle$. By replacing the momentum in $\mathcal{H}(t)$ with the canonical momentum, $p \to p + (e/c)\,\mathbf{A}(\mathbf{r},t)$, where $\mathbf{A}(\mathbf{r},t)$ is the vector potential of the field. Then the resulting Hamiltonian will have two parts, a time independent part, $\mathcal{H}_0 = \frac{p^2}{2m} + V$, and a time dependent part

$$\mathcal{H}'(t) = -\,e\mathcal{E}(\mathbf{r},t)\cdot\mathbf{r} = -\mathbf{d}\cdot\mathcal{E}(\mathbf{r},\mathbf{t}) \tag{1.5}$$

here $\mathcal{E} = \frac{1}{c}\frac{d\mathbf{A}}{dt}$ is defined as the electric field which couples the two levels together [19, 20].

Assuming that the light is a plane wave traveling in the z direction, then the electric field operator $\mathcal{E}$ has the form $\mathcal{E}(\mathbf{r},t) = \mathrm{E}_0\hat{\epsilon}\cos(\omega_\ell t - \mathbf{k}\cdot\mathbf{z})\,\mathrm{e}^{-i\phi}$ and the time-dependent

Hamiltonian becomes $\mathcal{H}'_{ge} = \hbar\Omega\cos(\omega_\ell t - \mathbf{k}\cdot\mathbf{z})\,\mathrm{e}^{-i\phi}$ where

$$\Omega \equiv -\frac{e\mathrm{E}_0}{\hbar}\langle e|\mathbf{r}|g\rangle \tag{1.6}$$

is the Rabi frequency. Substituting this into Eq. 1.4 and dropping the $\mathbf{k}\cdot\mathbf{z}$ term, results in the following

$$\dot{c_g}(t) = -i\frac{\Omega\mathrm{e}^{-i\phi}}{2}\left(\mathrm{e}^{-i\omega_\ell t} + \mathrm{e}^{i\omega_\ell t}\right)\mathrm{e}^{-i\omega_a t}c_e(t) \tag{1.7a}$$

$$\dot{c_e}(t) = -i\frac{\Omega^*\mathrm{e}^{i\phi}}{2}\left(\mathrm{e}^{-i\omega_\ell t} + \mathrm{e}^{i\omega_\ell t}\right)\mathrm{e}^{i\omega_a t}c_g(t) \tag{1.7b}$$

Looking at Eqs. 1.7 it can be seen that there are two distinct time scales at which the solutions oscillate; the fast $\mathrm{e}^{\pm(\omega_\ell+\omega_a)t}$ and the slow $\mathrm{e}^{\pm(\omega_\ell-\omega_a)t}$. The rotating wave approximation (RWA) treats these oscillatory terms differently based on the timescale of typical experiments [21]. The fast oscillations occur on a timescale which is much too quick for any experiment ($\sim 10^{15}\,\mathrm{Hz}$), and therefore are assumed to average to zero. Meanwhile the slowly oscillating term has a timescale which is relevant to an experiment (up to a few hundred MHz) and thus will be considered in the approximation.

After making the RWA the coupled equations (Eq. 1.4) become

$$\dot{c}_g(t) = -\frac{i}{2}\Omega\mathrm{e}^{-i\phi}c_e(t)\mathrm{e}^{-i\delta t} \tag{1.8a}$$

$$\dot{c}_e(t) = -\frac{i}{2}\Omega\mathrm{e}^{i\phi}c_g(t)\mathrm{e}^{i\delta t} \tag{1.8b}$$

where $\delta \equiv \omega_\ell - \omega_a$. These two equations can be decoupled by differentiating the first one and substituting it into the second equation thus arriving at

$$\ddot{c}_g(t) - i\delta\dot{c}_g(t) + \frac{|\Omega|^2}{4}c_g(t) = 0 \tag{1.9}$$

and similarly

$$\ddot{c}_e(t) + i\delta\dot{c}_e(t) + \frac{|\Omega|^2}{4}c_e(t) = 0 \tag{1.10}$$

Solving these equations for the initial conditions $c_g(0) = 1$ and $c_e(0) = 0$, leads to the following

$$c_g(t) = \left(\cos\frac{\Omega' t}{2} - i\frac{\delta}{\Omega'}\sin\frac{\Omega' t}{2}\right)\mathrm{e}^{i\delta t/2} \tag{1.11a}$$

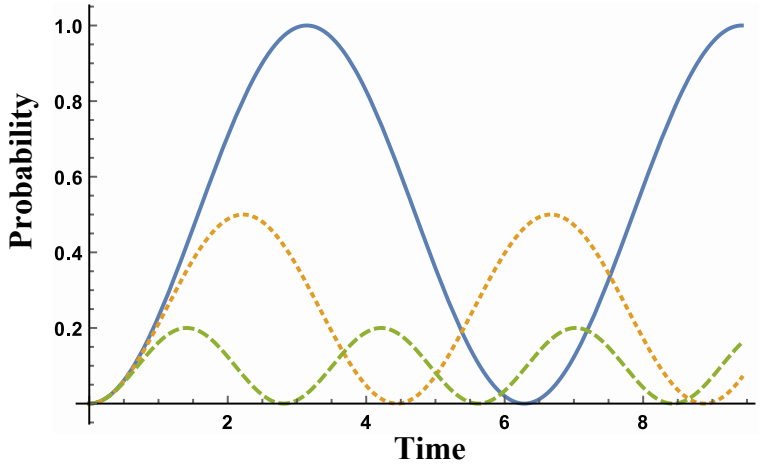

Figure 1.2: Plot of the probability of an atom to found be in the excited state, $|c_e(t)|^2$, *vs.* time. The solid line corresponds to $\delta = 0$, the dotted line to $\delta = |\Omega|$, and the dashed to $\delta = 2|\Omega|$. The time is plotted in units of $1/|\Omega|$.

$$c_e(t) = -i\frac{\Omega e^{i\phi}}{\Omega'} \sin\frac{\Omega' t}{2} e^{-i\delta t/2} \tag{1.11b}$$

where $\Omega' \equiv \sqrt{|\Omega|^2 + \delta^2}$ is the generalized Rabi frequency. Rabi oscillations are depicted in Fig. 1.2, which shows a plot of $|c_e(t)|^2$, the probability of the atom being found in the excited state, *vs.* time. It can be seen that the frequency of the oscillation is directly proportional to Ω', but the amplitude of the oscillation is inversely proportional to Ω'.

A point of interest is the case of resonant light ($\delta = 0$), and a pulse duration of $t = \pi/\Omega$. From Fig. 1.2 it can be seen that a pulse under this condition will result in a complete inversion of the population, $|c_e(t)|^2 = 1$, and is referred to as a π-pulse. A pulse whose duration is half that of a π-pulse will place the atom in an equal superposition of ground and excited states and is called a $\pi/2$-pulse.

1.1.2 The Bloch Sphere

Using the complex amplitudes c_g and c_e defined in Sec. 1.1.1, the full density matrix, ρ, can be written as

$$\rho = |\psi\rangle\langle\psi| = \begin{pmatrix} |c_g|^2 & c_g c_e^* e^{i\phi} \\ c_e e^{-i\phi} c_g^* & |c_e|^2 \end{pmatrix} = \begin{pmatrix} \rho_{gg} & \rho_{ge} \\ \rho_{eg} & \rho_{ee} \end{pmatrix} \tag{1.12}$$

A novel way of looking at the time evolution of the density matrix was first done by Feynman, Vernon, and Hellswarth [22]. They considered a change of variables to a rotating coordinate system and arrived at a state vector $\mathbf{R}$, the Bloch vector, whose components $\{u, v, w\}$ are given by

$$u = \rho_{eg} + \rho_{ge} = 2\mathrm{Re}\left[\mathrm{c_g(t)c_e^*(t)}\right]\cos\phi(\mathrm{t}) \tag{1.13a}$$

$$v = i\left(\rho_{ge} - \rho_{eg}\right) = 2\mathrm{Im}\left[\mathrm{c_g(t)c_e^*(t)}\right]\sin\phi(\mathrm{t}) \tag{1.13b}$$

$$w = \rho_{ee} - \rho_{gg} = |c_e(t)|^2 - |c_g(t)|^2 \tag{1.13c}$$

This is a convenient coordinate system to use because $|\mathbf{R}(t)| = 1$, it can be pictorially represented on unit sphere, called the Bloch sphere. The south pole of the Bloch sphere represents the ground state of the system, the north pole the excited state, and any other point some superposition of the two.

The time dependence of $\mathbf{R}$ calculated from the TDSE is given by

$$\frac{d\mathbf{R}}{dt} = \mathbf{\Omega} \times \mathbf{R} \tag{1.14}$$

where $\mathbf{\Omega}$ is called the torque vector and its components are $\{\Omega_{\mathrm{real}}, \Omega_{\mathrm{imag}}, -\delta\}$. Ω_{real} is the real part of the Rabi frequency, Ω_{imag} is the imaginary part. Equation 1.14 is nothing more than a rewriting of Eq. 1.8 in terms of the Bloch vector.

1.1.3 The Optical Bloch Equations

In order to expand the Bloch vector model, Sec. 1.1.2, to better represent a two-level atomic system, it is necessary to include a decay term. This decay term can take the form of either collisions or spontaneous decay. Given the nature of the experiments performed in this work, collisions are extremely unlikely and as such will be neglected. As for spontaneous emission, one way of handling it is to treat it as a special type of inelastic collision, in which dephasing or loss of coherence can occur along with a change in the internal energy state of the atom [21].

Through proper treatment of spontaneous emission, the time dependence of $\mathbf{R}$ can be written as

$$\dot{u} = \Omega_{\mathrm{imag}} w - \delta v - (\gamma/2)\, u \tag{1.15a}$$

$$\dot{v} = -\Omega_{\mathrm{real}} w + \delta u - (\gamma/2)\, v \tag{1.15b}$$

$$\dot{w} = \Omega_{\text{real}} v - \Omega_{\text{imag}} u - \gamma(w+1) \tag{1.15c}$$

where γ is the spontaneous emission decay rate for the excited state. These equations are commonly referred to as the Optical Bloch Equations (OBEs).

1.2 Optical Forces

The basic physics behind optical forces is straightforward. An atom of mass M undergoes absorption of resonant light with frequency $\omega_\ell/2\pi$. It is required that both conservation of energy and momentum be upheld during this process. The absorbed energy from the light field $\hbar\omega_\ell$ goes into the excitation of the atom's internal state, thereby conserving energy. The angular momentum of the light, $\hbar$, is transferred to the orbital motion of the electron. The linear momentum $\hbar\omega_\ell/c \equiv \hbar k$ is transferred to the translational motion of the atom, resulting in a velocity change $\hbar k/\text{M} \sim$ few cm/s. The strength of the force is based on how quickly this process can be repeated over a given time interval, and thus it is limited by the rate at which the atom returns to its ground state. The following sections discuss some schemes which exploit this property of the atom-light interaction.

1.2.1 The Radiative Force

The radiative force is the simplest of the optical forces. For a stationary atom in a low intensity, traveling wave laser field, the atom will have a high probability to absorb the light of the field if the frequency corresponds to the energy separation between the ground state and another internal state. This absorption will impart a momentum kick, $p = \hbar\omega_\ell/c = \hbar k$, to the atom along the direction of the laser propagation. Due to the low intensity, the laser will have little influence on the excited atom until such time as the atom undergoes a spontaneous emission event and returns to the ground state. Spontaneous emission of an atom in vacuum is symmetric over many spontaneous emission events, therefore any momentum imparted to the atom due to the emission will average to 0 over many lifetimes. As such after a large number of cycles the net momentum change is therefore only in the direction the light is traveling. Figure 1.3 depicts one cycle of this process.

To quantify this process, it is necessary start by writing the force as

$$\mathbf{F}_{\text{rad}} = \hbar\mathbf{k}\gamma \left|c_e(t)\right|^2 \tag{1.16}$$

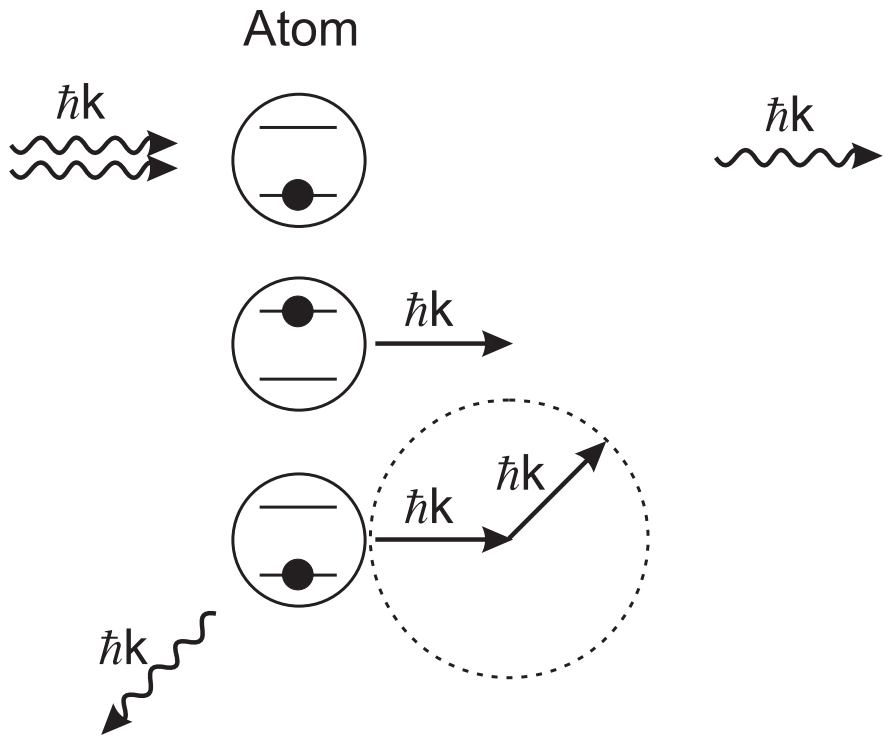

Figure 1.3: Diagram showing the step-by-step process of the radiative force through up to one spontaneous emission event. To start, an atom in the ground state absorbs light and is driven to the excited state, receiving a momentum kick of $\hbar k$ in the direction the light is traveling. After some time, the atom will undergo spontaneous emission, emitting light in a random direction and as the light is emitted the atom will recoil in the opposite direction to allow for momentum conservation. This process when repeated a large number times results only in a net momentum change in the direction of the light. Taken from [23]

where γ and $|c_e(t)|^2$ are previously defined. The force can also be written as [17]

$$\mathbf{F}_{\text{rad}} = \frac{\hbar k s_0 \gamma/2}{1 + s_0 + (2\delta/\gamma)^2} \tag{1.17}$$

where s_0 is the saturation parameter given by

$$s_0 = 2\left(\frac{|\Omega|}{\gamma}\right)^2 = \frac{I}{I_{\text{sat}}} \tag{1.18}$$

with the saturation intensity $I_{\text{sat}} \equiv \pi hc/3\lambda^3\tau$. As the intensity of the light increases, the

force will eventually saturate to a maximum of

$$\mathbf{F}_{\mathrm{rad,max}} = \hbar k\gamma/2. \tag{1.19}$$

This is valid for stationary atoms. However, to make use of the radiative force for cooling and trapping, it is necessary to consider moving atoms. An atom moving with velocity $\mathbf{v}$ in the lab frame will experience a Doppler shift given by $\omega_{\mathrm{D}} = -\mathbf{k}\cdot\mathbf{v}$, which will modify the radiative force in the following way:

$$\mathbf{F}_{\mathrm{rad}} = \hbar\mathbf{k}\frac{s_0\gamma/2}{1+s_0+\left(2\left(\delta-\mathbf{k}\cdot\mathbf{v}\right)/\gamma\right)^2}. \tag{1.20}$$

Here the δ in Eq. 1.17 has been replaced by an "effective detuning", $\delta - \mathbf{k}\cdot\mathbf{v}$. In this case the force is maximum for atoms having a velocity $\mathbf{v} = \delta\mathbf{k}/k^2$.

When an atom's velocity is opposite the direction of the light the radiative force will oppose the atomic motion. Because of this, the radiative force is a useful tool for the slowing of atomic beams. However, as the atom's velocity changes, the resonance condition will change due to the Doppler shift, so it is necessary to use some scheme to compensate for this change. One commonly used method to compensate for the Doppler shift is to use the Zeeman effect to make up for the changing resonance condition [7]. Other similar methods are covered in more detail in [17].

Besides slowing, the radiative force can also be used to cool atoms under certain conditions. In the low intensity limit, $s_0 \sim 1$, the force felt on an atom by two counter-propagating beams can be added together, resulting in a force which can be expressed as

$$\begin{aligned}\mathbf{F} =& \hbar\mathbf{k}\frac{\gamma s_0/2}{1+s_0+\left(2\left(\delta-\mathbf{k}\cdot\mathbf{v}\right)/\gamma\right)^2} - \hbar\mathbf{k}\frac{\gamma s_0/2}{1+s_0+\left(2\left(\delta+\mathbf{k}\cdot\mathbf{v}\right)/\gamma\right)^2} \\ \approx& \frac{8\hbar k^2\delta s_0\mathbf{v}}{\gamma\left(1+s_0+\left(2\delta/\gamma\right)^2\right)2}.\end{aligned} \tag{1.21}$$

For the case of red detuning ($\delta < 0$) the force will oppose the atom's motion and pushes the atom towards $\mathbf{v} = 0$, this is commonly referred to as optical molasses due to the viscous drag exerted on the atoms. Figure 1.4 depicts the force *vs.* velocity profile of optical molasses, for the case where $s_0 = 2$ and $\delta = -\gamma$. Atoms within the capture range, $|v| < \gamma/k$, will experience a force which quickly brings the average velocity to near $\mathbf{v} = 0$. The temperature

of the atoms will not reach $T = 0$, due to the discrete momentum exchanges that take place. For atoms typically used in atomic physics experiments, the cooled temperature limit is $\sim 100\,\mu$K [6].

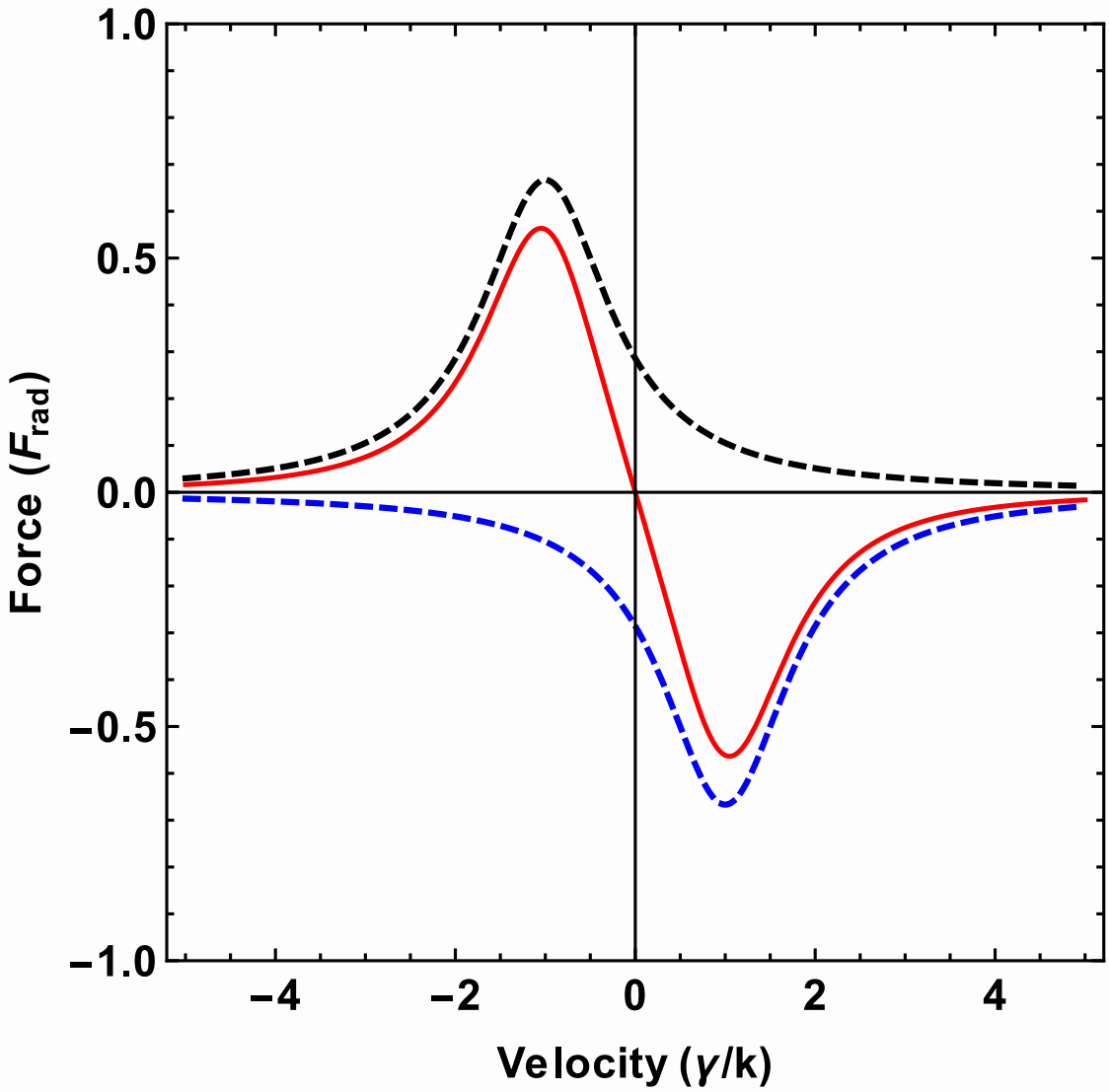

Figure 1.4: The force *vs.* velocity profile for optical molasses with parameters, $s_0 = 2$ and $\delta = -\gamma$. The dashed lines show the profile for the radiative force considering only light from each direction, and the solid line shows the combination of the two. In the region $|v| < \gamma/k$ the atom feels a restoring force which opposes its motion and drives it towards zero velocity.

1.2.2 The Dipole Force

The next optical force to be discussed is the dipole force. The dipole force differs from the radiative force in that it does not rely upon spontaneous emission. Instead, it results from the coherent exchange of momentum due to the absorption of light from one light field and the stimulated emission into a different light field.

Consider a two-level atom present in an optical field. For the case of $\delta \gg \Omega$, the ground state energy level will be shifted due to the light shift as shown in [17] by

$$\Delta E_g = \frac{\hbar \Omega^2}{4\delta}. \tag{1.22}$$

For an atom in single-frequency standing wave, these energy levels will be spatially modulated following the variation in the intensity of the light field. The dipole force is proportional to the gradient of this light shift,

$$F_{\text{dip}} = -\nabla(\Delta E_g). \tag{1.23}$$

For a standing wave, the intensity is given by $I(z) = I_0 \cos^2(kz)$, and using Eq. 1.18, the dipole force is,

$$F_{\text{dip}} = \frac{\hbar k \gamma^2 I_0}{8\delta I_{\text{sat}}} \sin(2kz) \tag{1.24}$$

where z is the position of the atom. The magnitude of the force does not saturate and is limited only by the intensity of the light which drives the process. However, it is not without its downside, as a closer examination shows that the spatial dependence of the force is oscillatory and will average to 0 over a full wavelength. Because of the symmetry of the standing wave, the dipole force can be used only to trap atoms, it is unable to cool atoms because the force is inherently conservative.

1.2.3 The Polychromatic Force

The large magnitude of the dipole force is of great interest to the AMO community, because its ability to exert strong forces over a short period of time opens up the possibility of miniaturization of the typically large and unwieldy laser cooling experiments. However, as stated above, it is necessary to come up with a mechanism to break the symmetry of the process. There are many different schemes devised to do this, but this section will address two of those which accomplish the goal through the use of polychromatic light.

The first of these polychromatic forces, the bichromatic force, involves simply the addition of a second frequency. For a full discussion of the bichromatic force see Ref. [18, 24–27], but here a simple discussion will be given. To start with, consider two counter-propagating beams each containing two frequencies, $\omega_\ell \pm \delta$ with $\omega_\ell \gg \delta \gg \gamma$. The addition of these two frequencies results in each beam being a train of pulses of length π/δ whose carrier frequency is at the average between the two frequencies in the beam, ω_ℓ. By carefully setting the Rabi frequency of each frequency component, these pulse can satisfy the π-pulse condition.

By setting the phase (time delay) of each pulse train, such that one pulse excites the atom while another pulse from the opposite direction causes stimulated emission returning the atom to the ground state. Because the absorption and stimulated emission occur in opposite directions, the resulting momentum kicks will be additive and lead to a momentum change of $2\hbar k$ over a time period of π/δ, producing a total force of $F_{\text{bichro}} = 2\hbar k\delta/\pi$. See Fig. 1.5 for a diagram of the bichromatic force setup. It can be seen that for $\delta \gg \gamma$ this force is much greater than that of the radiative force, F_{rad}. Many of the specific details and difficulties with the bichromatic force are not covered here but are covered in greater depth in Ref. [18, 28].

If the Bichromatic force is the next logical step from monochromatic light, then on the other extreme is the Adiabatic Rapid Passage (ARP) force, which uses discrete pulses and a continuous frequency sweep to invert the atomic state. This force is the major topic of this thesis and as such, the theory and implementation will be discussed in great detail in the subsequent chapters.

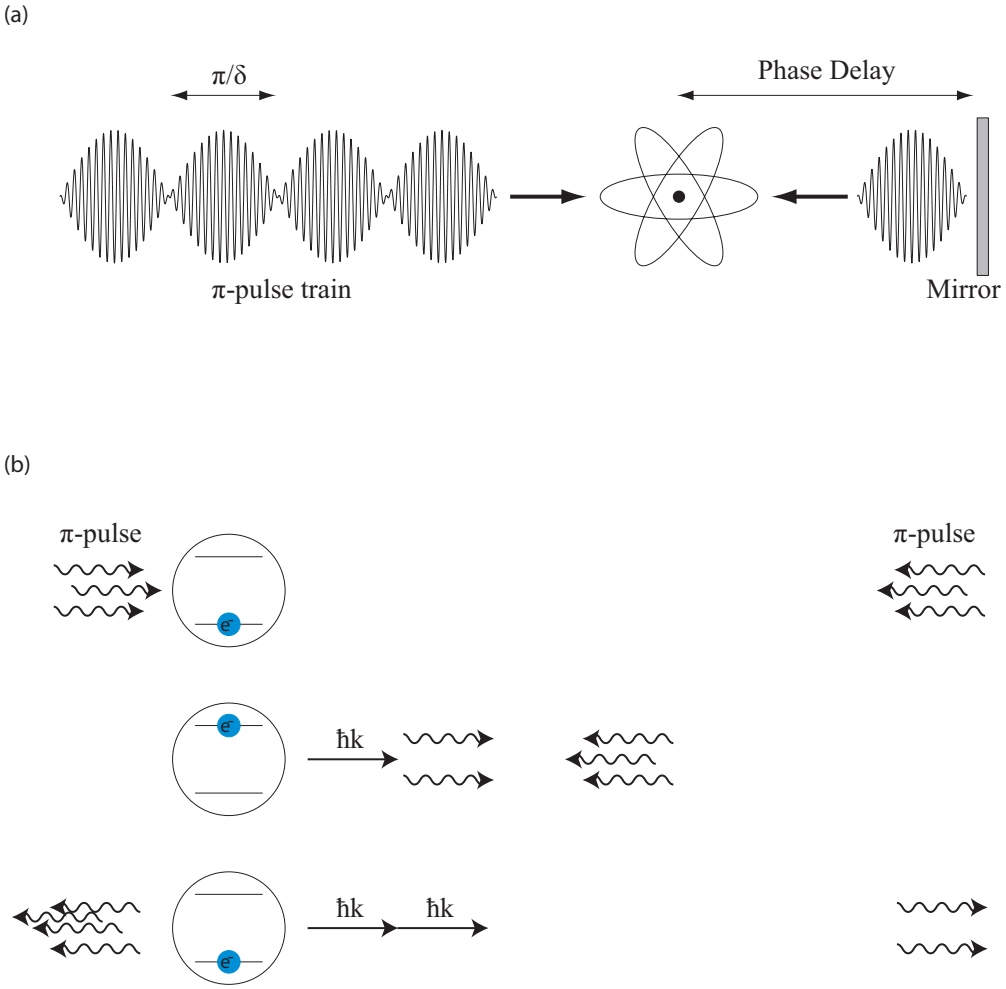

Figure 1.5: Diagram of the Bichromatic force. Part (a) shows train of pulses incident on an atom. The light is then retro-reflected off a mirror whose location is chosen such that it creates the proper delay between the pulses to allow that atom to see sequential pulses traveling in opposite directions. Part (b) depicts a single cycle of the absorption and stimulated emission process used to generate strong optical forces. Taken from [29].

Chapter 2

Adiabatic Rapid Passage (ARP)

2.1 Theory of ARP

Adiabatic rapid passage is a well known technique commonly used by the magnetic resonance community to invert spins in atoms or molecules [30]. In the atomic physics community ARP is commonly used to invert the population of a two-level system.

A way to visualize the ARP process is by looking at the energies of a two-level system in the dressed-atom picture. References [18, 23] provide a nice detailed explanation of the dressed atom picture, which can also be found in many other atomic physics textbooks. Thus the derivation will not be covered in this thesis.

The dressed-atom Hamiltonian for a two-level system can be written as:

$$\mathcal{H}(t) = \frac{\hbar}{2} \begin{pmatrix} \delta(t) & \Omega(t) \\ \Omega(t) & -\delta(t) \end{pmatrix}, \tag{2.1}$$

where $\delta(t)$, is the instantaneous detuning of the light, and $\Omega(t)$, is the instantaneous Rabi frequency. The eigenenergies of this Hamiltonian are $E(t)_{\pm} = \pm (\hbar/2) \sqrt{(\delta(t))^2 + (\Omega(t))^2}$. Figure 2.1 shows these eigenenergies and how they change with variation in $\Omega(t)$ and $\delta(t)$. An important feature of this picture is the energy ordering of the eigenstates. In the limit of $\Omega < |\delta|$ and $\delta > 0$ the upper eigenstate approaches the bare (no light shift) ground state, $|g\rangle$, while the lower eigenstate approaches the bare excited state, $|e\rangle$. However, for $\delta < 0$ these states are reversed. Away from the limit $\Omega < |\delta|$ these states are mixed on the two energy sheets.

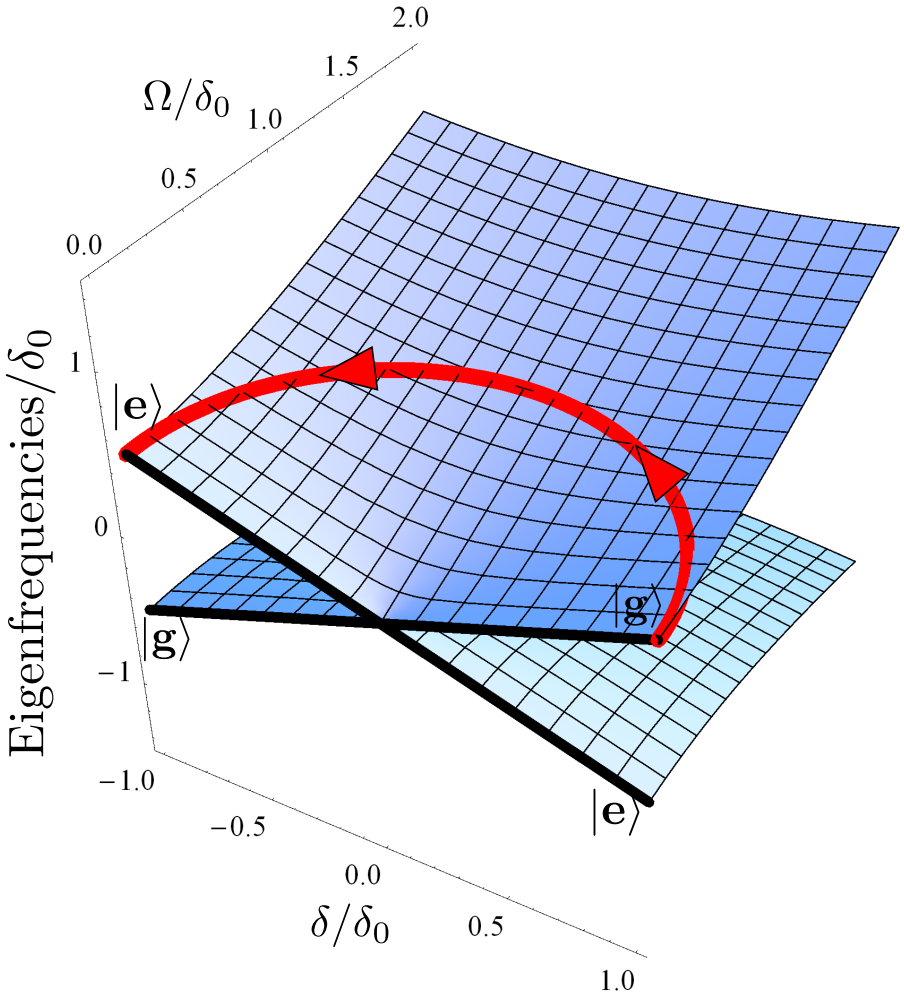

Figure 2.1: The dressed state energy sheets as a function of Ω and δ. At $\Omega = 0$ the upper sheet changes from $|g\rangle$ to $|e\rangle$ as δ changes sign. The curved path shows one possible trajectory for ARP.

The ARP process in the dressed-atom picture can be seen as a synchronized sweep of both the Rabi frequency and the detuning of the light, such that the state of the system follows along one of these eigenenergy sheets. A "slow enough" frequency sweep is necessary such that the the state of the two-level system will adiabatically follow one of the dressed eigenstates and result in an inversion of the population [31]. The curved path shown in Fig. 2.1, shows one such trajectory given by the experimentally-defined sweep profile $\delta(t) =$

$\delta_0 \cos(\omega_m t)$ and $\Omega(t) = |\Omega_0 \sin(\omega_m t)|$. If the process is not slow enough, the atom will not fully invert due to diabatic transitions, and the final state will be a superposition of both $|g\rangle$ and $|e\rangle$ states.

A second way to look at the ARP process is by observing the trajectory mapped out by the Bloch vector $\mathbf{R} = \{u, v, w\}$, on the Bloch sphere, when an atom interacts with ARP light [32]. For the case of ARP light, the torque vector, $\mathbf{\Omega}$, starts by pointing towards the south pole parallel with $\mathbf{R}$, for an atom starting in $|g\rangle$, and it is slowly swept to the north pole by symmetrically sweeping the detuning of the light from below to above atomic resonance. As this takes place, the Rabi frequency of the light starts at 0 and increases to a maximum when $\delta = 0$. It then returns to 0 at the end of the frequency sweep. Thus, the torque vector will follow a meridian of the Bloch sphere. The trajectory of the Bloch vector is governed by Eq. 1.14. For a "slow enough" sweep rate, the Bloch vector will adiabatically follow $\mathbf{\Omega}$ from the south pole to the north pole, while precessing around it in a spiral path, as shown in Fig. 2.2(a).

No matter the choice of pictures, ARP requires that the sweep rate, ω_m, be "slow enough" to allow for adiabatic following. A quantitative description of how slow is "slow enough" is given by,

$$|\mathbf{\Omega}| \gg \frac{d\theta(t)}{dt} \tag{2.2}$$

where $2\theta(t) \equiv \arctan(\Omega(t)/\delta(t))$[1], is called the mixing angle. This is the mixing angle of the eigenstates in the dressed-atom picture. Also, in the Bloch sphere picture, this can be viewed as the angle between $\mathbf{\Omega}$ and w-axis. This condition says that the angular frequency of torque vector must be small when compared to the angular frequency of the Bloch vector at all times. The "rapid" part of ARP assigns the condition that the ARP process must occur quickly when compared to the relaxation processes of the system. In an atomic system the natural relaxation process is the spontaneous decay rate, γ. For this reason ARP is typically used in the parameter space given by

$$\delta_0 \sim \Omega_0 \gg \omega_m \gg \gamma, \tag{2.3}$$

where δ_0 is the amplitude of the frequency sweep, Ω_0 is the peak Rabi frequency, ω_m is the modulation frequency, and γ is the spontaneous decay rate. This inequality defines a

[1]Note that Ref. [23] has this incorrectly defined.

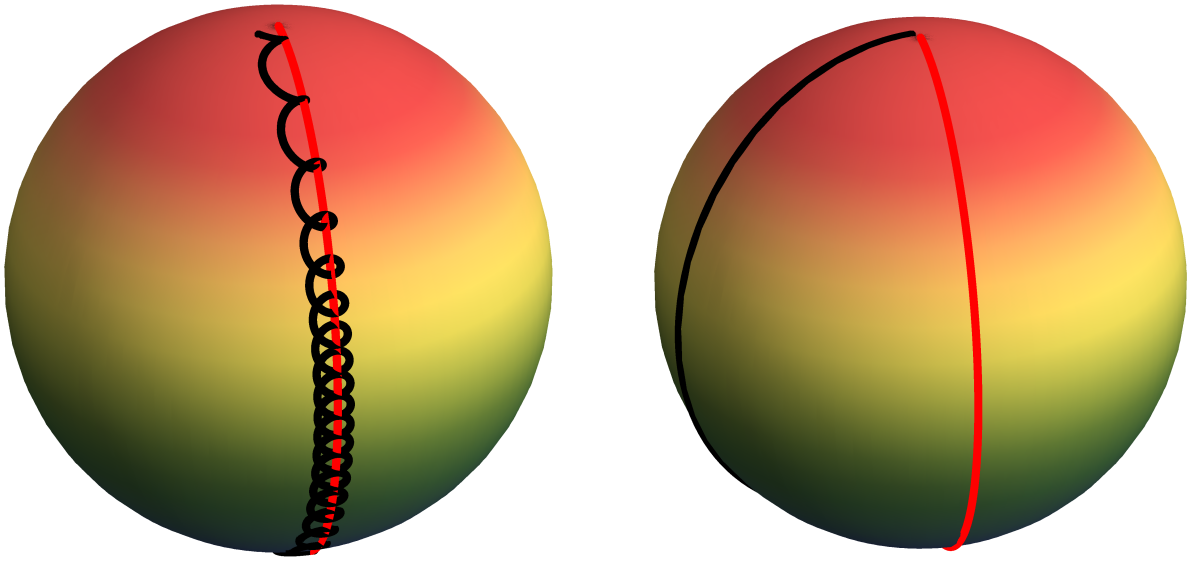

(a) (b)

Figure 2.2: A plot of the trajectories of the Bloch vector, $\mathbf{R}(t)$(black) and the torque vector $\mathbf{\Omega}(t)$(Grey/Red). Part (a) shows the trajectory for parameters which agree with Eq. 2.3, $\delta_0 = 30\ \omega_m$ and $\Omega_0 = 50\ \omega_m$. The path of $\mathbf{R}$ agrees with the intuitive picture of ARP, as it maps out a spiral path and precesses about $\mathbf{\Omega}$. Part (b) however, shows that even for experimentally accessible parameters ($\delta_0 = 1.10\ \omega_m$ and $\Omega_0 = 1.61\ \omega_m$), it is possible to achieve a population inversion. The path of $\mathbf{R}$ in this case is a simple arc which is $\sim 90°$ away from the path of $\mathbf{\Omega}$.

parameter space for which ARP is considered most robust.

2.1.1 The ARP Force

The ARP force arises from a sequence of absorption and stimulated emission events, similar to part (b) of Fig. 1.5, where the role of ARP is to invert the state, with a high fidelity, at each step in the process. The calculation of the force on an atom starts with the Ehrenfest theorem [33].

$$\mathbf{F} = \langle -\nabla \mathcal{H} \rangle = \mathrm{Tr}\left[\rho \nabla \mathcal{H}\right] = \frac{\hbar}{2}\left(u \nabla \Omega_{\mathrm{real}} + v \nabla \Omega_{\mathrm{imag}}\right) \tag{2.4}$$

where, $\Omega_{\mathrm{real,imag}}$, u, and v correspond to the respective components of the torque ($\mathbf{\Omega}$) and Bloch ($\mathbf{R}$) vector. For the case of one-dimensional, counter-propagating optical fields whose

wavenumber is k, the force can be rewritten as

$$\mathbf{F} = \frac{\hbar\mathbf{k}}{2}\left((\mathbf{\Omega}_{\text{Right}} - \mathbf{\Omega}_{\text{Left}}) \times \mathbf{R}\right)_3 \tag{2.5}$$

here $\mathbf{\Omega}_{\text{Right}}$ and $\mathbf{\Omega}_{\text{Left}}$ are the torque vectors of the right and left propagating fields. These experiments consider the case of non-temporally overlapped pulses. Therefore at any point in time only $\mathbf{\Omega}_{\text{Right}}$ or $\mathbf{\Omega}_{\text{Left}}$ is considered. Thus the force simplifies to

$$\mathbf{F} = \frac{\hbar\mathbf{k}}{2}\left(\mathbf{\Omega}_{\text{Right,Left}} \times \mathbf{R}\right)_3 = \frac{\hbar\mathbf{k}}{2T}\Delta w \tag{2.6}$$

This is an expected result showing that the force on the atom is directly related to the change in w after interacting with the light. For the case of this experiment, the force experienced by an atom for a single pulse ($T = \pi/\omega_m$) is

$$\mathbf{F} = \frac{\hbar\mathbf{k}}{2}\frac{\omega_m}{\pi}\Delta w. \tag{2.7}$$

Thus, for ideal ARP conditions the maximum force is $\mathbf{F}_{\text{ARP}} = \hbar\mathbf{k}\omega_m/\pi$.

2.2 ARP in an Unconventional Region of Parameter Space

The traditional ARP conditions given in Eq. 2.3 are for a robust process in which the population of the system can be inverted with a high fidelity. These conditions work well in the magnetic resonance community; in the optical ARP case it is not as easy to meet all of these conditions due to limitations in optical power, or because of the inherent properties in the atomic system. For this reason, it is necessary to consider how well ARP works in an unconventional region of parameter space.

Figure 2.3 shows a contour plot showing the average force on a two-level atom after a single pulse pair sequence for various values of Ω_0 and δ_0. From the plot it can be seen that in the usual parameter range (upper right corner) the force is strong and robust to small variation in the light's parameters. However, the more interesting aspect of this plot is in

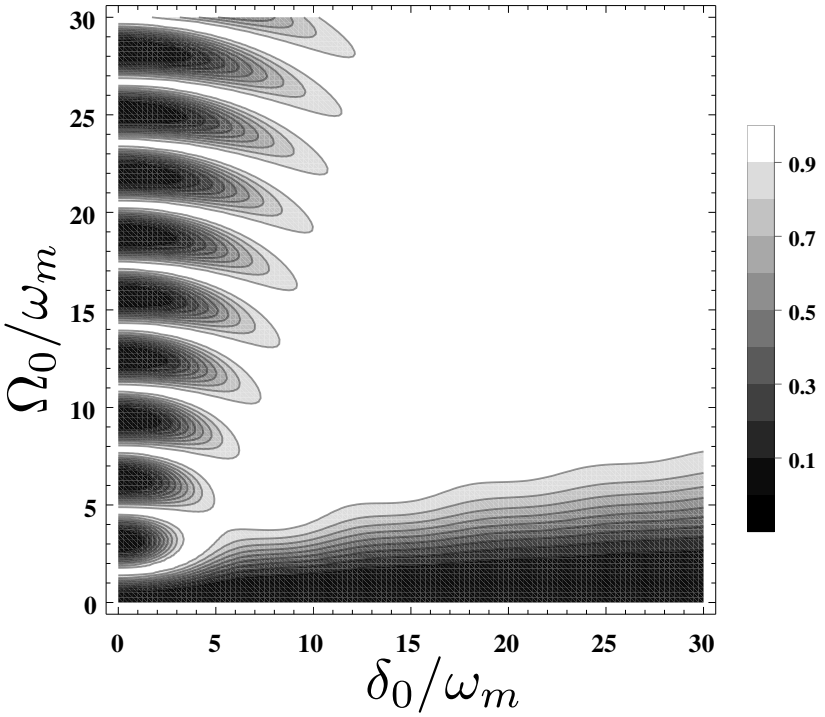

Figure 2.3: Plot of the ARP force as a function of Ω_0 and δ_0 for a single pulse pair. The color scheme shows the force in units of $\mathbf{F}/\mathbf{F}_{\mathrm{ARP}}$. For large values of Ω_0 and δ_0 the force is uniform and large. As Ω_0 and δ_0 get smaller approaching *Eq.* 2.8 the force becomes more sensitive to the values. Nonetheless, it can be seen that even in the lower left corner of the map, there are still some regions with strong forces.

the lower left corner. This is the case when

$$\delta_0 \sim \Omega_0 \sim \omega_m \gg \gamma. \tag{2.8}$$

In this region there are still certain parameters for which the force can be strong. This is further corroborated by Part (b) of Fig. 2.2, which plots the trajectory of the Bloch vector for one ARP pulse whose sweep parameters are given by, $\delta_0 = 1.10\ \omega_m$ and $\Omega_0 = 1.61\ \omega_m$. Although not agreeing with the intuitive picture of $\mathbf{R}$ following a spiral path around $\mathbf{\Omega}$, it shows that ARP pulses in this parameter regime can still invert the populations of a two-level system. This region of the phase space corresponds to the experimentally accessible region investigated in this thesis.

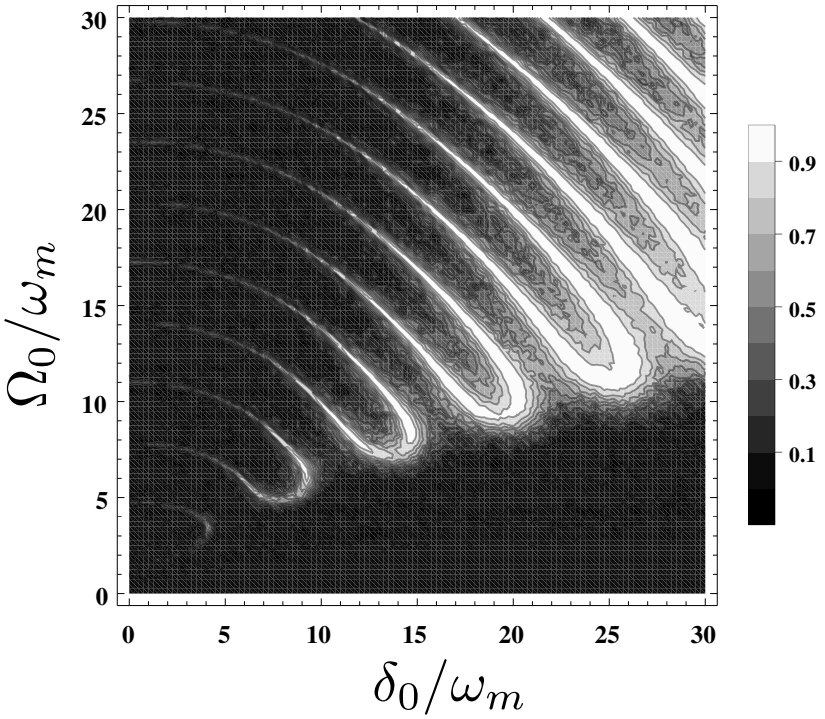

Figure 2.4: Plot of the ARP force as a function of Ω_0 and δ_0 after 320 pulse pairs. The color scheme plots the force in units of $\mathbf{F}_{\mathrm{ARP}}$. This plot differs from Fig. 2.3 in that the addition of mulitple ARP sequences means that the force is much more sensitive to the values of Ω_0 and δ_0. The large regions of strong force are much narrower, especially in the lower left corner (the experimentally accessible region).

2.3 Multiple ARP Sequences

Just as the radiative force requires a large number of absorption and spontaneous emission events to occur before the atom experiences a significant velocity change, so too does the ARP force require a large number of absorption-stimulated emission cycle to impart a large velocity change to an atom. The difference between the radiative force and the ARP force however, is that in the case of the ARP force, the process is fully coherent. For perfect ARP pulses the process follows the ideal model, and the addition of multiple ARP sequences doesn't change anything. However, for the case of an imperfect pulse, the multiple sequences will compound the small error from each pulse and the force will depart from the ideal.

Figure 2.4 shows the same force map as Fig. 2.3 except that the number of pulse pairs is increased from 1 to 320 pulse pairs (the number seen by the atoms in the experiment).

Looking at the plot, it can be seen that the regions of large average forces are much narrower, especially in the region that is experimentally accessible (lower left corner). The map does show that even for this large number of pulse pairs, there are pulse parameters for which strong forces can be generated on stationary atoms.

The reduced force felt by atoms due to imperfect pulses depends not only the pulse's inability to fully invert the system, but also on the relative phase between the counter-propagating pulse. Equation 1.13 shows the role that the phase of the Rabi frequency has on the Bloch vector. For a single ARP pulse, a frame which sets ϕ to 0 can be chosen, but in the case of two or more pulses this phase plays a critical role in the behavior of the system unless $\mathbf{R}$ is pointing exactly at the north or south pole. In an experiment such as the one described in this thesis, the atomic beam has a spatial extent which is much larger than a single wavelength. Thus, this phase can be handled by averaging over all possible relative phases between the counter propagating pulses. Section 5.3.2 further discusses this phase and the role that it plays in simulation results of the ARP force.

2.4 The Role of Spontaneous Emission

Spontaneous emission plays a critical role in the nature and magnitude of the ARP force. As stated above, the "rapid" condition requires that the sweep rate of the ARP process be faster than the natural decay rate, γ. Otherwise, the decay of the system will damp out the coherences established by the light, thereby preventing complete atomic inversion from taking place. For this reason, it is important to quantify this condition.

A measure of dependence of the ARP force as a function of sweep rate, ω_m/γ is shown in Fig. 2.5, for the pulse parameters $\delta_0 = 4.10\ \omega_m$ and $\Omega_0 = 3.37\ \omega_m$. The solid curve shows the case of 320 pulse pairs while, the dashed curves show 1, 10, and 100 pulse pairs with the longest dashes corresponding to 1 pulse pair and the shortest dashes to the 100 pulse pair case. From the plot, it can be seen that there is an apparent threshold for the sweep rate around $\omega_m/\gamma = 20$. Below this value, the force rapidly increases as ω_m/γ increases from 1 to 20. For sweep rates greater than 20, the force appears to saturate for all the plotted cases except the one corresponding to 10 pulse pairs. When $\omega_m/\gamma \sim 1$, spontaneous emission returns the atom to the ground state frequently enough that the counter-propagating pulse pairs are unable to efficiently transfer momentum to the atoms. As this value increases, the ARP process occurs rapidly enough that spontaneous emission is unable to significantly disrupt

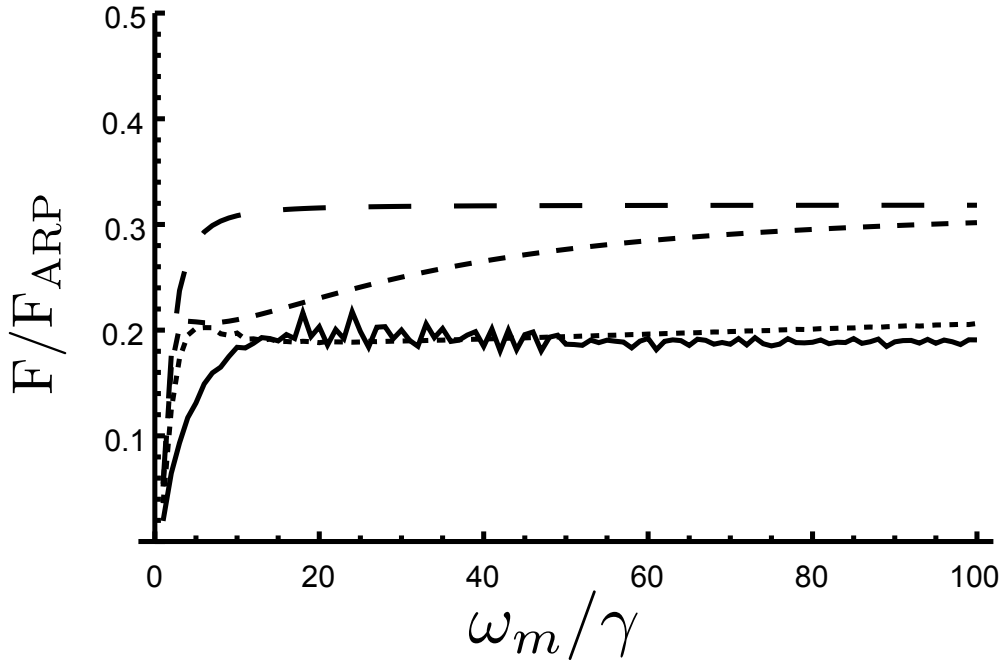

Figure 2.5: The "rapid" condition for ARP states that the sweep rate must be faster than any natural decay rate of the system. This plot shows the force on an atom after 1, 10, 100, and 320 (solid line) number of pulses. The size of the dashes get smaller as the number of pulses goes up. From this plot it can be seen that a sweep rate greater than $20\omega_m/\gamma$ appears to be fast enough to meet the "rapid" condition of ARP.

the coherence of the atom-light interaction. As such, more momentum can be transferred to the atoms. For the experiments performed in this thesis, a sweep rate of $\omega_m/\gamma = 100$ is used. It is worth noting that even in the case of large ω_m/γ, the number of pulse pairs is still important to consider because as seen Fig. 2.5, the case of 320 pulse pairs results in a force which is smaller than in the case of 10 pulse pairs.

The choice of a sweep rate of $\omega_m = 100\gamma$ means that a single ARP sequence is fast enough that spontaneous emission can be neglected. However, it does not fully eliminate the effects of spontaneous emission for the case of a long sequence of ARP pulses. For a long sequence of ARP pulses, spontaneous emission can reverse the direction of the force if it occurs at the wrong time in the pulse-pair sequence. Figure 2.6a shows the ideal pulse train. However in this configuration, if a spontaneous emission event were to occur between the first and second pulse (Black/Right and Red/Left) of a pair, then the second pulse would deliver momentum to the atom in the wrong direction, leading to a reversal of the force. This force reversal

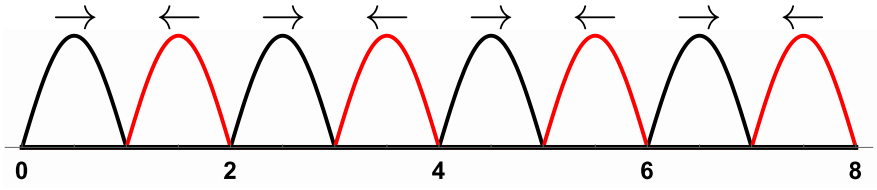

(a) No Dead Time

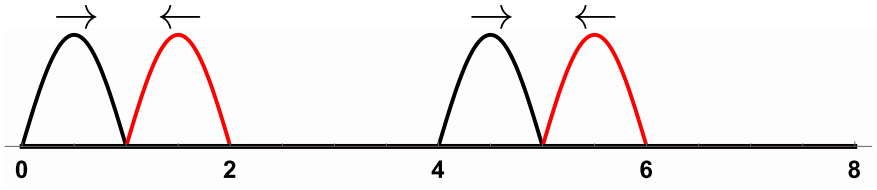

(b) With Included Dead Time

Figure 2.6: A schematic diagram of the timing scheme of the multiple ARP sequence. Figure 2.6a shows the ideal scheme. Pulses traveling in alternating directions interact with the atoms sequentially. Figure 2.6b shows the scheme which is designed to reduce the effects of spontaneous emission on the force. A pair of pulses traveling in opposite directions interact with the atoms, followed by a period of time in which no light interacts with the atoms. This time, referred to as dead time, helps to break the sysmmetry of experiment, by increasing the probability that spontaneous emission will occur at a time that does not cause a force reversal.

would then continue until another spontaneous emission event similar to the first occurs. This would result in no net average force. This problem is addressed by a modification to the pulse train, in which the light on the atoms is turned off for a period of time (dead time). Figure 2.6b shows the modified pulse train with the inclusion of dead time. The dead time is not designed to be comparable to lifetime of the excited state; instead, it is meant to break the symmetry of the process and impart a preferred direction to the force. Consider the probability of spontaneous emission occurring after the first pulse but before the first pulse in the subsequent pulse pair is $\frac{T_{\mathrm{pulse}}+T_{\mathrm{deadtime}}}{4\pi/\omega_m}$, while the probability of it occurring between the first and second pulse of a pulse pair is $\frac{T_{\mathrm{pulse}}}{4\pi/\omega_m}$. So for a non-zero dead time the atom is more likely to spontaneously decay at a time which will not reverse the force than at a time when it will.

Figure 2.7 shows the ARP force vs number of pulses pairs for five different values of dead

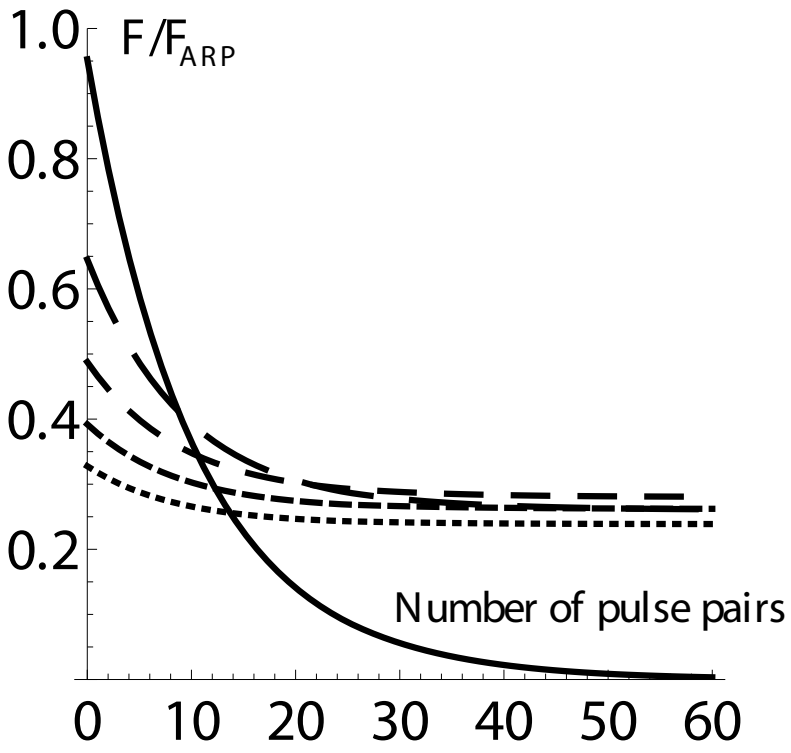

Figure 2.7: The calculated force *vs.* number of pulse pairs for various length of dead time. The solid curve shows the case of no dead time, and the dashed curves show the different values. As the dashes get smaller the length increases in integer multiples of π/ω_m (1, 2, 3, and 4 respectively). For a large number of pulse pairs the force converges to a non-zero value with the inclusion of dead time. For the experiment the value of $2\pi/\omega_m$ is chosen. Taken from Ref. [32]

time in increments of π/ω_m. For the case of zero dead time (the solid curve), the average force is reduced to zero after a small number of pulse pairs, due to increasing probability of force reversal. However, the inclusion of dead time allows for a non-zero force to be maintained over a large number of pulse pair sequences. In the experiments described in this thesis, the length of dead time is chosen to be $2\pi/\omega_m$, because it maintains the greatest force over time. The addition of the dead time does have a negative effect on the maximum force, because the total time between absorption-stimulated emission changes from $T = 2\pi/\omega_m \rightarrow 4\pi/\omega_m$ while the momentum change remains $2\hbar\mathbf{k}$ thus the force is reduced to $\mathbf{F}_{\rm ARP}/2 = \hbar\mathbf{k}\omega_m/2\pi$. For the experimental sweep rate of $\omega_m = 100\gamma$ the force $\mathbf{F}_{\rm ARP}/2 \approx 32F_{\rm rad}$.

Although the inclusion of the dead time prevents the force from averaging to zero over a long period of time, it does not prevent the magnitude from being reduced to a value less than the expected $\mathbf{F}_{\mathrm{ARP}}/2$. This further reduction occurs because the decay term in the OBEs causes a decrease in the length of the Bloch vector $|\mathbf{R}|$ from its starting value of 1 to a steady state value of ≈ 0.5. This means that over time spontaneous emission causes a loss of coherence within the atom, and as a result, the atoms are in a constant superposition of $|g\rangle$ and $|e\rangle$ states. Therefore, even perfect ARP pulses are unable to transfer the full $2\hbar\mathbf{k}$ of momentum, since $|\mathbf{R}| < 1$ cannot reach from pole to pole. Thus, over time, the average force will be reduced to a value less than $\mathbf{F}_{ARP}/2$.

The treatment of spontaneous emission in the OBEs is a good starting point for addressing the influence that spontaneous decay has on the ARP force. However, because the OBEs only address the ensemble average, the magnitude of the Bloch vector decays to less than one and will never return to unity. This means that the force calculated from this result will only be an average force. Also, because the ARP force derives from multiple pulse pairs, there is no way in the OBEs to reestablish the coherence, even though in the actual system this is possible because the next light pulse will interact with the atoms and establish some coherence. Another issue with the OBEs and the multiple ARP sequences is that there is no clear picture which will properly set the clock of the system. Because the atom undergoes hundreds of cycles between the ground and excited state along with long periods in which there is no light on the atom, it is not clear how to handle the clock reset or start time for spontaneous emission. For these reasons another method of treating spontaneous emission for multiple ARP sequences is required and is in progress. All of the simulations of the OBEs performed henceforth will treat spontaneous emission as a decay of the Bloch vector as described above.

Chapter 3

Experimental Apparatus

This chapter provides an overview of the apparatus used for the experiments described later in the thesis. It starts with a description of the inner workings of the metastable Helium source, followed by an overview of the atomic beam line, and the atomic beam detection methods. It then moves on to a description of the lasers used in the experiment and how the frequency is stabilized and locked, how ARP light is produced through the use of electro-optical modulators, and how the light is amplified to the power necessary for the ARP process.

This experiment uses metastable Helium (He^*) as the atomic species, and works on the $2^3S_1 \rightarrow 2^3P_2$ transition shown in Fig. 3.1. This is an ideal transition for ARP to work on due to the rather long life time of the excited state. The large separation between the adjacent J levels means the transition can be well-approximated as a two-level system. The other relevant parameters of this transition are given in Table 3.1.

Transition	Energy (eV)	$\omega_a/2\pi$ (THz)	λ (nm)	$\gamma/2\pi$ (MHz)	τ (ns)	$\omega_r/2\pi$ (kHz)	I_s (mW/cm^2)	v_r (m/s)	γ/k (m/s)
$2^3S \rightarrow 2^3P$	1.14	276.7	1083.3	1.62	97.9	42.5	0.17	0.092	1.76

Table 3.1: Table of the atomic parameters of Helium relevant to the ARP experiment [35].

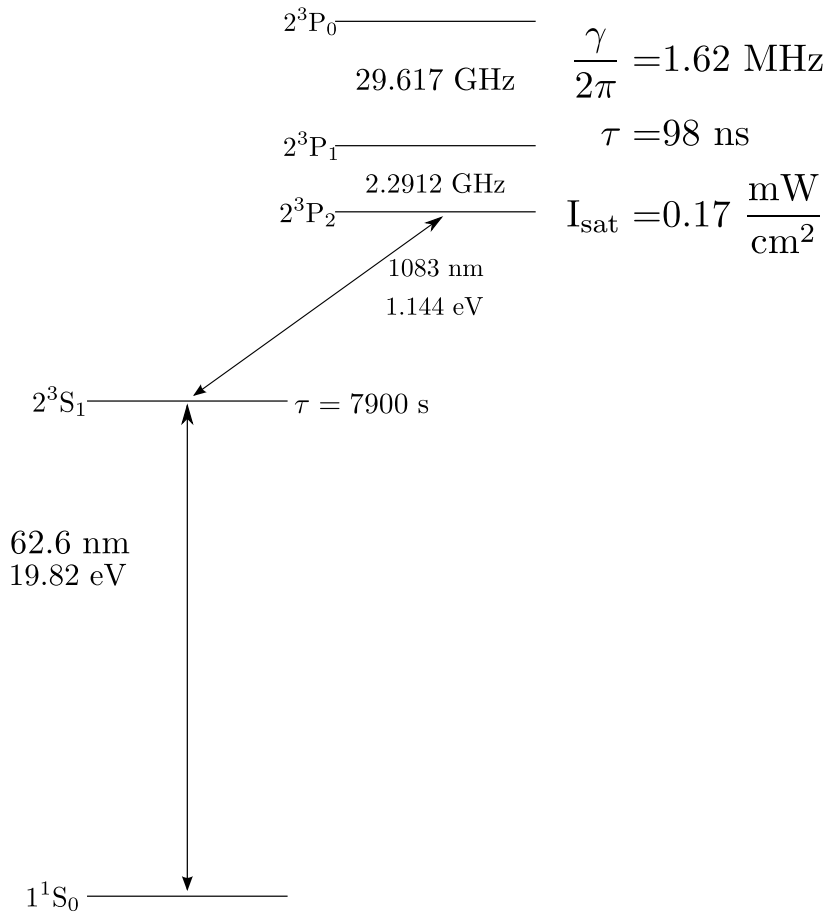

Figure 3.1: Partial energy level diagram of Helium addressing the relevant levels for this experiment. The lifetime of 2^3S is $\sim$ 7900 s and is treated as the "ground state" for this experiment [34].

3.1 Vacuum System

A schematic diagram of the vacuum system, used for the experiments described in this thesis, is shown in Fig. 3.2. The vacuum system is made up of three parts, the metastable helium source which generates the atomic beam with atoms in the 2^3S state, the atomic beamline where the light interacts with the atoms, and the detection region.

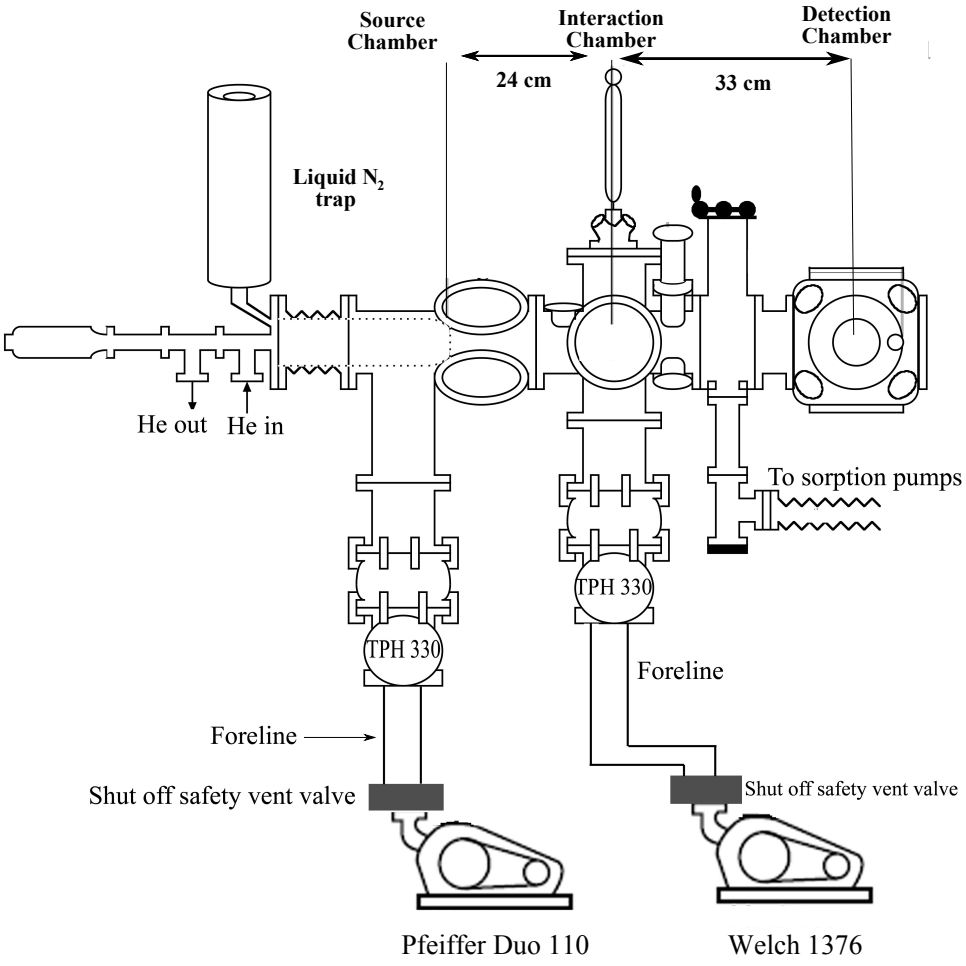

Figure 3.2: The vacuum system used in this experiment. It is made up of 3 sections: the source, the interaction region, and the detection region. The interaction region spans from the output of the source nozzle to the point where the light interacts with the atoms (24 cm), and the region between the optical interaction to the front of the detector (33 cm).

3.1.1 Metastable Helium Source

The metastable Helium source is a reverse-flow, DC discharge atomic source based on the design presented in Shimizu [36], and includes the modifications outlined in Maswijk, *et al.* [37]. It was constructed in Universiteit Utrecht, then assembled and tested in Stony Brook in 1999, where it has been in operation since. A diagram of the source is shown in Fig. 3.3.

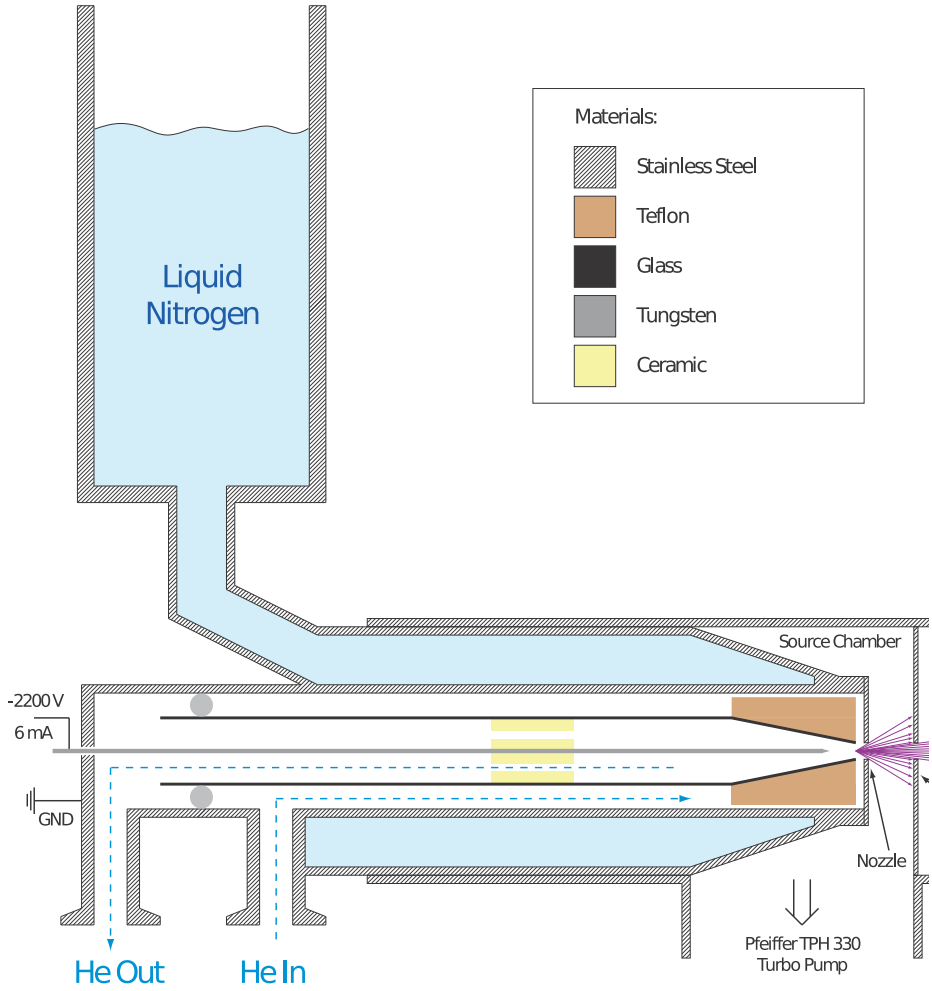

Figure 3.3: A schematic diagram of the metastable Helium source used in this experiment.[29]

The source consists of a 1 cm diameter glass tube, which is tapered at one end. Inside is a 1 mm diameter tungsten needle centered coaxially with the glass tube by a ceramic spacer. The glass tube is placed inside a stainless steel jacket with a diameter of 3 cm, and is centered

in the jacket through the use of an O-ring at the non-tapered end and a teflon spacer shaped to hold the tapered end.

Helium gas flows into the source as shown in Fig. 3.3, between the outside of the glass tube and the steel jacket around the teflon spacer through the front of the glass tube, and is pumped out of the source past the tungsten needle by a Welch 1376 mechanical pump. As the helium flows through the source, it is cooled by contact with the liquid nitrogen-cooled steel jacket.

To light the source, $-2200\,\mathrm{V}$ is applied to the tungsten needle. As the helium flows past the tip of the needle a discharge forms between the needle (cathode) and the nozzle plate (anode). The discharge forms a plasma which is maintained by the helium flow. Inside of the plasma, metastable helium atoms in both the singlet ($2^1\mathrm{S}$) and the triplet ($2^3\mathrm{S}$) state are formed through electron-ion recombination. Although most of the metastable Helium atoms are quenched due to collisions, some of the triplet state atoms remain.

The source region is pumped by a Pfeiffer TPH 330 turbo pump backed by a Pfeiffer Duo 110 mechanical pump. While the source is running, the absolute pressure of the source chamber, measured by an ion gauge, reads on the order of $10^{-5}\,\mathrm{Torr}$, up from the base pressure of $10^{-7}\,\mathrm{Torr}$. Under typical working conditions, the backing pressure of the source's turbo pump will rise to $\sim 160\,\mathrm{mTorr}$ while the outlet pressure reads $\sim 1\,\mathrm{Torr}$. These settings are chosen to optimize the the reliability of the source at the expense of efficiency. Thus the process has a conversion efficiency of ground state Helium to the triplet state of only $\sim 10^{-5}$.

Behind the nozzle plate is a skimmer plate with a $0.5\,\mathrm{mm}$ opening whose purpose is to define the size of the atomic beam. It also serves as a means of differential pumping between the source region and the beam line region of the vacuum system pumped by its own turbo pump [38].

3.1.2 Atomic Beamline

The beamline section is the largest part of the vacuum system. It spans the region from the output of the skimmer plate all the way to the front of the detector ($\sim 57\,\mathrm{cm}$). In this section, the atoms interact with the light for both the ARP and the UV bichromatic force experiments [28]. Just as with the source, this region of the vacuum system is pumped by a Pfieffer TPH 330 turbo molecular pump and maintains a background pressure, with the source off, of $\sim 10^{-7}\,\mathrm{torr}$.

The atomic beam produced by the source travels through the skimmer plate aperture. It consists of a mixture of ground state Helium, singlet and triplet state metastable Helium, Helium ions, electrons, 62 nm UV emission from quenching of metastable Helium atoms in the source plasma, and visible light due to relaxation of the excited Helium. The atoms emerge from the source with a roughly Maxwellian velocity distribution, slightly supersonic, with mean velocity of 1000 m/s and a spread of ± 400 m/s, and have a transverse velocity spread of ± 40 m/s [23].

The atoms travel 24 cm down the beam line and pass through a 250μm wide and 1 cm tall slit made out of brass shim stock. This slit serves to define the atomic beam with a very small transverse velocity (± 1 m/s) and a narrow spatial extent, as opposed to the transverse spread of the atomic beam directly out of the source whose angular spread spans a region larger than the detector.

Immediately following the atomic slit is a pair of Helmholtz coils which serve to provide a uniform magnetic field transverse to the atomic beam and define a z-axis. The coils and atomic slit share the same Macor mount, shown in Fig. 3.4. A relatively small magnetic field of a only a few Gauss is all that is needed to break the Zeeman degeneracy of the 2^3S_1 state, $(1.4\,\mathrm{MHz/G})\mathbf{B} > \gamma/2\pi = 1.62\,\mathrm{MHz}$. Based on the design of the coils, $\mathbf{B} = 3.77\,\mathrm{I(amps)}$ so a magnetic field of this magnitude can be achieved with little more than a few amps of current.

3.1.3 Detection system

Two metastable He detectors are commonly used in this lab; a multi-channel plate/ phosphor screen combination (MCP/PS) and a stainless steel detector (SSD). For this experiment, we are more interested in the atom's position on the detector and the shape of the final atomic distribution than on the absolute number of atoms detected, so only the MCP/PS will be discussed. A diagram of the MCP/PS detector is shown in Fig. 3.5.

The MCP is a thin, 1" diameter disk comprised of 10 μm diameter, lead-coated glass tubes (channels) arranged in a hexagonal pattern of radius 12 μm. These tubes are aligned at an 8° angle to the normal of the plate. When a He^* atom is incident on the MCP, its 19.8 eV of internal energy is more than enough to eject an electron into the channel it struck. The MCP is negatively biased with -1000 V on the front and grounded on the back. This bias causes electron multiplication and acceleration as the electrons travel through the

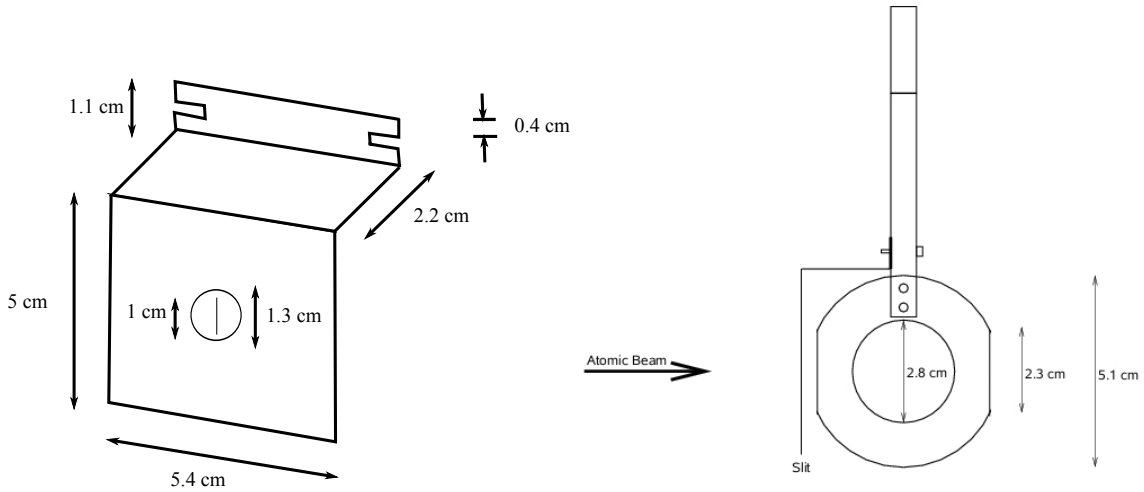

(a) Front View (b) Side View

Figure 3.4: Schematic Diagram of the atomic slit and Helmoholtz coils [38].

channels. The Photonis MCPs used in this experiment are specified to provide a gain of $\sim 10^3$ when biased with $-1000\,\mathrm{V}$.

The electrons are accelerated by a $\sim +2000\,\mathrm{V}$ bias voltage and then detected on a 1 inch diameter Lexel phosphor screen located directly behind the MCP. The phosphor screen consists of a 1.16 inch diameter glass plate with a layered Indium Tin Oxide and aluminum coating to help with conductivity. On top of the aluminum is deposited a thin layer of P43 phosphor. The electrons incident on the screen cause a fluorescence of the phosphor at the position of impact, with the brightness roughly proportional to the flux of electrons which hit the screen. This electron flux is of course, proportional to the number of He^* atoms that impact the detector. A mirror mounted at 45° allows for the image of the phosphor screen to be captured by an external CCD camera through a side window of the detection chamber.

While the MCP/PS provides for very efficient detection and measurement of the spatial distribution of He^*, it is not without its problems. The detector not only responds to the He^* atoms but also to the UV light emitted by the source. The geometry of the vacuum system means that both the UV light and the He^* atoms travel identical paths and thus are indistinguishable on the detector. The nonlinear response of the PS due to non-uniformity of the phosphor and over-exposure of the screen, means that obtaining an absolute calibration between atom number and intensity of the fluorescence is not possible.

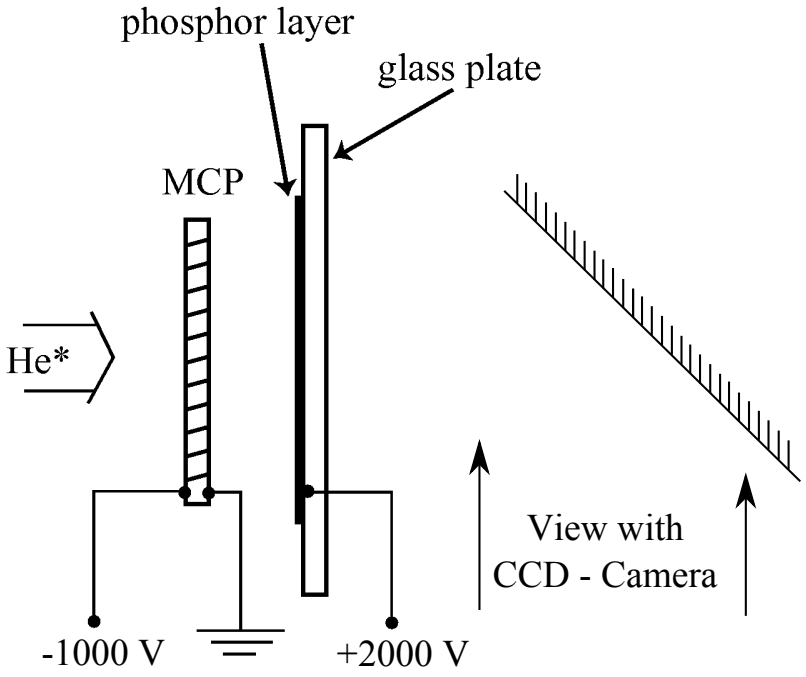

Figure 3.5: Diagram of the MCP/PS detector. Metastable Helium incident on the MCP causes electrons to be ejected. The bias across the MCP cause a cascade of electrons to be accelerated to the phosphor screen, where the fluorescence of the phosphor can be seen. A CCD is then used to capture images of the screen. Modified from [38].

3.2 Optical System

This section will outline the optical system used in the ARP experiments. It starts with a description of the infrared light source and the frequency stabilization techniques, then moves on to the electro-optical modulators which are used generate the frequency chirp and amplitude modulation needed for the ARP process. Finally, the optical amplification devices used to produce the required optical intensity for ARP are described.

3.2.1 Infrared Laser Diodes

A pair of Spectra Diode Labs SDL-6702-H1 Distributed Bragg Reflector (DBR) lasers serve as the light sources in this experiment. A thorough investigation into the frequency control and stability of the two diodes used in the ARP experiments was performed by C. Avila [39]. The diodes come in a standard 8-pin TO-3 window package with a thermistor

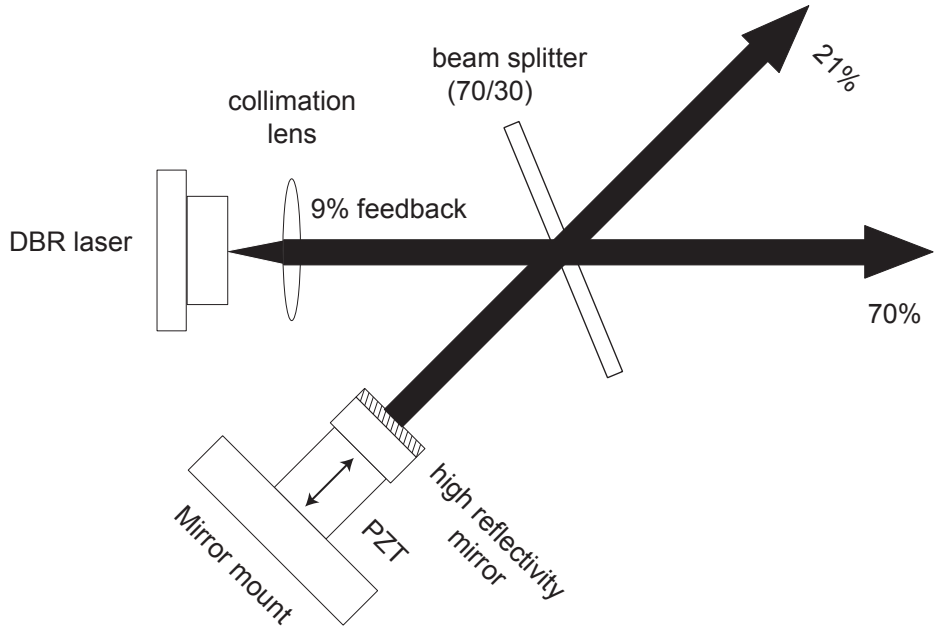

Figure 3.6: Layout of the extended cavity diode lasers. The light transmitted through the 70/30 beam splitter is sent to the experiment, the reflected light is used for feedback (9%) and for locking (21%) as shown in the diagram [23].

and thermoelectric cooler included. One diode (ARP diode) has a Newport model 325 temperature controller and a Newport model 505 current controller used for the current injection and temperature stabilization. The other diode (Litho diode) uses a Lightwave LDT-5910 temperature controller and Thorlabs LDC-500 current controller.

Stabilization of the laser frequency is crucial for the ARP experiments performed in this thesis. On the short time scale the frequency can be stabilized by adjusting the temperature ($-22\,\mathrm{GHz/^\circ C}$) and the current ($-300\,\mathrm{MHz/mA}$). The $2^3S_1 \rightarrow 2^3P_2$ in He^* requires a wavelength of ($\lambda = 1083.33065\,\mathrm{nm}$), and to achieve this, the ARP diode's thermistor was typically set to $10.00\,\mathrm{k\Omega}$ ($\sim 25^\circ\mathrm{C}$) and the current set to $150.0\,\mathrm{mA}$. The Litho diode is operated at a temperature of $\sim 23.3^\circ\mathrm{C}$ and $\sim 152\,\mathrm{mA}$. The typical output power for each diode at the given settings is $\sim 30\,\mathrm{mW}$.

An extended cavity (EC) is used to provide the necessary active optical feedback to the laser. The EC consists of 70/30 beamsplitter, a high reflective mirror mounted on a piezo-electric transducer (PZT), and the Bragg reflector of the laser diode (see Fig. 3.6). The reflected portion, 9% of the full output power, is sent back to the laser for the purpose

of frequency stabilization. Two beams leave the cavity, the smallest of which, 21% of the full power (the leakage beam), is used for Saturation Absorption Spectroscopy and provides the reference signal. The remaining beam, which contains 70% of the output power passes through some beam shaping optics and a Faraday isolator, and is then coupled into an optical fiber and sent to the experiment. The frequency of the laser can be adjusted by changing the position of the EC mirror with a voltage applied to the PZT. Besides providing fine tuning of the frequency, the EC also reduces the linewidth of the laser [40, 41] to $\sim 125\,\mathrm{kHz}$ [23], which is less than the natural linewidth of the $2^3S_1 \rightarrow 2^3P_2$ transition in He^* (1.62 MHz).

To lock the lasers and further reduce the fluctuations and drift of the lasers' frequency, a Doppler-free saturated absorption spectroscopy (SAS) signal is used as a reference signal. The setup used for the SAS is shown in Fig. 3.7. It is a typical SAS setup as described in Ref. [20]. The major difference in this setup is the use of a Helium discharge cell to excite the atoms to the 2^3S state, which is used as the ground state instead of the actual ground state. The discharge cell consists of a typical gas cell, filled with Helium, and wrapped with coils driven by an rf voltage at 51 MHz generated by an HP 8640, and amplified by an EIN 420LA RF. The amplfied rf interacts with the Helium in the cell producing a mild discharge. He collisions in the cell excite a small fraction of the atoms to the correct He^* state. The rest of the locking scheme is described in the thesis of D. Stack [38].

3.2.2 Phase Modulator

The ARP experiment requires pulses and a specially-tailored frequency chirp in order to efficiently invert the state of the atoms. To achieve this, electro-optical modulators (EOM) are used. An EOM uses the principle of the linear electro-optical effect in a $LiNbO_3$ crystal. The linear electro-optical effect describes a change of the index of refraction of material that is proportional to the strength of an applied electric field [42]. The phase modulators used in this experiment, model $NIR - MPX - LNO3$, are purchased from Photline Technologies[1]. The modulators consist of an integrated waveguide modulator, with PM fibers pigtailed on both ends making it easier to align the correct polarization into the waveguide.

A time dependent voltage applied to the electrodes of the phase modulator introduces a

[1]Photline Technologies, 16 rue Jouchoux, 25000 Besancon, France. Phone: +33 (0) 381 85 31 80. www.photline.com

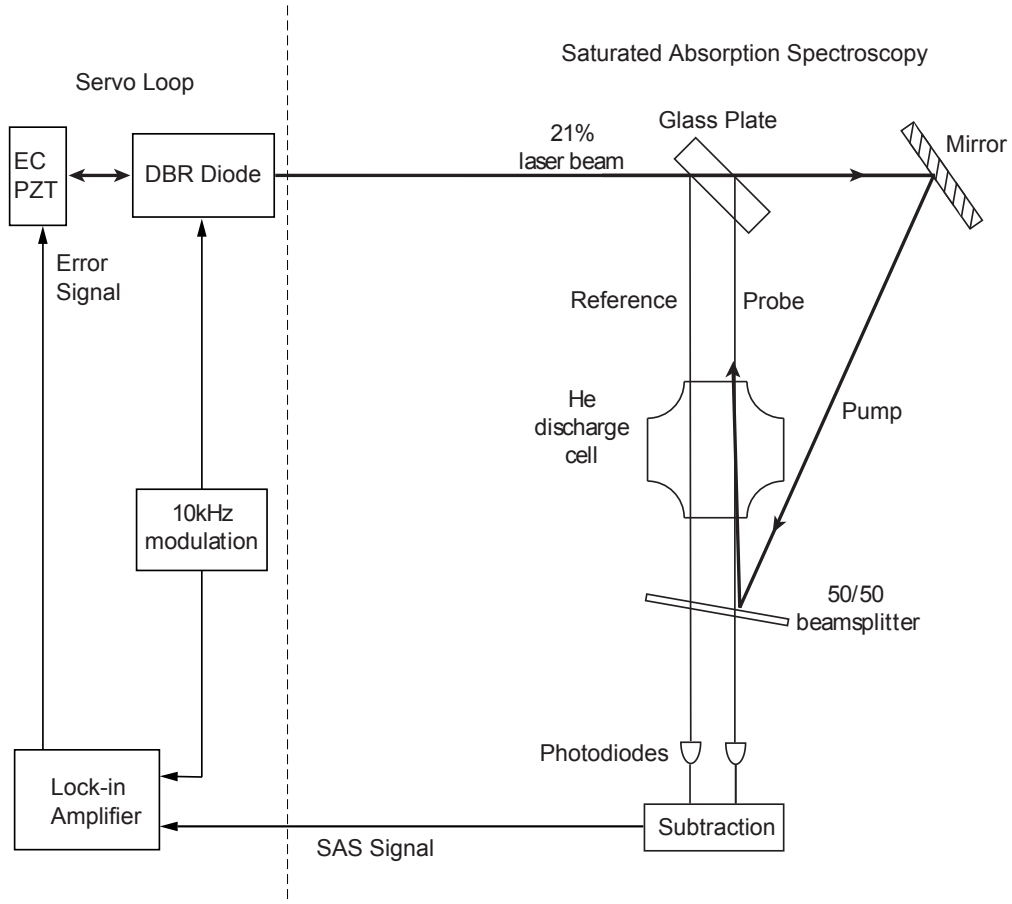

Figure 3.7: The layout of the locking scheme used to lock the diode lasers to the $2^3S_1 \rightarrow 2^3P_2$ transition. On right is the optical setup which uses the leakage beam, on the left is the electronic feedback loop used in the SAS locking. [23]

phase delay to the light passing through the device given by

$$\phi(t) = \kappa M(\omega_m) V(t) \tag{3.1}$$

where $M(\omega_m)$ describes the frequency dependence of the phase delay as a result of rf losses and optical phase mismatch, and

$$\kappa = \frac{\pi}{\lambda G} n_e^3 r_{33} \eta L \tag{3.2}$$

L and G are the length and gap respectively between the electrodes, r_{33} is the electro-optical coefficient along the z-axis of the crystal, n_e is the index of refraction for light polarized in the extraordinary direction, and η is a coefficient associated with the overlap of the electric

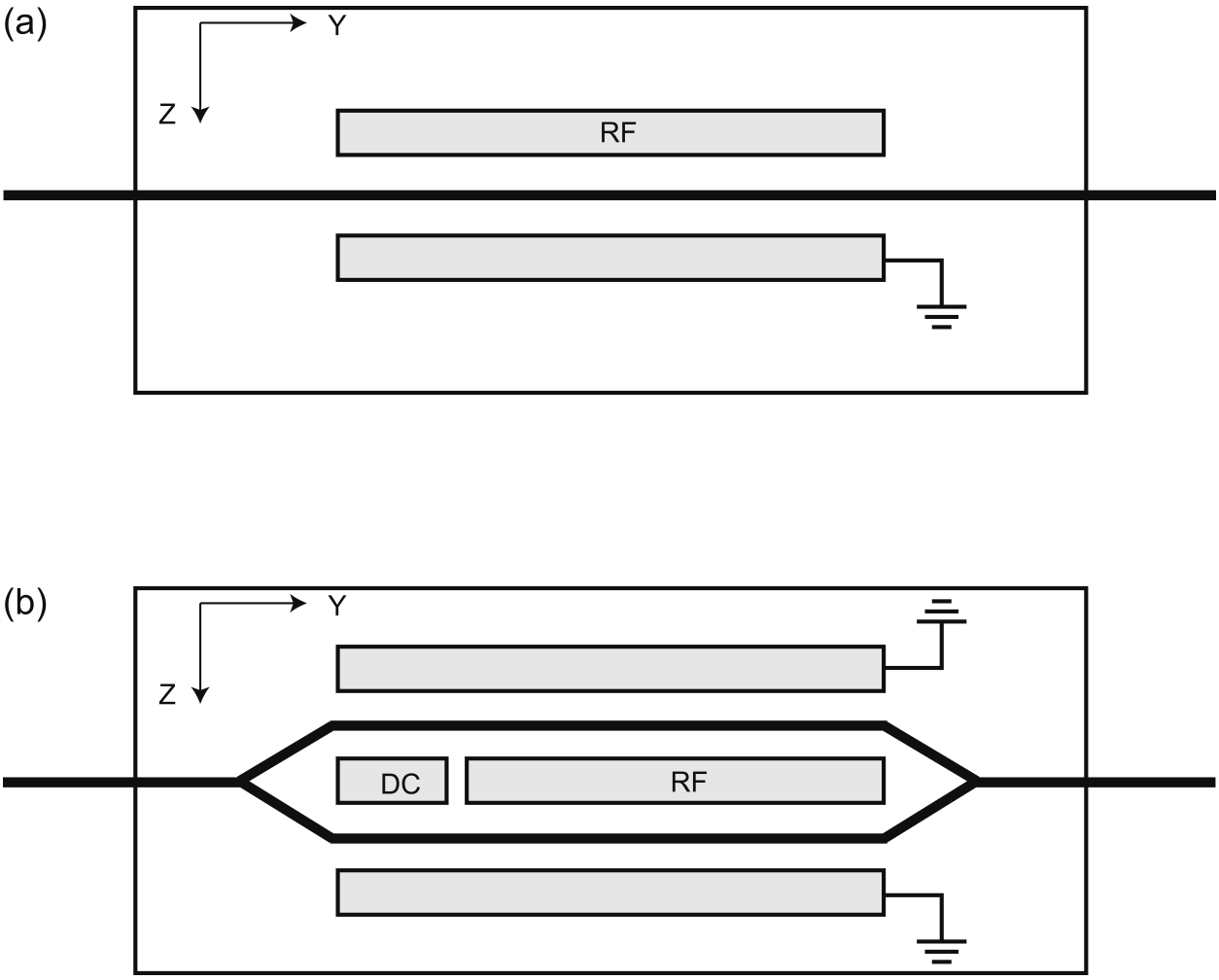

Figure 3.8: Schematic of the two types of Photline modulators used in the ARP experiments. (a)The NIR-MPX-LN03 phase modulator and (b) the NIR-PX-LN03 amplitude modulator.

and optical fields.

A sinusoidal rf signal applied to the phase modulator results in an optical field of the form

$$E(t) = E_0 \cos\left(\omega_l t - \beta \sin(\omega_m t)\right) \tag{3.3}$$

where E_0 is the amplitude of the light field, ω_l is the unmodulated frequency, and β is the amplitude of the phase modulation referred to as the modulation index. β is given by the equation

$$\beta = \frac{\pi V}{V_\pi(\omega_m)} \tag{3.4}$$

V_π is the voltage required to shift the phase of the optical field by π. For a given modulation frequency (ω_m), it can be calculated using Eqs. 3.1 and 3.2

$$V_\pi(\omega_m) = \frac{\lambda G}{n_e^3 r_{33} \eta L M(\omega_m)} \tag{3.5}$$

Although, V_π can be calculated based on the physical parameters of modulator, it is generally easier to measure the value from the Fourier spectrum of the modulated light. The method of doing this is explained in great detail in the previous theses on this experiment [23, 38] and as such will not be covered here.

The time derivative of the overall phase of a light field gives the instantaneous frequency, therefore

$$\omega(t) = \frac{d\phi(t)}{dt} = \omega_l - \beta\omega_m \cos(\omega_m t). \tag{3.6}$$

Thus, a sinusoidal phase modulation results in a cosinusoidal frequency chirp at the modulation frequency ω_m.

3.2.3 Intensity Modulator

The pulses used in the ARP light are generated using a Photline $NIR - MX - LNO3$ intensity modulator, whose operation is similar to that of the phase modulator. It uses a pair of waveguides placed in a Mach-Zehnder interferometer configuration (Fig. 3.8b) [43]. In this configuration, the modulator's two grounded electrodes are placed on the outside of the waveguides and two active electrodes are placed in between the two arms. One active electrode has a DC voltage applied to it that is adjusted so that it causes destructive interference when the light from the two arms recombine. The other, larger electrode has an rf pulse

applied to it, and it produces the desired optical pulse.

Light that passes through the amplitude modulator, emerges from the device with a modified electric field given by

$$E(t) = \frac{E_0}{2}\left[\sin\left(\omega_l t + \phi(t)\right) + \sin\left(\omega_l t - \phi(t)\right)\right] = E_0 \sin\left(\phi(t)\right)\sin\left(\omega_l t\right) \tag{3.7}$$

where the phase shift of one arm of the interferometer caused by the rf is given by $\phi(t)$, and phase shift in the other arm is $-\phi(t)$. The balanced design of the modulator with each arm receiving a phase shift of the same magnitude but opposite signs results in an E-field with an overall amplitude modulation but without any net phase modulation.

3.2.4 Fiber Amplifiers

The diode lasers used in this experiment produce $\sim 20\,\mathrm{mW}$ of power out of the EC. When taking into account the insertion losses of both the EOMs and the power loss due to the 25% duty cycle amplitude modulation, the available average power is $< 0.1\,\mathrm{mW}$. The ARP process typically requires $\sim 1\,\mathrm{W}$ of average power to generate the Rabi frequency necessary for the atomic state to adiabatically follow the optical field. To achieve this large average power a pair of Keopsys model $\mathrm{KPS-BT2-YFA}$ 4W fiber amplifiers are used.

The fiber amplifiers use Yb-doped fibers as their gain medium. The Yb ions in the fiber strongly absorb 980 nm pump light and emit light in a $1050\,\mathrm{nm} - 1100\,\mathrm{nm}$ window. High power 980 nm pump diodes inject the pump light into the cladding of the fiber through a mechanical V-groove[2]. Seed light launched into the fiber core is amplified through a process of stimulated emission, with gain that is proportional to the power of the 980 nm pump light.

3.2.5 Booster Optical Amplifiers

The $\mathrm{KPS-BT2-YFA}$ fiber amplifier requires an average input power $> 0.5\,\mathrm{mW}$ to seed its pre-amp stage, and this is needed to saturate the full amplification stage. In order to increase the power from $< 0.1\,\mathrm{mW}$ to $0.5\,\mathrm{mW}$, a Thorlabs BOA1137P booster optical amplifier (BOA) is used to provide the small gain needed to exceed the input threshold of the fiber amplifiers. A BOA is simply described as a semiconductor diode laser with anti-reflective coatings instead of highly-reflective coatings on its faces to prevent oscillation.

[2]A patented Keyopsys feature

The BOA makes use of a waveguide in the amplification process and as such amplifies only light of a given polarization. Thus the devices used in this experiment are pigtailed with PM980 polarization-maintaining fiber on both the input and output of the device. Although the BOAs have many great advantages, they also can cause self-phase modulation (SPM) thereby changing the light's characteristics. To alleviate the SPM, the BOAs have to be used before the amplitude modulators.

The BOA1137Ps used in this experiment come in a standard 14-pin butterfly package and are mounted in a Thorlabs LM14S2 universal butterfly mount. One of the BOAs uses a Newport Model 325 Temperature Controller typically set to 15.84 kΩ ($\sim 16°$C) and a Newport Model 505 Laser Diode Driver running at 302.4 mA. The second BOA is controlled with an ILX Lightwave LDC-3722 Laser Diode Driver, which also has a temperature controller; the settings for this BOA are 14.5 kΩ ($\sim 16°$C) and 330.15 mA. The reason for running the BOAs at a temperature that is not 25°C is because both BoAs have a center wavelength which is near 1050 nm, so they are cooled and driven at max current to enhance their gain at 1083 nm.

3.3 The Experimental Setup

The experiments described in this thesis are designed to measure a 1-D transverse deflection of atoms in an atomic beam caused by interaction with ARP pulses. A layout of the experimental setup is shown in figure 3.9; a detailed explanation of each of the components is given in Chapter 3.

3.3.1 Production of the ARP Light

The ARP pulses used in the experiment are specially tailored to have the specific amplitude and phase modulation of a half sine pulse at 25% duty cycle with a cosinusoidal chirp, as described in Chapter 2. To achieve this modulation, phase (Sec. 3.2.2) and amplitude (Sec. 3.2.3) modulators are used.

The amplitude modulators are driven by a Tektronix DTG5274 Data Timing Generator, operating at 320 MHz with 1/4 pulse rate and 17% duty cycle. For these settings, the DTG5274 outputs a nearly-triangle pulse that has a base width of ~ 3.125 ns and a repetition rate of 80 MHz. Fine tuning of the optical pulse shape can be made by adjusting the

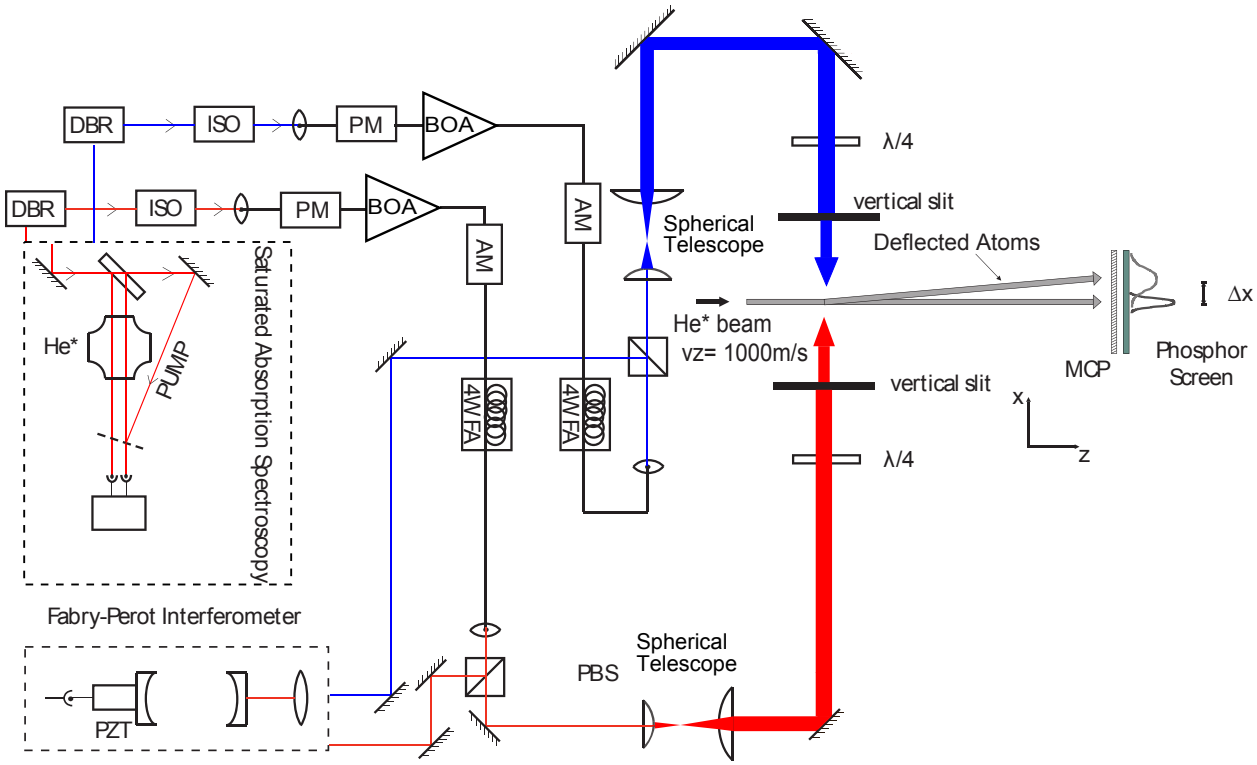

Figure 3.9: Diagram of the full experimental setup. The components of the setup are as follows: DBR: Distributed Bragg Reflector diode laser, ISO: Faraday optical isolator, PM: phase modulators, AM: amplitude modulators, BOA: Booster Optical Amplifiers, and 4WFA: Keyopsys fiber amplifiers.

amplitude of the electric pulse and the external DC voltage (supplied by a Power Design Inc. model 2005 precision power supply) to the amplitude modulator. The DTG5274 has two outputs that are used to drive both of the amplitude modulators. It also has the ability to control the phase between these two outputs, thereby providing an electronic means of delaying one optical pulse with respect to the other in the experiment.

The phase modulators, which create the frequency chirp, are each driven by a 160 MHz sinusoidal rf signal originating from separate signal generators. The phase modulator for the ARP (3.2.1) diode uses an HP 8657D signal generator, while the modulator for the Litho (3.2.1) diode uses an HP 8657A signal generator. Both rf signals are then amplified by their own Mini Circuits ZHL-1-2W-S+ 2W rf amplifier, whose DC voltage is supplied by a Power Design Inc model 6150 supply. Separate signal generators and rf amplifiers are needed because the modulation index for each optical phase modulator is different, and in order to

obtain the same amount of frequency sweep, it is necessary for the rf signals to have different amplitudes. For the ARP diode's phase modulator, the conversion from $V_{\rm rms}$ of the rf signal to δ_0/ω_m was measured to be

$$V_{\rm ARP}({\rm mV}) = \frac{(\delta_0/\omega_{\rm m})}{0.0265} \tag{3.8}$$

and for the Litho diode's phase modulator

$$V_{\rm Litho}({\rm mV}) = 0.631\frac{(\delta_0/\omega_{\rm m})}{0.0265}. \tag{3.9}$$

For ARP to properly work, the pulse and chirp need to be aligned to each other and the clocks on all of the rf sources need to be synchronized. The scheme for doing this is shown in Fig. 3.10; the DTG 5274 serves as the master clock for both of the HP signal generators which are connected to it as shown in Fig. 3.10. This configuration will allow the signal generators to be synchronized to each other even if the DTG 5274 is turned off or becomes disconnected. With the clocks synchronized, the phase of the rf signal from the HP signal generators can be reliably controlled in 1° increments by computer through a Prologix GPIB adapter and a Pascal-based program (EZGPIB). Adjustment of the phase will change the alignment of the chirp with respect to the pulse.

3.3.2 Transport of the Light

After the ARP pulses are properly created, each beam is amplified by its own 4W fiber amplifier (FA) to a desired power. Each emerges from the FA with a linear polarization, and then passes through a half-waveplate and a polarizing beam splitter (PBS) to allow for control of the optical power delivered to the experiment (see Fig. 3.9). The fraction of light not sent to the experiment is coupled into an optical fiber where it sent to a fast photodiode and the scanning Fabry-Perot to be characterized (See Sec. 4.1).

The light sent to the experiment is then magnified by a spherical telescope to have a beam waist of 3.85 mm for the Litho diode beam and 3.2 mm for the ARP diode beam. Thus its intensity profile is given by,

$$I = I_0 \exp\left(-\frac{2(x^2+y^2)}{{\rm w}^2}\right), \tag{3.10}$$

where w is the waist of the beams.

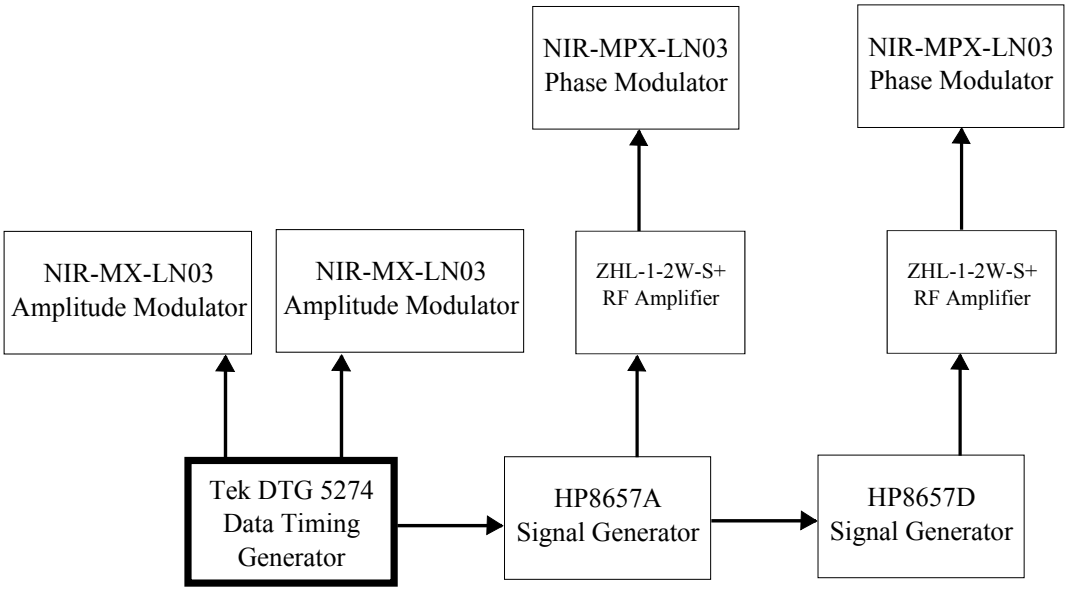

Figure 3.10: The setup for the rf signal generation used in this experiment. The NIR-MX-LN03 amplitude modulators are driven by a single Tektronics DTG 5274 data timing generator, whose internal control sets the rf pulse timing and thereby the optical pulse timing. The DTG also serves as the master clock for the HP signal generators which drive the NIR-MPX-LNO3 phase modulators.

The relationship between the intensity and the Rabi frequency is given by

$$\frac{I}{I_{\rm sat}} = 2\left(\frac{\Omega}{\gamma}\right)^2, \tag{3.11}$$

where $\gamma = 2\pi \times 1.62\,\mathrm{MHz}$ is the natural linewidth of the transition and $I_{\rm sat} \equiv (\pi hc)/3\lambda^3\tau = 0.167\,\mathrm{mW/cm^2}$ for the $2^3\mathrm{S}_1 \rightarrow 2^3\mathrm{P}_2$ in He^*. Therefore the average power of amplitude modulated light whose period is T, is given by

$$\begin{aligned}
\bar{P} =& \frac{1}{T}\int_0^T \int_{-\infty}^{\infty}\int_{-\infty}^{\infty} I_0(t)\exp\left(-\frac{2(x^2+y^2)}{\mathrm{w}^2}\right)dxdy\;dt \\
=& \frac{\pi}{2}\mathrm{w}^2\frac{1}{\mathrm{T}}\int_0^{\mathrm{T}} \mathrm{I}_0(\mathrm{t})\mathrm{dt} \\
=& \frac{\pi \mathrm{w}^2 \mathrm{I}_{\rm sat}}{T}\int_0^T \left(\frac{\Omega(t)}{\gamma}\right)^2 dt.
\end{aligned}$$

In the experiment $\Omega(t) = \Omega_0 \sin \omega_m t$ and $T = 4T_P = 4\pi/\omega_m$ so, the average power becomes

$$\begin{aligned}\bar{P} =& \pi \mathrm{w}^2 I_{\mathrm{sat}} \frac{\Omega_0}{\gamma} \cdot \frac{1}{T} \int_0^{T_P} \sin^2(\omega_m t)\, dt \\ \bar{P} =& \frac{\pi}{8} \mathrm{w}^2 I_{\mathrm{sat}} \left(\frac{\Omega_0}{\gamma}\right)^2 \end{aligned} \tag{3.12}$$

The Rabi frequencies of the two beams should be identical, therefore the average power for the two beams must be adjusted to compensate for the difference in the beam sizes

$$\begin{aligned}\frac{\bar{P}_{\mathrm{ARP}}}{\mathrm{w}_{\mathrm{ARP}}^2} =& \frac{\bar{P}_{\mathrm{Litho}}}{\mathrm{w}_{\mathrm{Litho}}^2} \\ \bar{P}_{\mathrm{ARP}} =& \left(\frac{\mathrm{w}_{\mathrm{ARP}}}{\mathrm{w}_{\mathrm{Litho}}}\right)^2 \bar{P}_{\mathrm{Litho}} \\ \bar{P}_{\mathrm{ARP}} =& \left(\frac{0.32\,\mathrm{cm}}{0.385\,\mathrm{cm}}\right)^2 \bar{P}_{\mathrm{Litho}} = 0.69\ \bar{P}_{\mathrm{Litho}} \end{aligned} \tag{3.13}$$

Following the telescopes, the light passes through a quarter-wave ($\lambda/4$) plate, which changes the polarization from linear to σ^+. This drives the $2^3\mathrm{S}_1 \rightarrow 2^3\mathrm{P}_2$, $\Delta m_j = +1$ transitions in He*. After the $\lambda/4$ plate, the beams pass through 4 mm slits designed to occlude the edges of the Gaussian beams as shown in Fig. 3.9. This limits the interaction time of the experiment to $\approx 4\ \mu s$ (40 lifetimes) for atoms with $\mathbf{v}_\ell = 1000\,\mathrm{m/s}$. These slits are placed as close to the atomic beam as possible ($\sim 15\,\mathrm{cm}$) to reduce the effects of diffraction.

Chapter 4

Measurement of the ARP Force

Measurement of the Adiabatic Rapid Passage (ARP) force was first performed in the 1996 by Ekstrom *et al.* [44]. A highly collimated beam of He^* traversed a tightly-focused laser beam at its Rayleigh length, the part of the beam that has the strongest wavefront curvature. The wavefront curvature caused the atoms to experience a Doppler shift that changed as they traversed the light beam and thus was dependent on their positions in it. A full transit of the laser beam resulted in the atoms experiencing both a frequency sweep and an amplitude modulation, causing the atoms to experience a force via the ARP process. It was observed by the deflection of the atomic beam.

In our laboratory the first measurement of the ARP force was performed in the early 2000's, and was achieved through modulation of the injection current of a diode laser, thereby producing the frequency sweep [27]. Since then, the techniques used to measure and produce the ARP force have been further refined, and a better understanding of ARP process has been developed [14, 32, 45].

4.1 Characterization of the Light

Due to the unique structure of the ARP pulses (see Chap. 3) and the strong sensitivity of the ARP force to the shape and frequency chirp, it is necessary to properly characterize the light pulses used in this experiment. The characterization of the amplitude modulation is performed by monitoring the light's intensity profile with a fast photodiode. This is done with either a Thorlabs DET08CFC or DET010CFC fast photodiode. The bandwidth of

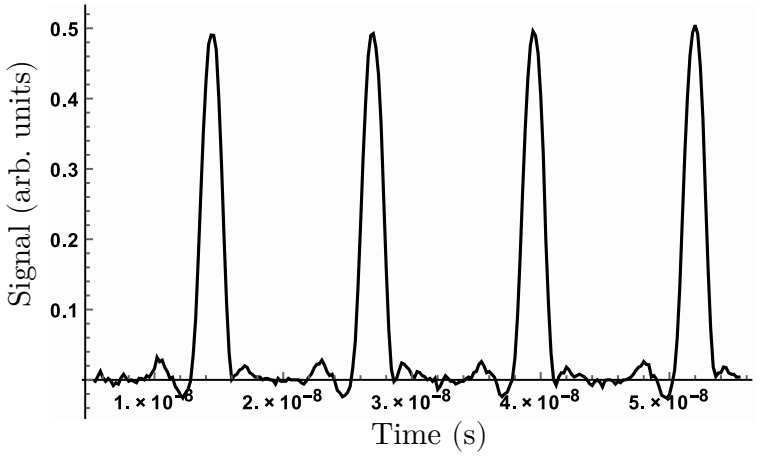

Figure 4.1: The intensity profile of good optical pulses used in this experiment. A Thorlabs DET08CFC photodetector was used to measure the light and a Tektronics TDS 3054 was used to take the data.

these photodiodes is 5 GHz and 1.2 GHz respectively and their outputs are monitored on a Tektronics TDS 3052 500 MHz oscilloscope. By monitoring the shape of the pulse's intensity profile, any drift of the amplitude modulator's external DC voltage will be seen as a distortion in the pulse shape and thus can be corrected. A drifting DC voltage will no longer cause the interference of the light in the two arms of the amplitude modulator to perfectly cancel and the resulting optical pulse will either have a reduced amplitude or a large DC offset. Figure 4.1 shows a sample trace of properly shaped ARP pulses used in this experiment. A second way that the amplitude modulation can be monitored is by looking at the frequency spectrum of the pulse train. A home-built, scanning Fabry-Perot (FP) interferometer (see Fig. 4.2) is used to look at the frequency spectrum (Fig. 4.3). From the frequency spectrum of the pulse train, it is possible to determine whether or not there is any residual light caused by an improper DC voltage, by comparing at the height of the carrier frequency peak with respect to the other peaks of the spectrum.

The measurement and characterization of how well the chirp and pulse are aligned is a non-trivial task requiring use of the same scanning FP used to measure the pulses' spectra. An in-depth analysis of the the expected FP spectrum for sinusoidally-amplitude modulated and phase modulated light is covered in [23, 38]. The basic overview is that for a properly aligned chirp, the spectra should be symmetric (Fig. 4.4a), and for a chirp which is not, the spectra will be skewed in one direction or the other (Fig. 4.4b).

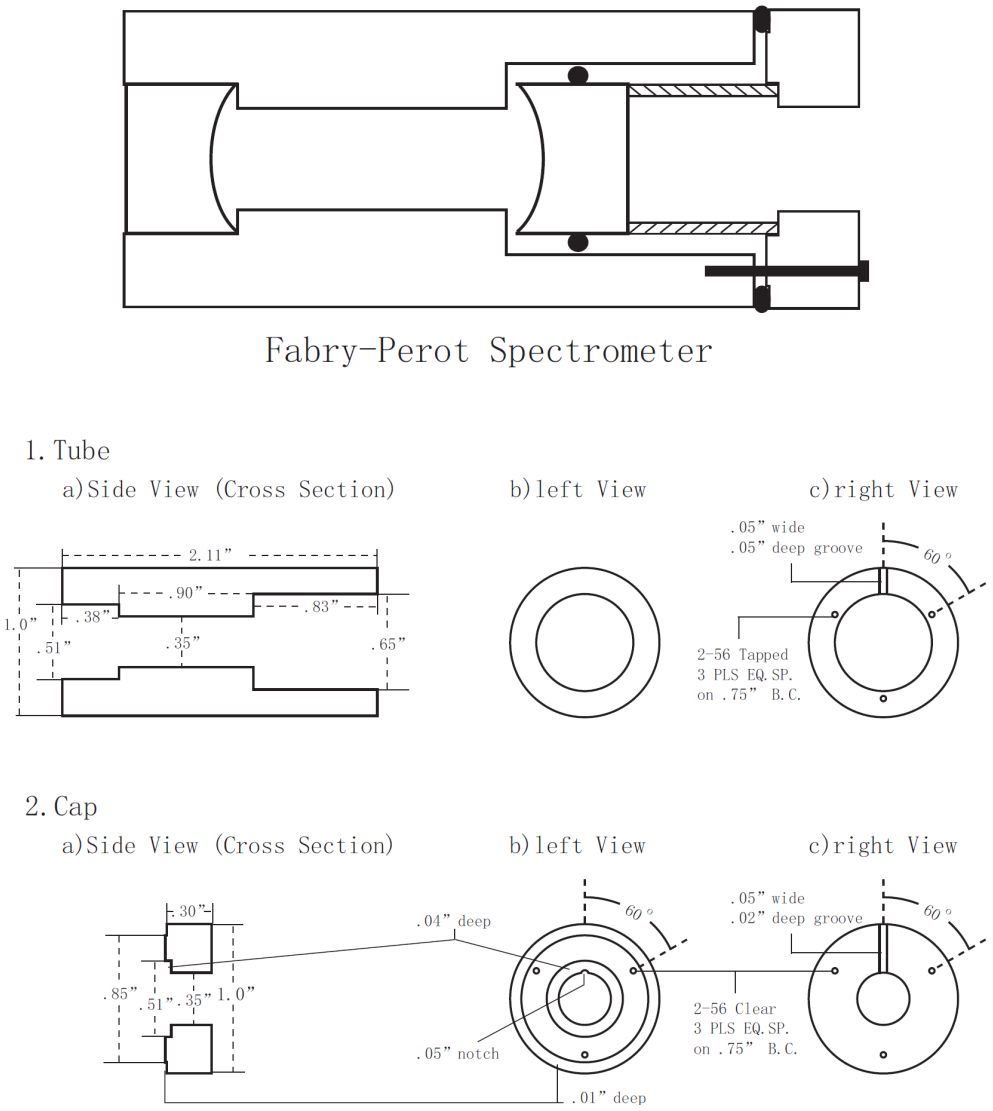

Figure 4.2: Schematic of the Fabry-Perot interferometer used to characterize the ARP light. The length of the cavity is 25 mm, the mirror diameters are 12.7 mm, with a focal length of 25 mm and thickness of 9.5 mm. The FP has a free spectral range of $\approx 3\,\mathrm{GHz}$ and a resolution $\sim 30\,\mathrm{MHz}$. Taken from the thesis of D. Stack [38].

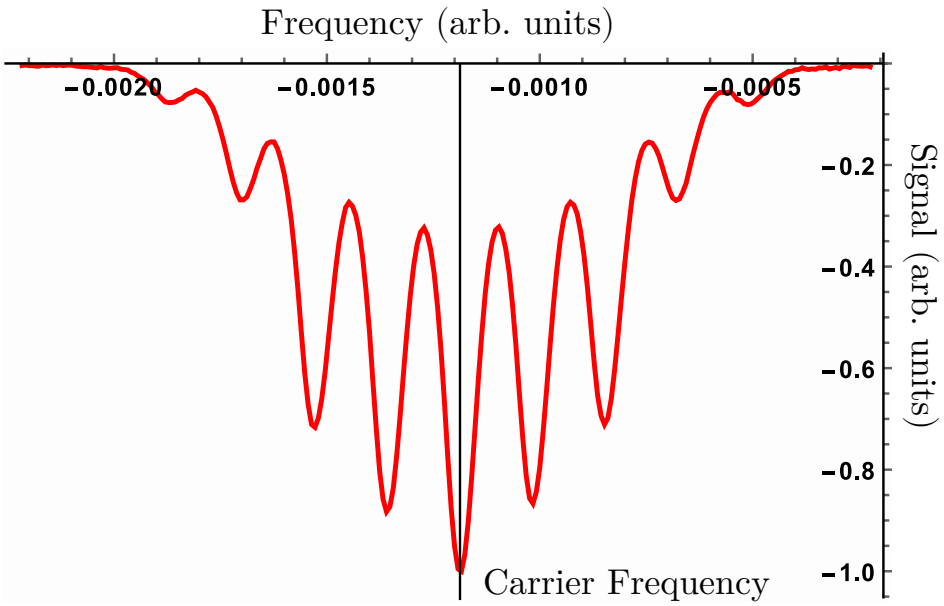

Figure 4.3: Measured Fabry-Perot spectrum for a train of properly shaped pulses. The peaks are separated by the repetition rate of 80 MHz and the full width of the signal corresponds to the bandwidth of 320 MHz. A Tektronics TDS 3054 was used to take the data.

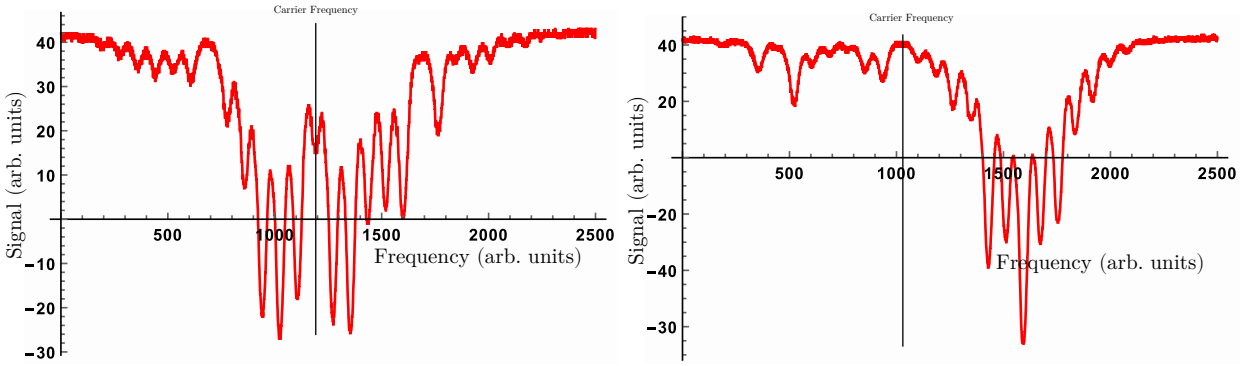

(a) Properly Aligned Chirped Pulses (b) Misaligned Chirped Pulses

Figure 4.4: Part (a) shows the Fabry-Perot spectrum for an ARP pulse with the frequency chirp properly aligned to the amplitude modulation. Note the spectrum is roughly symmetric around the identified carrier frequency. Part (b) shows a spectrum for a misaligned frequency chirp. Note that they spectrum is not symmetric about the carrier, and instead the spectrum resembles a detuned unchirped pulse. Both signals were taken with the same Tektronics TDS 3052 oscilloscope.

4.2 Data Collection

Previous methods used to measure the ARP force mainly involved the systematic changing of Ω_0 and δ_0 while keeping the lasers locked either on resonance or to a simulated Doppler shift given by a frequency offset of $\pm\delta$. This method worked well for the initial studies of ARP, but it is not a very efficient method for measuring the velocity dependence of the force due to the need to consistently relock the laser to a different detuning after every data set. The thesis of D. Stack outlines the results of measuring the force in this way, and as shown, it can take upwards of several weeks to measure a single force *vs.* velocity profile [38].

A means of continuously varying the Doppler shift was needed to speed up the data collection process. The first implementation of this method was used to collect preliminary velocity profiles shown in [38]. The method, described in the next section involved fixing the values of Ω_0 and δ_0 and simulating a Doppler shift by varying the detuning of the laser pulses incident on the atoms.

4.2.1 Simulating the Doppler Shift

For these experiments, an atomic velocity is simulated through the Doppler shift, and uses oppositely-detuned, counter-propagating optical pulses. The detuning of these pulses can be varied by slowly changing the sizes of the extended cavities of the diode lasers. A slow ($\sim 0.1\,\mathrm{Hz}$) periodic ramp signal is applied to the PZT of each diode laser causing a continuous variation of the lasers' frequencies.

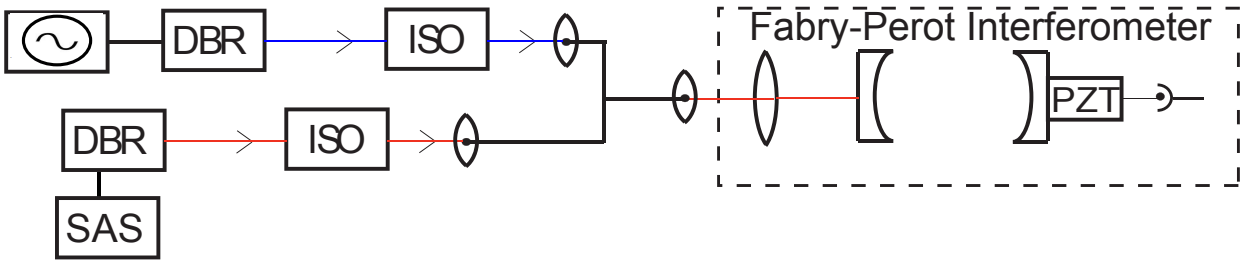

Figure 4.5: Diagram of the method used to measure the response of the extend cavity PZT and to calibrate the frequency detuning. Two lasers are coupled into the same scanning FP, one is locked to the atomic transition through SAS while the other is frequency swept by changing the voltage applied to the PZT in the external cavity. By monitoring the FP signal, the calibration from voltage on the PZT to frequency detuning can be measured. Taken from [38]

It is necessary to accurately measure the change in the laser cavity sizes, and thus the change in frequency, due to the changing voltage applied to the PZTs. Fig. 4.5 shows a schematic diagram of the the method used to measure this response using cw lasers. The ramp signal, supplied from a Stanford Research Systems DS345 function generator and amplified by a home-built voltage amplifier, drives the PZT of one laser; the other laser is locked to the SAS peak. Both laser outputs are then coupled into a scanning Fabry-Perot (FP) interferometer. The locked laser serves as the reference; the difference between its frequency and that of the sweeping laser will eliminate any possible drifts in the peak positions due to temperature changes. During the measurement, the output light from the FP is detected using a photodiode and the signal is monitored by a Tektronix TDS 210 oscilloscope. The oscilloscope trace is periodically saved ($\sim 30\,\mathrm{ms}$), which is longer than the scan rate of the FP ($\sim 500\,\mathrm{Hz}$) but much shorter then the diode's frequency sweep ($0.1\,\mathrm{Hz}$). A pair of Lorentzians can be fit to the saved scope traces, and from these fits a conversion factor of voltage to frequency can be obtained. Figure 4.6a shows an example of the Lorentzian fit [38].

An absolute frequency scale can be obtained by applying a signal to the phase modulator of locked laser. The phase modulation will create sidebands of $\pm\omega_m$ which can be seen on the FP signal. Multiple Lorentzians can be fit to the phase modulated signal and the distance between these peaks provides the $160\,\mathrm{MHz}$ conversions factor (See Fig. 4.6b). For the ARP diode, the conversion factor was found to be $29(1)\,\mathrm{MHz/V}$ and for the Litho diode $356(1)\,\mathrm{MHz/V}$. The large difference between the two diodes is due to the design of the home-built electronics which were used to frequency lock the lasers to a reference signal.

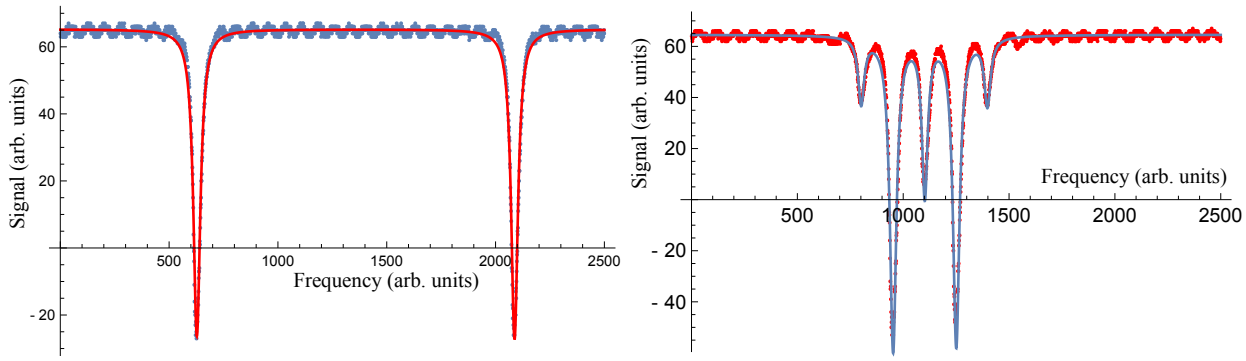

(a) FP Trace of Sweep Measurement (b) FP Trace of Phase Modulated Light

Figure 4.6: Figure 4.6a) shows a scope trace and fit for two cw lasers offset in frequency by some arbitrary value. In the sweep calibration, the peak on the right will move as the voltage on the PZT is changed, while the peak on the left is locked to atomic resonance. By measuring the distance between these peaks for several cycles of the PZT ramp, a calibration of voltage to frequency can be made. Figure 4.6b indicates how the frequency change is calibrated. It shows the FP signal for a single phase modulated laser (modulation frequency is 160 MHz) where the spacing between the peaks must be 160 MHz. The line is a fit of multiple Lorentzians on the scope signal.

4.2.2 Detection of the ARP Force

After leaving the optical interaction region the deflected atoms travel a distance of 33 cm down the vacuum system and are incident on an MCP/PS, described in Sec. 3.1.3. During these experiments, the MCP was run at -1100 V while the PS was at $+1900$ volts. An image of the phosphor screen is captured using a 320×240 CCD camera, whose output is read into the computer. During an experimental run, a LabView program is used to read in the voltages applied to each PZT and the voltages from the SAS signal every 33 ms and to save them to a text file. This is done through use of a National Instruments Data Acquisition (NI-DAQ) card. The LabView program also initializes a video capture of the phosphor screen via the open source program Virtual Dub. For the data presented in this thesis, all experimental runs lasted for 100 s.

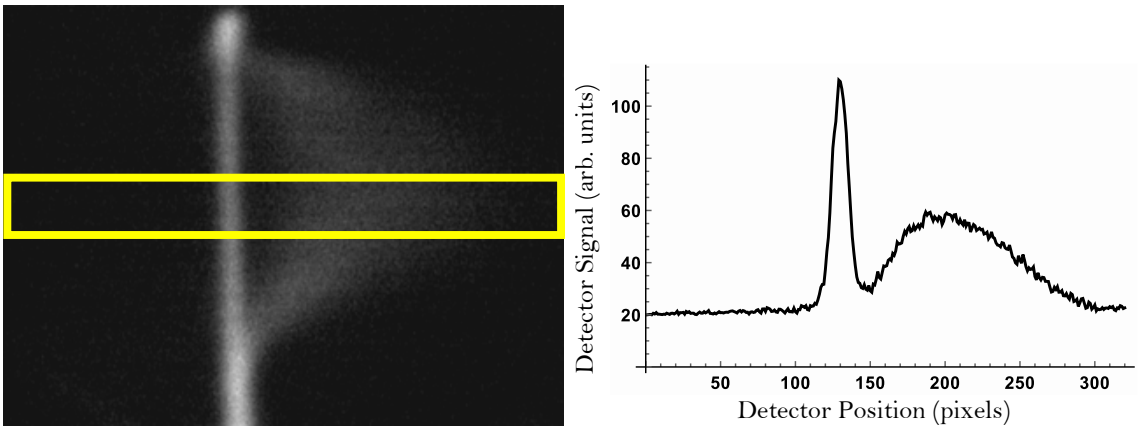

(a) Phosphor Screen image (b) Averaged lineout

Figure 4.7: Part (a) shows an image of the phosphor screen with deflected atoms. The bright line in the images is the image of the 250 μm slit used to define the atomic beam. The atoms are predominately pushed to the right, seen by the smeared out grey. The yellow box indicates the region selected and averaged together to produce the lineout shown in part (b).

4.3 Data Analysis

The data collection starts with taking the video file of the MCP/PS screen and cropping out the narrow region of interest. The light beams have a circular Gaussian beam cross section which is modified in the horizontal direction through the use of 4 mm slits as discussed previously. The vertical direction still maintains the Gaussian shape, but near the center of the beam, in a small ($\sim$ 10 pixel) region the intensity is approximately uniform. This region is cropped out of the video file, and the rows comprising it are then averaged together to help eliminate noise from the phosphor screen. Figure 4.7 shows an example of the cropped region compared to the whole screen (4.7a) and also an averaged lineout (4.7b).

The data file, which has the PZT and SAS voltage data, is the other key component in the data analysis process. The information in this file can be used to identify the points when the lasers cross resonance and determine the range of the velocity sweep. The voltage on the PZT corresponding to resonances is found by looking at the SAS voltage signal. Using this PZT voltage and the calibration for each laser, the voltage *vs.* time signal can be converted into a Doppler frequency *vs.* time ramp signal. Figure 4.8 shows an example of the SAS signal on top of the Doppler frequency *vs.* time ramp signal.

Using the frequency *vs.* time and the lineouts, it is possible to average the 10 cycles of the

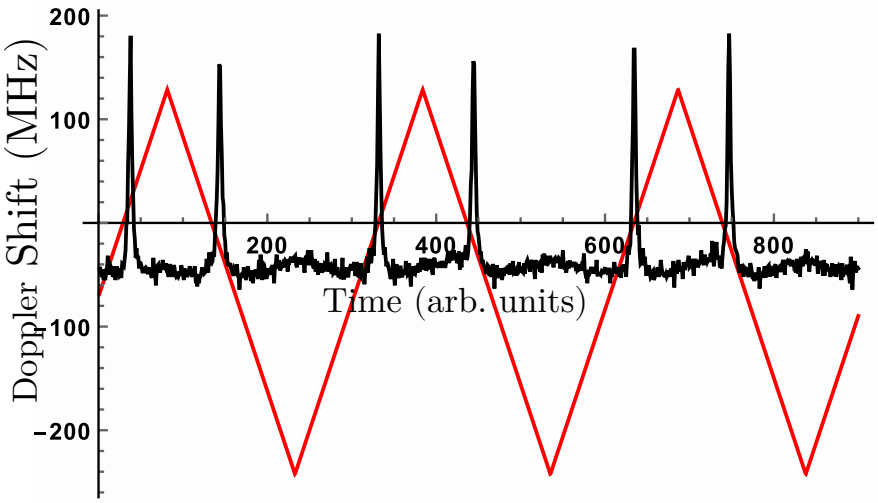

Figure 4.8: Scope trace showing the simulated Doppler shift due to voltage applied to the PZT for the Litho laser plotted with the SAS signal for the same laser. There appears to be a systematic offset in that it only occurs on the downward ramp. Because it is consistent it should only influence the absolute velocity scale.

velocity sweep and make a density plot of detector position and atom number *vs.* Doppler frequency. However, there are experimental difficulties which arise from the averaging process which must be accounted for in the data analysis. The first of these issues is that the camera and video capture program do not initialize at the same time as the voltage data capture begins; therefore it is required to use an offset to the frequency signal to align with the atomic signal. The next concern is that the frame rate of the video capture is not exactly 30 fps and, in fact, it can vary from run to run depending on what the computer has running in the background. In addition, the frame rate can even vary during the 100 s data run; this is the most difficult problem to deal with. The frame issues are corrected by using an average frame rate for the data run. These issues with the averaging in the data analysis are a major source of noise in the final results of the experiment. The inconsistent frame rate will artificially broaden any peaks in the signal due to the improper overlap of the features for all 10 cycles. The absolute velocity values also have some uncertainty due to the lack of a proper trigger in the data collection process. Nonetheless all of the uncertainty associated with the data analysis amounts to between $5 - 10\%$.

Chapter 5

Numerical Simulation

Due to the complexity of the ARP process, it is necessary to run numerical simulations of the ARP force to enhance understanding of the experimental results. This chapter provides an overview of how these numerical simulations are performed along with an analysis of the results they provide.

5.1 The Simulation

The Optical Bloch Equations are numerically solved in the interaction picture using the Fortran-90 subroutine BIM [46]. In the interaction picture, the torque vector $\mathbf{\Omega}(t) = \{\Omega_{\text{real}}, \Omega_{\text{imag}}, -\delta\}$ is given as follows

$$\Omega_{\text{real}} = |\Omega_0 \sin(\omega_m t)| \cos(\alpha(t)) \tag{5.1a}$$

$$\Omega_{\text{imag}} = |\Omega_0 \sin(\omega_m t)| \sin(\alpha(t)) \tag{5.1b}$$

$$\delta = 0 \tag{5.1c}$$

where

$$\alpha(t) = -\left(\delta_0/\omega_m\right) \sin(\omega_m t) \pm \mathbf{k} \cdot \mathbf{v}_{\text{t}} t \pm \phi/2 \tag{5.2}$$

Here the frequency detuning ($\delta(t)$) is moved from the 3rd component of the torque vector into the complex phase of the Rabi frequency $\alpha(t)$. The frequency sweep used in the ARP process is given by $(-\delta_0/\omega_m) \sin(\omega_m t)$ and the sweep direction is determined by the sign of

δ_0. The contribution from Doppler shifts is given by $\mathbf{k} \cdot \mathbf{v}_t t$ where $\mathbf{k}$ is the wave vector and $\mathbf{v}_t$ is the atom's transverse velocity, and the phase difference between the pulses is ϕ. Using this torque vector, the OBEs in the interaction picture are written as.

$$\dot{u} = \Omega_{\text{imag}} w - (\gamma/2) u \tag{5.3a}$$

$$\dot{v} = -\Omega_{\text{real}} w - (\gamma/2) v \tag{5.3b}$$

$$\dot{w} = \Omega_{\text{real}} v - \Omega_{\text{imag}} u - \gamma(w + 1) \tag{5.3c}$$

In the simulation, the ARP process is broken up into time units of π/ω_m, of which there are a total of 4 per pulse pair including dead time. After each time unit, the resulting Bloch vector $\mathbf{R} = \{u, v, w\}$ is used to calculate the force (See Sec. 5.1.1) on the atom and the solution serves as the initial state of the atom for the next time unit. The parameters for the calculation are given in Table 5.1.

Parameter	Description
$npulses$	The number of pulse pairs which interact with the atom
ω_m	The modulation frequency
Ω_0	The peak Rabi frequency of the pulses
δ_0	The amplitude of the frequency sweep
$\mathbf{v}_t$	The transverse velocity of the atom
γ	The spontaneous emission decay rate
ϕ	The relative phase difference between sequential pulses

Table 5.1: Table of the simulation parameters.

Besides varying the normal experimentally accessible parameters Ω_0, δ_0, and ω_m, the simulation gives us the ability to change the parameters which cannot be varied in the experiment either easily or at all such as γ, $npulses$, and ϕ. In the experiment, the value of the spontaneous decay rate (γ) is fixed by the atom, but in the calculation the value can be changed making it easier to understand the role spontaneous decay plays in the average force. This is discussed in great detail in the thesis of D. Stack [38].

Experimentally ϕ is determined by both the position of the atom when the light interacts with it, and also by the coherence between the two light pulses that come from different lasers and compose a single ARP cycle. The spatial extent of the atomic beam is much larger than

the wavelength of the light, so it is nearly impossible to fix the position of the atoms on a sub-wavelength scale. Therefore, it is assumed that throughout the experiment all values of ϕ are probed. To reproduce this in the simulation, ϕ is calculated for 25 equally spaced values ranging from 0 to 2π, and the results are then averaged together. The simulation assumes perfect coherence between the two pulses. In this experiment, there is virtually no coherence since the pulse train in each direction originates from its own independent laser. This problem could be overcome by phase locking the lasers together, but the means to do this were not available for this thesis work.

5.1.1 Calculating the Force

For these ARP simulations, the force is calculated from the change in the value of w, the 3rd component of the Bloch vector. This is equivalent to using the Ehrenfest theorem shown in Sec. 2.1.1

$$\text{If } (i \bmod 4) = 1, \text{ then}$$

$$d\mathbf{F} = (w_{\mathrm{i}} - w_{(\mathrm{i}-1)})\frac{\hbar k}{2}\frac{\omega_m}{\pi} \tag{5.4}$$

$$\text{Else If } (i \bmod 4) = 2, \text{ then}$$

$$d\mathbf{F} = -(w_{\mathrm{i}} - w_{(\mathrm{i}-1)})\frac{\hbar k}{2}\frac{\omega_m}{\pi} \tag{5.5}$$

$$\text{Else}$$

$$d\mathbf{F} = 0 \tag{5.6}$$

This method assumes that, although the atom can decay during the time when there is no light on it, the change in the force due to the decay is negligible, and will not influence the value of the average force. The sign change between Eq. 5.4 and Eq. 5.5 of the force calculation is due to the fact that for an atom in the ground state, experiencing a perfect inversion $\Delta w = 1-(-1) = 2$, whereas for an atom in the excited state, undergoing a similar inversion $\Delta w = -1-1 = -2$.

5.1.2 Dragged Atom vs. Atomic Motion

The standard method of calculating forces on atoms due to an optical field is to use what is called the dragged atom model. This model ignores the change in atomic velocity due to the interaction with the light. It is a good approximation when used to calculate the standard radiative force or forces of a similar magnitude over a short interaction time. This is because the velocity change caused by these types of forces result in a Doppler shift which is typically smaller than or comparable to the natural linewidth of the atomic transition. The dragged atom model has been previously used to calculate the ARP force [32]; however, this is not appropriate for our experiment. For the interaction equal to the experiment (about 320 pulse pairs), the Doppler shift from the changing atomic velocity is substantial.

$$\begin{aligned} \mathbf{F}_{\max} &\rightarrow 320 \text{ pulse pairs} = 640 v_{\text{recoil}} \\ \Delta\mathbf{v} &= 640(9.2\,\text{cm/s}) = 58.8\,\text{m/s} \\ \delta_{\max} &= \mathbf{k}\cdot\mathbf{v} \\ &= (58.8\,\text{m/s}) * (2\pi/1.08\mu\text{m}) \approx 2\pi * 54\,\text{MHz} \end{aligned} \tag{5.7}$$

whereas $\gamma = 2\pi * 1.62\,\text{MHz}$. In the case of maximum force or even half of the maximum force, the Doppler shift is on the order of the modulation frequency ω_m and cannot be neglected throughout the force calculation.

To account for the moving atom, the simulation changes the value of the transverse velocity right after calculating the force.

$$\mathrm{v_{(i+1)}} = \Delta\mathrm{v} + \mathrm{v_i} = \frac{2(\mathrm{dF})\mathrm{t_{pulse}}}{\mathrm{M}} + \mathrm{v_i} \tag{5.8}$$

where $\mathrm{v_i}$ is the velocity used for the time interval used to calculate the current force, v_{i+1} is the velocity for the next time interval, M is the mass of the atom (for He $M = 6.64648 * 10^{-27}\,\text{kg}$), dF is the force on the atom through the most recent time interval, and $\mathrm{t_{pulse}}$ is the time of the pulse/interval of time (π/ω_m). Besides changing the value of the transverse velocity of the atom for the calculation, the changing transverse velocity also changes the relative phase difference between the two pulses. This change is easily calculated

$$\phi_{i+1} = \phi_i + 2\pi\frac{\pi}{\omega_m}\frac{\Delta\mathrm{v}}{\lambda} \tag{5.9}$$

where Δv is the change in the transverse velocity due to the interaction with a single pulse.

5.2 Calculating the Final Atomic Distribution

To better compare the results of the simulation to the experiment, it is necessary to convert the force and final transverse velocities that are output by the simulation into measurable quantity in the experiment. This is done by using the atom's final transverse velocities and projecting them through simple ballistics to a downstream detector, as diagrammed in Fig. 5.1.

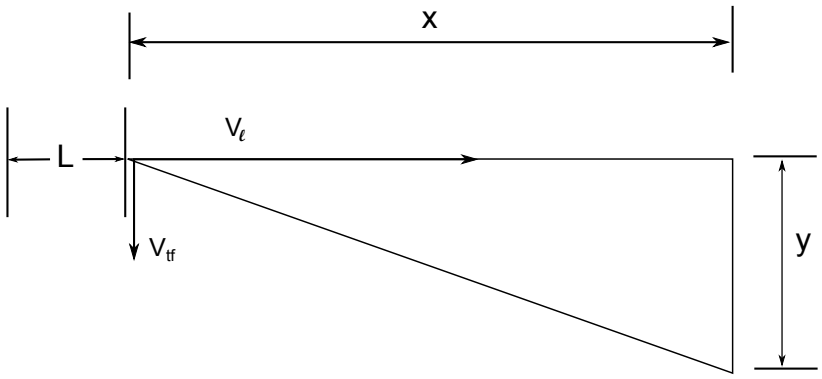

Figure 5.1: Schematic representation of the atoms trajectories as they leave the interaction region. The atoms leave the interaction region (L), with longitudinal velocities (v_ℓ) and transverse velocities (v_{tf}). The atoms then travel a longitudinal distance (x = 33 cm) to the detector. By calculating y we can simulate the results seen in the experiment.

The calculation of the transverse displacement of the atom is

$$y = \frac{v_{tf}}{v_\ell} * x \tag{5.10}$$

$$v_\ell = L/t;\ t = T * npulses$$

$$y = x\frac{T}{L}(v_{tf}) * npulses \tag{5.11}$$

where *npulses* is the number of pulse pairs that interact with the atom, T is the period of a pulse pair ($4\pi/\omega_m$), v_{tf} is the final transverse velocity, v_ℓ is the longitudinal velocity, x is the flight distance of the atom after the interaction region (33 cm), and y is the position on the detector. In the experiment, the initial transverse velocity is effectively changed by

varying the detuning of the lasers. Thus the Doppler shift on the atoms is simulated and for this reason only the change in the transverse velocity due to the interaction with the light and not the absolute velocity is desired, therefore $v_{tf} \rightarrow v_{tf} - v_{ti} = \Delta v_t$. The initial starting value of y is not considered because in the experiment the atoms pass through an atomic slit which is only 250 μm wide, therefore the any variation on y's starting value will have little influence on the final y position of the atoms.

5.2.1 Longitudinal Velocity Distribution

Up to this point in the simulation, the longitudinal velocity has been assumed to have a single value, and the choice of this velocity is determined by the number of pulse pairs experienced by the atoms as they traverse the fixed size of the light beams in the calculation. However, as explained in Sec. 3.1.2, the atomic beam in the experiment has a longitudinal velocity distribution with a shape approximately matching Fig. 5.2.

By using the distribution of longitudinal velocities of the atoms to weight the results of where the atoms land on the detector, further insight into the experimental results can be obtained. A density plot with initial velocity on the x-axis, the position where atoms will land on the detector on the y-axis, and the weighted atom number given by the longitudinal velocity distribution on the z-axis, is used to show the effect caused by the longitudinal velocity distribution. A plot can be made from the raw data of the experiment, thus providing a direct comparison between simulations and experiment.

The process used to weight the results is to first take the position data for all velocities ranging from 2000 m/s (160 pulsepairs) to 570 m/s (540 pulsepairs) and scale them by $N(v)dv$ obtained from Fig. 5.2. This process uses discrete values for longitudinal velocities corresponding only to an integer number of pulse pairs. The position on the detector is then broken up into discrete bins and the atom density is just the summation of all values that fall inside the bin.

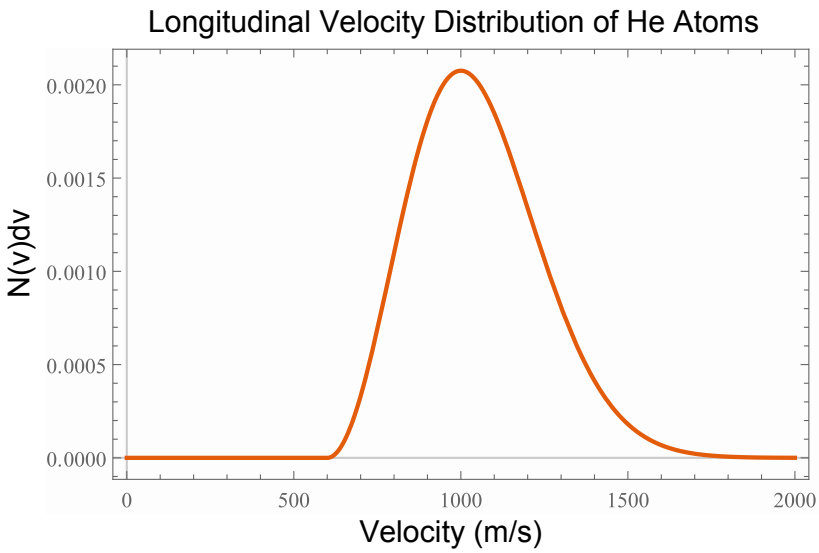

Figure 5.2: An approximate fit of the He* longitudinal velocity distribution from our atomic beam source. The peak of the distribution is at $\sim 1000\,\mathrm{m/s}$, with a minimum value of $600\,\mathrm{m/s}$ and maximum value of $\sim 1800\,\mathrm{m/s}$.

5.3 Simulation Results

The numerical simulations are very powerful tools that have produced a large number of results and provide great insight into how the ARP force works. This section will touch on three such results, looking into their effects on the ARP process.

5.3.1 Effects of Atomic Motion

Fig. 5.3 shows the influence that atomic motion has on the simulation results. These plots show the average force on an atom after a given number of pulse pairs, in this case 320 pulses pairs, plotted against the atom's initial transverse velocity. The major differences between the two are the shift of the peak from $\mathbf{v} = 0$ to a value of $\mathbf{v} < 0$, the unexpected oscillations which emerge at $|\mathbf{v}| > 300\,\mathrm{m/s}$, and the disappearance of the narrow resonances.

The shift of the peak to negative velocities is not an unexpected result. Consider the case of a positive force in the dragged atom picture, where an atom which starts at $\mathbf{v} = 0$ will experience an increase in its velocity. As the velocity increases the force will be reduced. Now consider an atom which starts with a velocity which is negative but still near the maximum of the dragged atom profile. The velocity increase due to the force on this atom will cause it

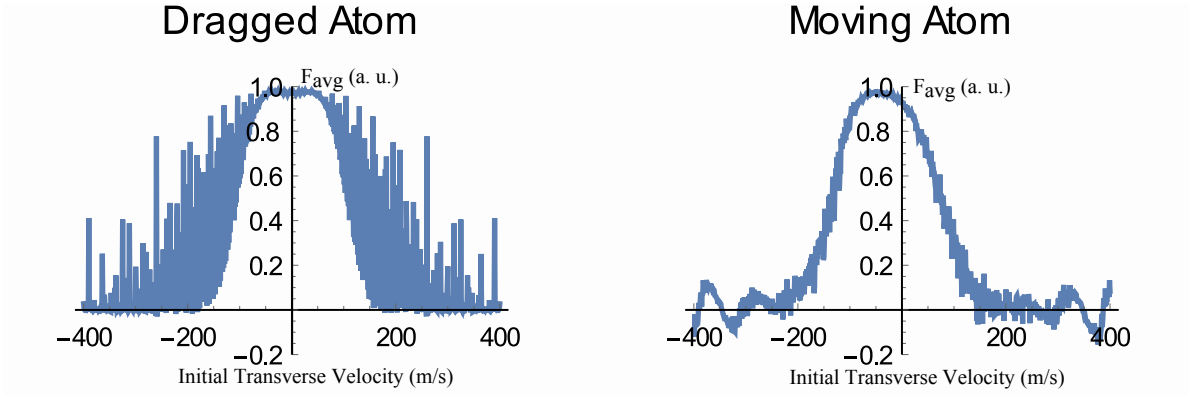

Figure 5.3: Force *vs.* velocity plots for the values $\Omega_0 = 3.37\ \omega_m$, $\delta_0 = 4.11\ \omega_m$, comparing the dragged atom to the moving atom. The x-axis shows the initial transverse velocity and the y-axis the average force after 320 pulse pairs in arbitrary units. The main differences are the disappearance of the narrow resonances seen in the dragged atom picture, the emergence of an oscillation at extreme velocities, and the shifting of the peak towards negative velocities for the case of positive force.

to experience an increasing force until sometime after its velocity gets larger than $\mathbf{v} = 0$ at which point it will also experience a decreased force. Thus the average force felt by such an atom will therfore be larger than the average force on an atom that starts at zero velocity.

The narrow resonances that are seen in the dragged atom picture are real enhancements of the force which arise due to multiple ARP processes. In the Bloch sphere picture, a moving atom is represented by allowing the sphere to rotate at a given rate. If the pulses interact with the sphere every integer number or rational fraction of this rotation rate, then after many sequences there will be an enhancement of the force. These features require many pulse pair interactions at fixed velocity to develop. Inclusion of the changing atomic velocity is equivalent to allowing the atom to sample many different velocities throughout the entire simulation time. By sampling different velocities after every pulse, a majority of the narrow resonances will wash out. Those that don't get washed out correspond to the strongest resonances, and so required fewer pulse pairs to develop. As such, they are broadened, and it is this broadening which is believed to be the source of the unexpected oscillatory features at extreme velocities. The period of these oscillations very closely corresponds to half the modulation frequency. However, the fact that the force has a negative average value in the vicinity of these features is not fully understood but the next section provides a possible explanation.

5.3.2 The Role of Phase

The role of the phase in the calculation has been previously addressed in detail [23, 32, 38]. This section will provide an overview of the previous work and expand on it, providing new results. The relative phase difference between the two pulses of a pair plays a very important role in determining the ARP force. The phase term ϕ in the calculation is best interpreted as a rotation of the torque vector by an angle ϕ about the polar axis. Therefore, for a pulse which fails to place the atom in either the ground, $\mathbf{R} = \{0, 0, -1\}$, or excited, $\mathbf{R} = \{0, 0, 1\}$ state, the relative phase of the subsequent pulse will greatly influence the trajectory of the Bloch vector during its interaction with the atom. This is most easily seen when a relative phase of π is considered. For a relative phase of π, the Bloch vector will traverse one side of the Bloch sphere during the first pulse and then follow an identical path except it will be on the opposite side of the Bloch sphere, 180° rotated from the first. This change in the torque vector will cause the trajectory of the Bloch vector during the second pulse to retrace the path followed during the first pulse, thereby returning it to the position it was in before the first pulse.

The complicated nature of the OBE's means that it is generally not easy to describe how the changing the phase term effects the trajectory of the Bloch vector, over multiple ARP sequences. By looking at the value of the Bloch vector before and after the atom interacts with the light field, it is possible to gain some qualitative insight into the role that phase plays in determining the value of the average force on stationary atoms ($\mathbf{v} = 0$). This is done by looking at the Bloch sphere in a 2-D plane, looking down the u-axis (See Figs. 5.4(a) and 5.4(c)) or the v-axis (See Figs. 5.4(b) and 5.4(d)). The points indicate the values of the Bloch vector at the end of the first pulse in the pair ((a) and (b)), and the end of the second pulse in the pair ((c) and (d)) evaluated for the parameters $\Omega_0 = 3.37\ \omega_m$, $\delta_0 = 4.85\ \omega_m$, $\phi = 10\pi/9$, and a total of 540 pulse pairs. Although not a good choice, the dragged atom model is used to for these images because it provides a clear, uncomplicated picture showing the emergence of circles on the sphere and agrees with the work in the appendix of [23]. Changing ϕ changes the the shapes of these circles, even going so far as to cause the circles to cross the equator. Crossing the equator implies that for some period of time the force is reversed, as shown in Fig. 5.5.

The complexity of the picture grows further when the motion of the atom is included. This can be seen in the example in Fig. 5.6, which uses the same parameters as those of

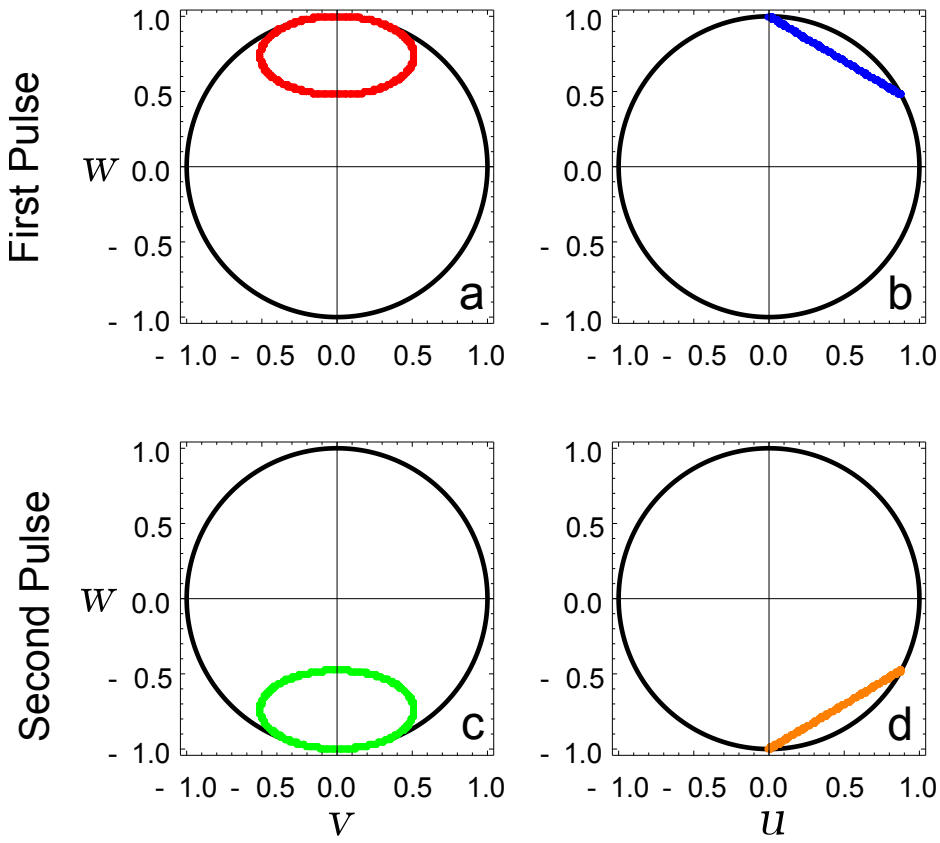

Figure 5.4: Plots showing the value of **R** after the first pulse ((a) and (b)) and second pulse ((c) and (d)) of the period. The points are plotted on a 2-D representation of the Bloch sphere looking down either the u or v axis. These calculations were run using the dragged atom model for the point $\Omega_0 = 3.37\ \omega_m$, $\delta_0 = 4.85\ \omega_m$ and $\phi = 10\pi/9$. A total number of 540 pulse pairs are plotted. The interesting result is that all of the points lie in a circle.

Fig. 5.4, except that the velocity change of the atom due to interaction with the light is taken into account. In this case, the relatively strong average force calculated for the dragged atom is drastically reduced for the moving atom. This is seen by looking at the points above and below the equator. For the dragged atom, they are near the poles implying a strong average force. But for the moving atom, they are confined to a region around the equator which implies an average force near zero. Just as with the dragged atom, a small change in ϕ can lead to a large change in these plots. The interesting cases to look at are those in which, after just a few pulse pairs, the Bloch vector ends in the southern hemisphere after the first pulse and in the northern hemisphere after the second pulse. When this happens, the force

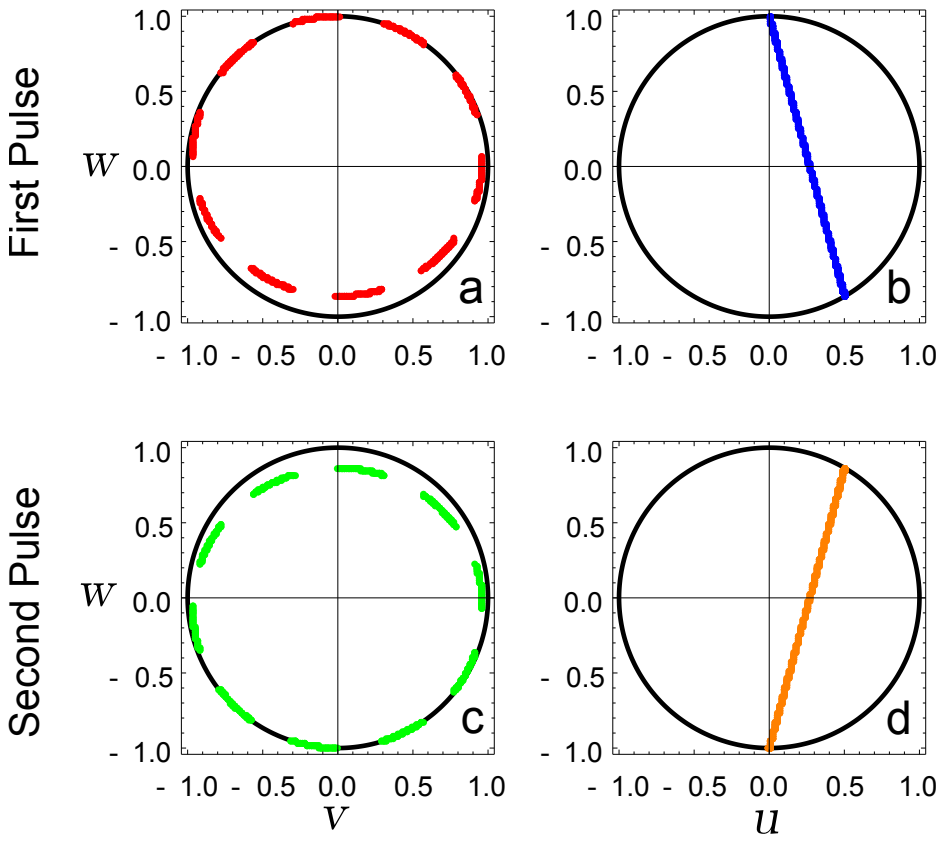

Figure 5.5: Plots showing the same information as Fig. 5.4 for the same calculation parameters except $\phi = 5\pi/4$. As can be seen, a small change of ϕ can drastically change the evolution of the Bloch vector over 540 pulse pairs. In this case, the fact that the final points cross the equator leads to a force which is reversed for certain points in the process.

direction is reversed. Thus it can be seen that the pulse timing is not the only parameter that defines the direction of the ARP force.

5.3.3 Reduced Force on v = 0 Atoms

Among the most revealing result from the simulations are those that show two peaks with a splitting in the force *vs.* velocity plot, such as Figs. 5.7, 5.8. This splitting is interesting because as δ_0 increases the splitting in the profile increases, and the force on atoms at $v = 0$ decreases until it is virtually 0. This can be seen by looking at Figures 5.7, 5.8 which show this effect at a fixed Rabi frequency and various values of δ_0, both without and with

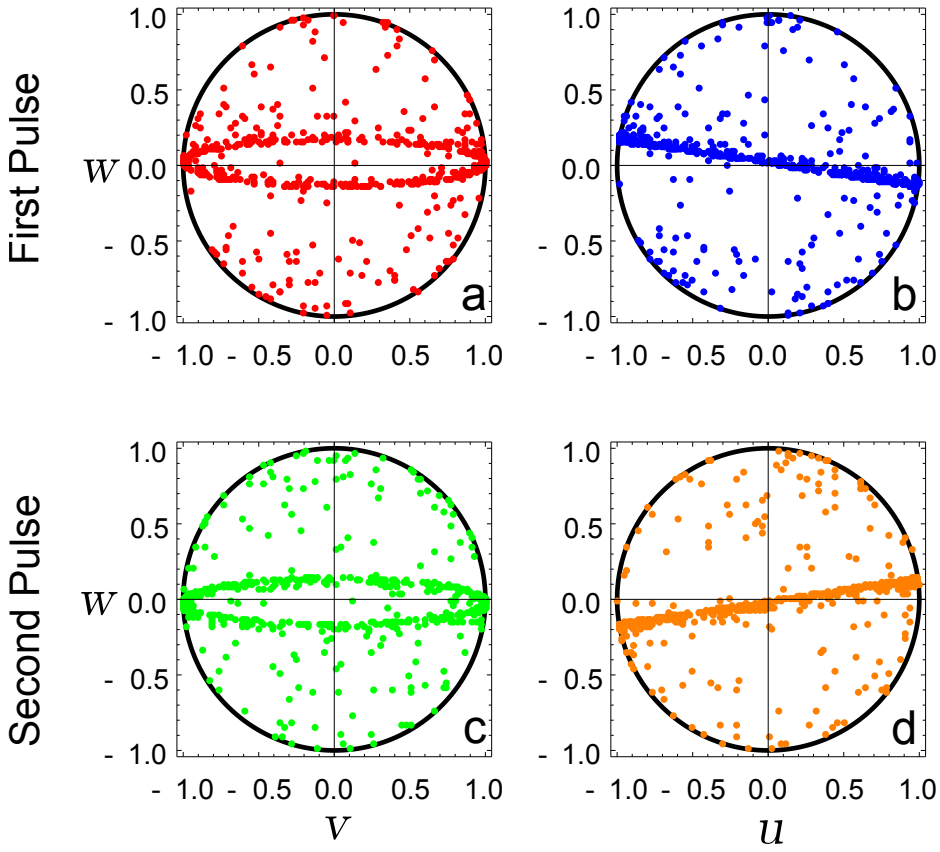

Figure 5.6: Identical plot to Fig. 5.4 except that this time the atomic motion is accounted for. By considering the velocity change due to the interaction of the atom with the force, the strong force seen for the dragged atom model is now reduced to nearly 0.

spontaneous emission respectively.

It is worth investigating what the relationship is between this splitting and the value of δ_0. To do this it is necessary to determine the location of the peaks. Only the peak of the final longitudinal velocity distribution is used, and the peaks are then identified by either picking the maximum by hand, or fitting the peaks to a Lorentzian function given by

$$f(\mathbf{v}, w_f) = \frac{w_f}{(\mathbf{v}+\mathbf{v}_0)^2 + w_f^2} \qquad \text{for } (\mathbf{v}+\mathbf{v}_0) < 0 \tag{5.12}$$

$$g(\mathbf{x}, w_f) = \frac{w_g}{(\mathbf{v}+\mathbf{v}_0)^2 + w_g^2} \qquad \text{for } (\mathbf{v}+\mathbf{v}_0) \geq 0 \tag{5.13}$$

where $\mathbf{v}_0$ is the peak center, and w_f and w_g are fitting parameters related to the widths of

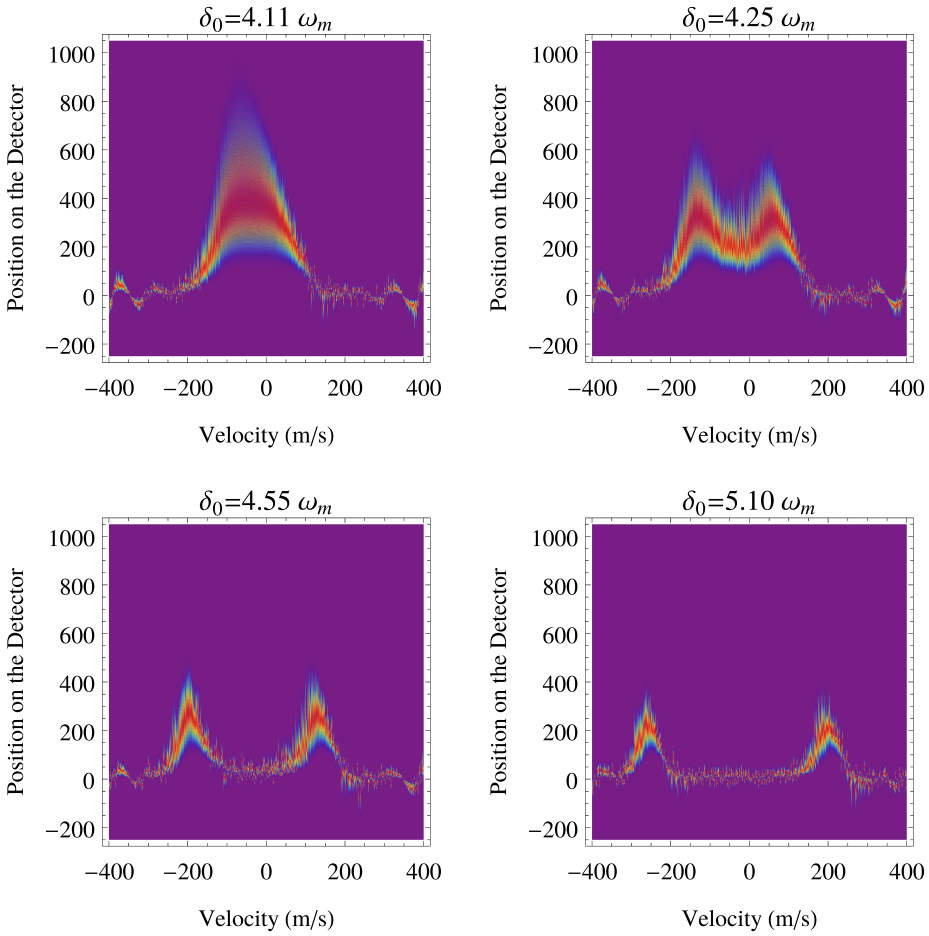

Figure 5.7: Simulation results showing force *vs.* velocity profiles for various values of δ_0 with spontaneous emission turned off. The color represents relative atom number, where red corresponds to more atoms and violet to less atoms. The interesting feature in these results is the two peak structure whose splitting increases as the value of δ_0 increases.

the peaks. The asymmetric shape of the peaks means that it is not necessary for w_f and w_g to have the same value. Although a physical explanation for these shapes is not known at the present, the fit is qualitatively good and provides an unbiased way of obtaining the peak location. Both techniques give very similar results. The fitting method is preferred because it requires less judgement on the part of the user.

A plot of the velocity separation between the two peaks ($\Delta\mathbf{v}$) *vs.* δ_0 shows a monotonic trend. Several attempts to fit different functions to the results were made and the best option turned out to be a function of the form $k\Delta\mathrm{v} = \mu\left(\delta_0 - \eta\right)^{1/\xi}$, where μ, η, and ξ are the fitting

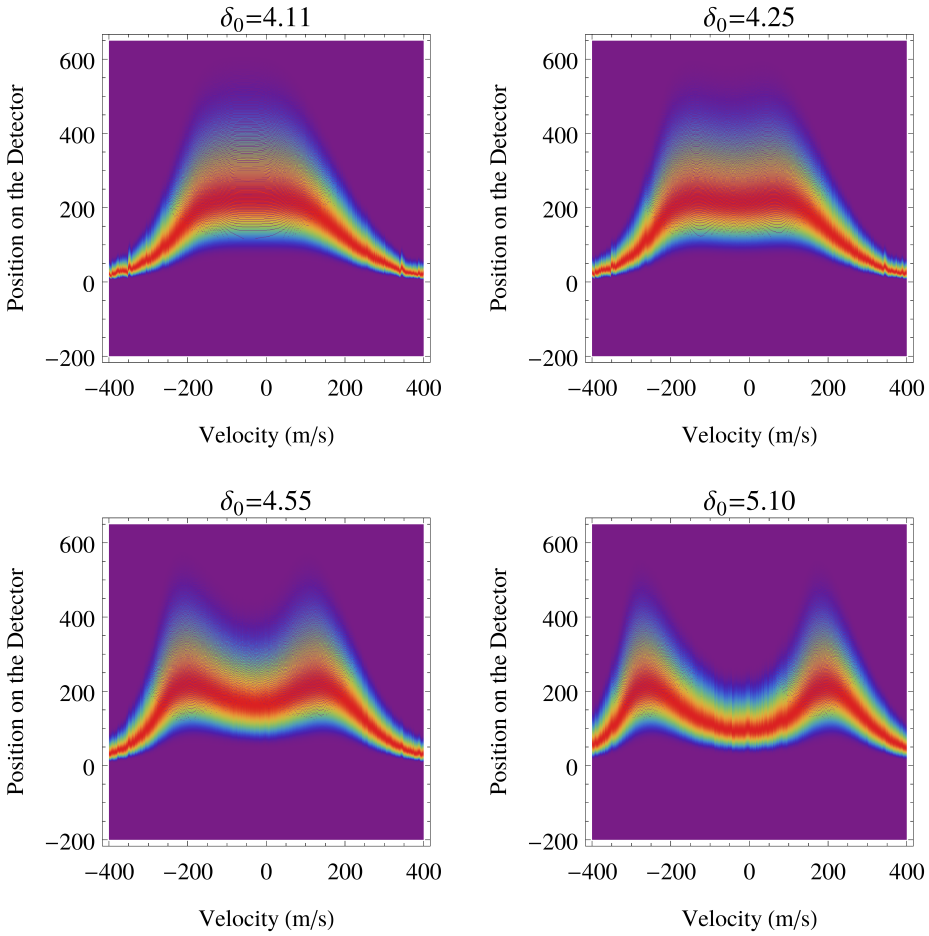

Figure 5.8: Simulation results showing force *vs.* velocity profiles for various values of δ_0 with spontaneous emission included at experimental rate. The color represents relative atom number, where red corresponds to more atoms and violet to less atoms. The interesting feature in these results is the two peak structure whose splitting increases as the value of δ_0 increases.

parameters. Δv is the separation between the peaks, k is the magnitude of the wavevector $2\pi/\lambda$, and δ_0 is the value used in the calculation in units of ω_m. Figure 5.9 shows the fit for a Rabi frequency of $\Omega_0 = 3.37\ \omega_m$ and Table 5.2 gives the values of the fit parameters.

In an attempt to better understand the meaning of the fit, a similar set of calculations was done for Rabi frequencies of 3.27 ω_m and 3.47 ω_m. Just as with the calculations with 3.37 ω_m, δ_0 was varied from 4.0 ω_m to $\approx$ 5.4 ω_m, and the points were fit with a function of the same form. Figure 5.10 shows the three fits all plotted on the same graph and Table 5.2

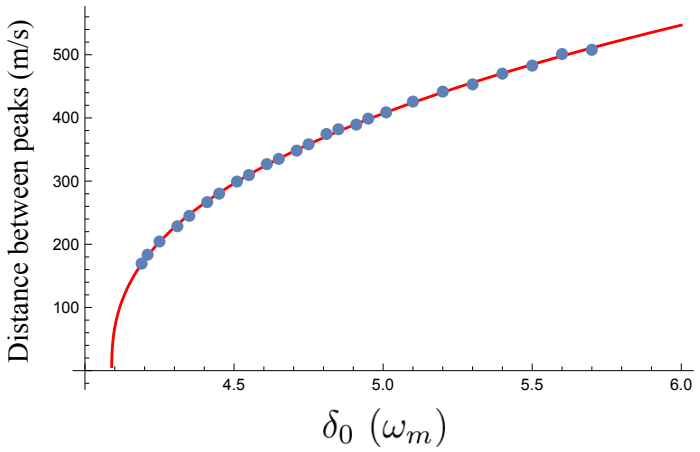

Figure 5.9: A plot of $\Delta\mathbf{v}$ as a function of δ_0 for $\Omega_0 = 3.37\ \omega_m$ and $\gamma = 0$ force *vs.* velocity simulations. The points are the measured splitting in the simulations and the solid line shows the fit of these points using the function $k\Delta\mathrm{v} = \mu\,(\delta_0 - \eta)^{1/\xi}$. The values of μ, η, and ξ are given in Table 5.2.

gives the values of the fit parameters. Based on the small variations in the fit parameters, and the statistics of the fits, it is believed that ξ is a constant $\approx 5/2$. The variation in its value, seen in the three fits is likely due to the difficulty in accurately identifying the peak separation. Also, it would appear that changing the Rabi frequency has only little to no influence on the values of η. This is rather strange because it implies that the splitting in the force profile arises at $\delta_0 \approx 4.1\ \omega_m$ is independent of small changes in the Rabi frequency.

Ω_0 (ω_m)	η (rad/s)	ξ (dimensionless)	μ (rad/s$^{(1/\xi)}$)
3.27	4.11	2.66	435.1
3.37	4.09	2.51	422.5
3.47	4.08	2.42	431.1

Table 5.2: Table of values for the fits shown in Fig. 5.10.

The only explanation that can presently be made about the origins of this phenomenon is that the phase term is playing a more dominant role on the moving atoms than was previously expected.

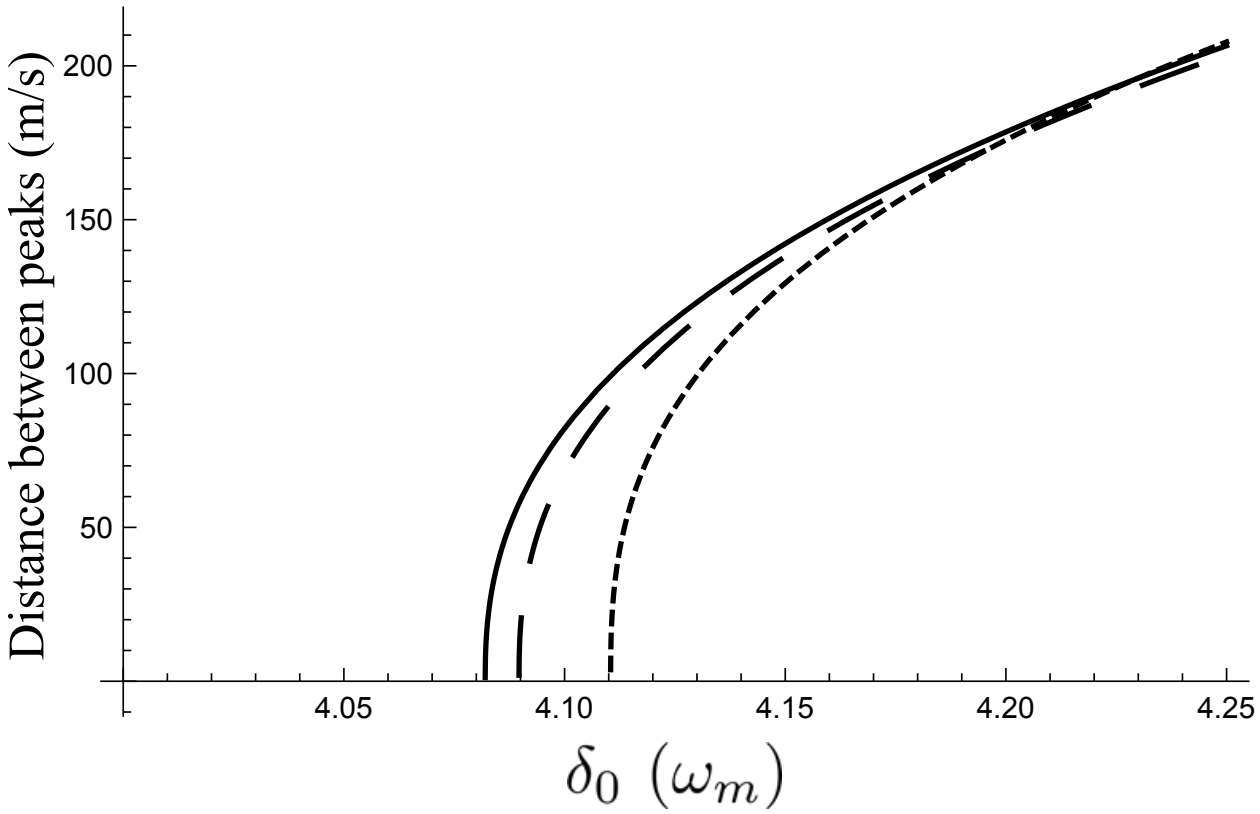

Figure 5.10: Plot of the fits to the peak splitting in the force *vs.* velocity calculation results. The large dashed line is for $\Omega_0 = 3.27\ \omega_m$, the small dashed line for $\Omega_0 = 3.37\ \omega_m$, and the solid line for $\Omega_0 = 3.47\ \omega_m$. The three fits are very similar.

Chapter 6

Experimental Results

In order for an optical force to be suitable for laser cooling, it must have a significant strength at some velocities and vanish at other velocities. For the radiative force, in the low intensity limit, a velocity capture range, $\mathbf{v}_{\text{capture}} \sim \gamma/\mathbf{k}$, is entirely dependent on the properties of the atom. By contrast, our numerical simulations predict that the velocity capture range for the ARP force, $\mathbf{v}_{\text{capture}} \sim \delta_0/\mathbf{k}$, can be orders of magnitude larger than that of the radiative force by choosing $\delta_0 \gg \gamma$ [32]. For this reason, a measurement of the velocity dependence of the ARP force was the ultimate goal of this thesis.

The velocity dependence of the ARP force was not the only piece knowledge gained by these experiments. As the previous chapters have shown, that ARP is a very complicated technique, and several fundamental questions about the physics of the process must be considered. Some of these questions are: Why does the relative phase difference between a pair ARP pulses play such a strong role in determining the final state of the atom? How does the use of multiple ARP sequences compound this phase question? In the case of multiple ARP sequences, how should the role of spontaneous emission (SE) be handled throughout the process? Should the SE clock reset every time the state returns to or passes through the south pole of the Bloch sphere, or does the fact that the process is coherent mean that the clock continues to run throughout the process? Insight into some of these questions has been revealed by the numerical simulations and experimental data, but there is more to be learned about the physics of the ARP process.

6.1 The Velocity Dependence of the ARP Force

The results of the experiments on the velocity dependence of ARP are shown in Fig. 6.1. These plots show the ARP force *vs.* velocity for a fixed Rabi frequency, $\Omega_0 \approx 3.70\ \omega_m$, and various values of δ_0. The plots show the simulated Doppler velocity on the x-axis, and the position the atoms land on the detector (proportional to the force) on the y-axis. The color depicts the atomic density based on the longitudinal velocity distribution (red corresponds to more atoms, while violet corresponds to fewer atoms). The bright line through the middle of the data plots results from UV light from the source passing through the atomic slit along with any undeflected (F = 0) atoms. These plots are similar to the simulation results shown in Figs. 5.7 and 5.8. However, unlike the simulation results, the experimental data fails to show a nice smooth force profile. An investigation into the reason for the difference between the numerical simulations and the experimental results has revealed some surprising results about the importance of the role that the phase, ϕ, plays in the ARP force.

The current iteration of the experiment involves the use of two independent diode lasers to continuously vary the simulated velocity of the atoms. This method was developed because there were concerns that data collection would take too long using a single laser and any drifts in experimental parameters would lead to inconsistency between data sets. However, the use of two independent lasers seems to be the source of the difference between the experimental data and the numerical simulations. Although each of the two lasers has its own very narrow linewidth ($\sim 200\,\mathrm{KHz}$), there is no coherence between them. This is because the lasers are only frequency-locked, not phase-locked to an atomic reference so there is no phase coherence between the ARP pulses in each pulse pair. Based on a simple model of the ARP process, this should not be an issue since the frequency sweep during a pulse is significantly larger than any frequency noise on the locked laser. But, as was seen in Sec. 5.3.2, the relative phase difference between pulses in a pair plays an important role in the strength and behavior of the ARP force. It is believed that the lack of phase coherence between the two pulses is responsible for the unique features and large discrepancy between the experimental results and the numerical simulations. It would appear that whatever the role phase is playing in the ARP process, it is significant enough that it can change the overall velocity dependence of the force. However, it is also revealing that even with these phase-incoherent pulses, the ARP force can still be strong over a large velocity range. The rest of this section will address some of the interesting features of this velocity data.

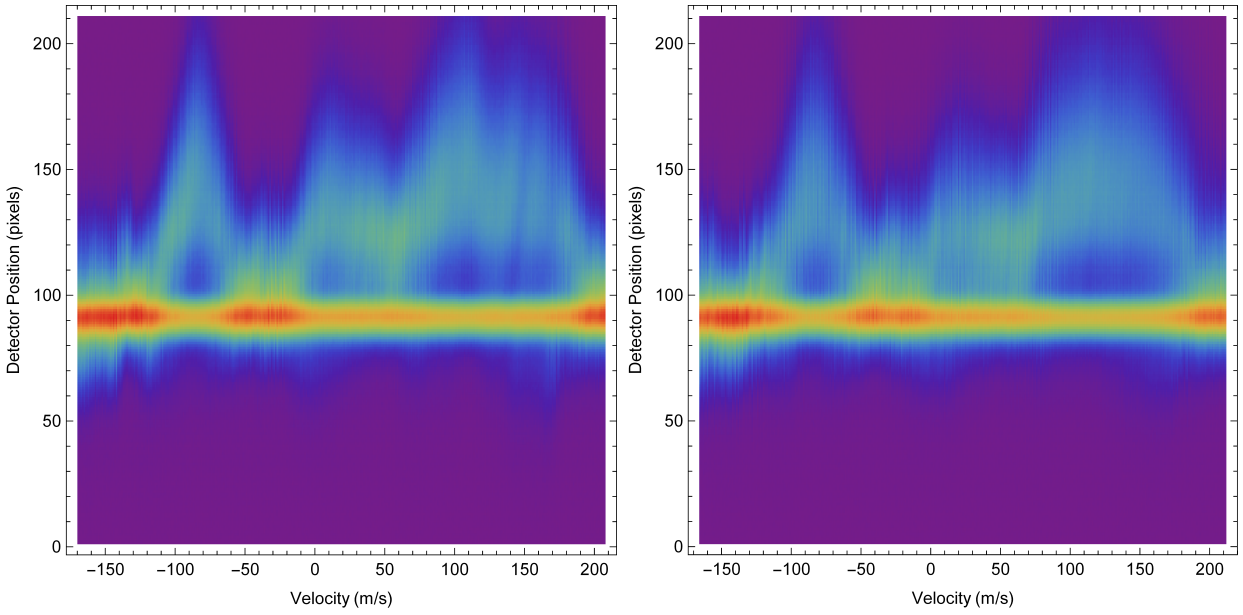

(a) $\delta_0 = 3.25\ \omega_m$

(b) $\delta_0 = 3.25\ \omega_m$

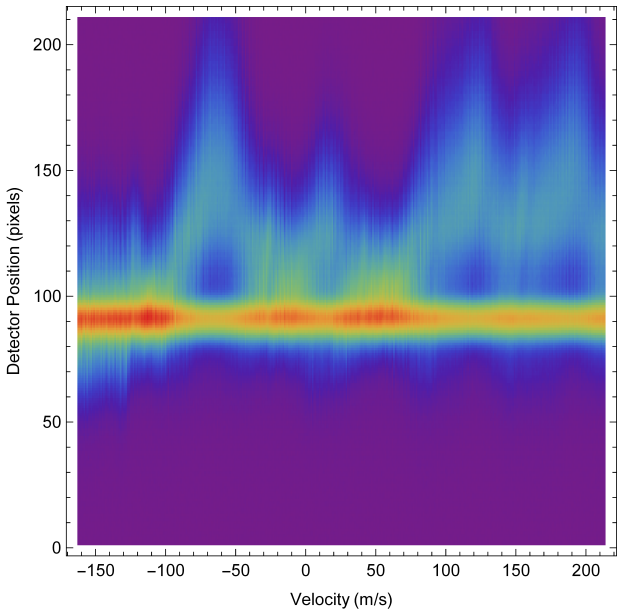

(c) $\delta_0 = 3.50\ \omega_m$

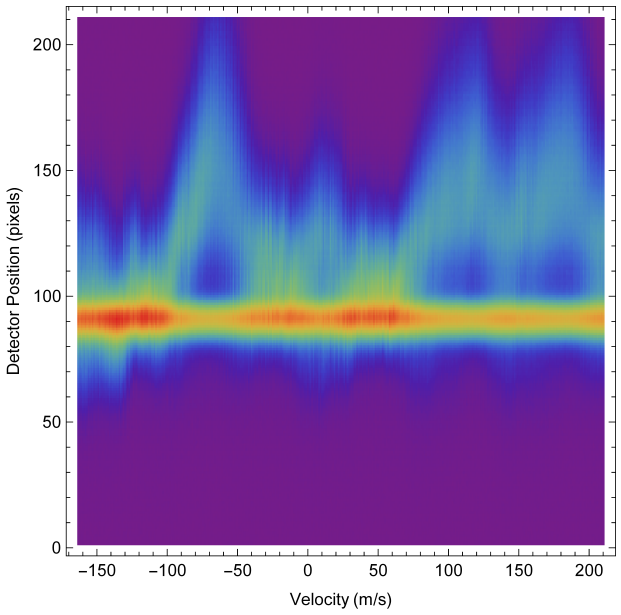

(d) $\delta_0 = 3.75\ \omega_m$

Figure 6.1: Velocity Dependence of the ARP force measured for $\Omega_0 \approx 3.70\ \omega_m$ and various values of δ_0.

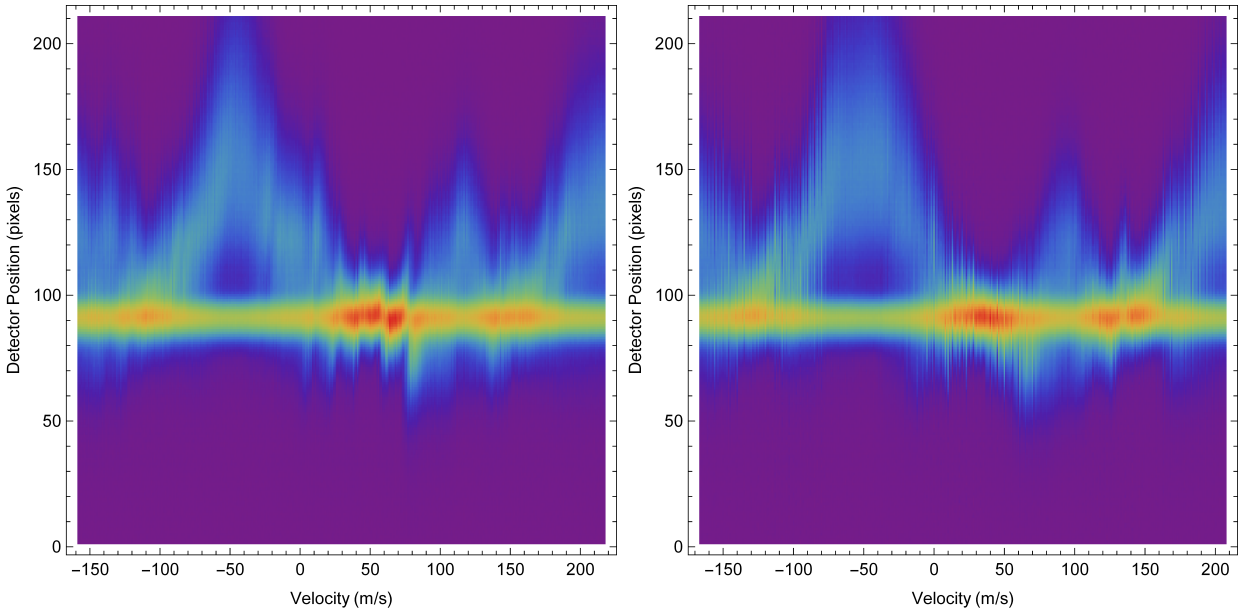

(e) $\delta_0 = 4.00\ \omega_m$

(f) $\delta_0 = 4.25\ \omega_m$

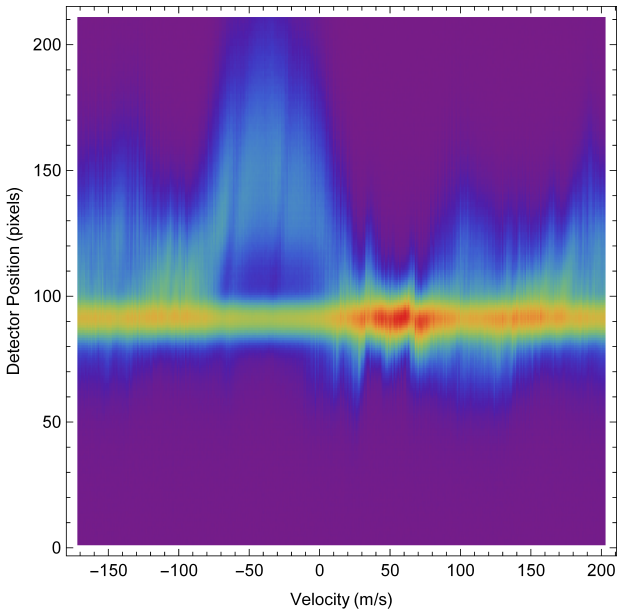

(g) $\delta_0 = 4.50\ \omega_m$

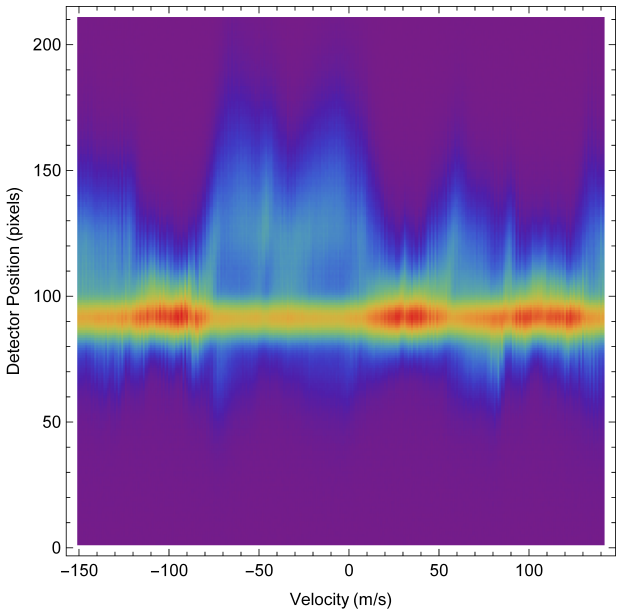

(h) $\delta_0 = 5.00\ \omega_m$

Figure 6.1: Velocity Dependence of the ARP force measured for $\Omega_0 \approx 3.70\ \omega_m$ and various values of δ_0.

6.1.1 Periodic Enhancement

The most obvious feature of the data, shown in Fig. 6.1, is the appearance of an enhanced force for some velocities. Although the significance of these velocities is unknown, the spacing between these enhancements is roughly periodic. The period of the enhancements, when converted to a Doppler frequency, $\mathbf{k}\Delta v = \omega_{\text{Doppler}}$, closely matches the pulse repetition rate of the experiment. Figures 6.1c and 6.1d most clearly show this effect. Peaks occur at $\approx -70\,\text{m/s}$, $\approx 10\,\text{m/s}$, $\approx 100\,\text{m/s}$, and $\approx 185\,\text{m/s}$. For $\Delta v \approx 80\,\text{m/s}$, we find $\mathbf{k}\Delta\mathbf{v} \sim \frac{\omega_m}{2} = 80\,\text{MHz}$ which is the repetition rate of the pulses. As δ_0 is changed, the strength of the force at these velocities changes, but the periodic behavior is present in all cases. This could be experimental support for the claims made in Sec. 5.3.1 which addressed the meaning of the unexpected oscillations seen in the force *vs.* velocity plots of Fig. 5.3.

6.1.2 Strength of the Force

The next aspect of the data to be addressed is the strength of the force. For the experimental parameters, $\omega_m = 100\gamma$ and the value of dead time equal to $2\pi/\omega_m$, the theoretical maximum force should be $32F_{\text{Rad}}$ without the effects of spontaneous emission considered and $\sim 16F_{\text{Rad}}$ with it considered. The work done in Ref. [38] and [23] showed that forces could be measured to be very near the $16F_{\text{Rad}}$ value when using a single laser source, either through the use of retro-reflection or splitting the beam. However, the largest forces seen in the current data, measured by looking at the peak of the atomic distribution for different velocities, is only $\approx 6 - 7F_{\text{Rad}}$. This reduction could mean that the phase incoherence resulting from the use of two independent lasers reduces the strength of the ARP force by ≈ 2. The mechanism by which this reduction occurs is still being investigated.

6.1.3 Forces in the Wrong Direction

The final feature exhibited in the velocity data that will be discussed, is the emergence of forces in the wrong direction, or negative forces. This is seen in the data as atoms which are below the bright line image of the atomic slit. The emergence of negative forces is seen in some of the simulation results, and arises from the relative phase differences between the ARP pulses. However, in all of these cases shown in Chapter 5, the simulations were run in the absence of spontaneous emission. To see negative forces in experimental data is a

rather surprising result. This raises, the question of whether the multiple ARP sequences somehow influence the decay rate of the atoms. This result provides further impetus answer the questions about the proper treatment of the spontaneous emission clock during multiple ARP sequences.

6.2 Future Outlook

To date the ARP force experiments have shown that there is a velocity dependence of the ARP force and that the ARP force is a strong force. However, the current experimental results are limited by the phase incoherence of the pulse pairs. There does not appear to be a well defined pattern of how the force *vs.* velocity profile will behave, and there is a large disconnect between the current theory and these experimental results. Because of this, plans have been set in motion to upgrade the experimental apparatus with the ultimate goal to better measure the velocity dependence of ARP and also seek answers to many of the more fundamental questions about ARP.

6.2.1 Laser Upgrade

The plans for the laser upgrade are centered around establishing a phase coherence between the two lasers that produce the ARP pulses. There are at least two proposed ways to do this. The first involves using a single laser, splitting the power and making use of a complex optical scheme to properly simulate the Doppler shift. The advantage of this approach is that, in using a single laser, there is no concern that the phase coherence of the pulses is not good enough. However, it does require significant work on the optical setup, and laser power will definitely be a concern.

The second method is to use two lasers, as in the current setup except that the lasers will be phase-locked. Because the goal will still be to measure the velocity dependence of the ARP force, it will be necessary to vary the detuning of the lasers, just as it is in the current setup. This method has the advantage of making use of the current optical setup and as such eliminates the concern about optical power. Its downside is that the degree of phase coherence will depend on how well the lasers can be phase-locked together.

Our plan is to implement the scheme based on the two phase locked lasers. We will use a master laser and two slave lasers; the master laser will be frequency-locked to the

$2^3S_1 \rightarrow 2^3P_2$ atomic resonance just as the lasers in the current experiment are, and the two slave lasers will be phase-locked to the master laser. A pair of TOPTICA DL100 lasers have been purchased and will serve as the slave lasers, while one of the current DBR lasers will serve as the master laser. To help stabilize the master laser and narrow its linewidth, the extended cavity configuration will be changed in accordance with the design used in Ref. [47]. Each of the slave lasers will be phase-locked to the master, one above resonance and the other below, through the use of two TOPTICA mFALC 110 phase lock boxes.

6.2.2 Optical System Changes to Search for SE Reduction

The experimental results presented above show what might be a reduction in the spontaneous emission decay rate for atoms which experience multiple ARP sequences. This could be a very significant result and needs experimental confirmation, and we are planning to do this. Since spontaneous emission is hard to measure directly, we will modify the experiment such that the number of spontaneous emission events can be varied. This can be done by changing the atom-laser interaction time, by varying the size of the optical beams. In the current configuration the 4 mm interaction length is as small as the experimental design will allow without having to deal with diffraction effects. Therefore we want to change the optical collimation lines so that they will properly image a variable slit onto the atoms, thereby providing significantly more control over the interaction length/time and hopefully revealing answers as to whether or not spontaneous emission is suppressed during multiple ARP sequences.

6.3 Conclusions

This thesis has shown that ARP is able to produce large optical forces ($\sim 6 - 7F_{\mathrm{Rad}}$) over a large velocity range ($\sim$ Several hundred m/s). Our results were achieved through the use of two independent diode lasers, asynchronously swept through atomic resonance to simulate a Doppler shift on metastable Helium atoms. The force values differ from the theoretically expected values mainly due to phase incoherence between the pulses in a pair. (Experimental difficulties may also play a role in this reduction.) However, even with this phase incoherence, forces were measured showing how robust the ARP process really is. Future plans have been laid to try and further overcome these difficulties by removing the phase coherence problem;

to improve understanding of the physics of the ARP process.

The numerical simulations and experimental results have, along with aiding in the understanding of the ARP force, also posed many fundamental questions about adiabatic rapid passage. These questions have pertained mostly to how to deal with a two-level system under multiple ARP sequences and the role played by spontaneous emission in the process. Answers to a few of these questions have been provided, but as of now, many of the fundamental physics questions remain unanswered.

Bibliography

[1] C.E. Wieman. The creation of bose-einstein condensation in a cold vapor. 46(S6):2923–2927, 1996.

[2] M.H. Anderson, J.R. Ensher, M.R. Matthews, C.E. Wieman, and E.A. Cornell. *Science*, 269(5221):198–201, 1995.

[3] W. Ketterle, M.R. Andrews, K.B. Davis, D.S. Durfee, D.M. Kurn, M.O. Mewes, and N.J. Vandruten. Bose-einstein condensation of ultracold atomic gases. T66:31–37, 1996.

[4] C.C. Bradley, C.A. Sackett, J.J. Tollett, and R.G. Hulet. Evidence of bose-einstein condensation in an atomic gas with attractive interactions. 75(9):1687–1690, 1995.

[5] T. Hänsch and A. Schawlow. *Op. Comm.*, 13(1):68–71, 1975.

[6] D. Wineland and W. Itano. *Phys. Rev. A*, 20(4):1521–1540, 1979.

[7] W. Phillips and H. Metcalf. *Phys. Rev. Lett.*, 48(9):596–599, 1982.

[8] S. Chu and C. Wieman. Laser cooling and trapping of atoms. 6(11):2020–2020, 1989.

[9] S. Chu, L. Hollberg, J. Bjorkholm, A. Cable, and A. Ashkin. *Phys. Rev. Lett.*, 55(1):48–51, 1985.

[10] P. Lett, R. Watts, C. Westbrook, W. Phillips, P. Gould, and H. Metcalf. Observation of atoms laser cooled below the doppler limit. 61(2):169–172, 1988.

[11] M. Cashen and H. Metcalf. Optical forces on atoms in nonmonochromatic light. *J. Opt. Soc. Am. B*, 20:915, 2003.

[12] M. Williams, F. Chi, M. Cashen, and H. Metcalf. Bichromatic force measurements using atomic beam deflections. 61:023408, 2000.

[13] Andrew Chieda, Michael and E E Eyler. Bichromatic slowing of metastable helium. *Physical Review A*, 86(5):053415, 2012.

[14] X. Miao, E. Wertz, M. G. Cohen, and H. Metcalf. *Phys. Rev. A*, 75:011402, 2007.

[15] M A Chieda and E E Eyler. Prospects for rapid deceleration of small molecules by optical bichromatic forces. *Physical Review A*, 84(6):063401, 2011.

[16] M.T. Hummon J.V. Porto A.M. Jayich, A.C. Vutha and W.C. Campbell. Continuous all-optical deceleration and single-photon cooling of molecular beams. *Physical Review A*, 89(2):023425, 2014.

[17] H.J. Metcalf and P. van der Straten. *Laser Cooling and Trapping*. Springer-Verlag, New York, 1999.

[18] C. S. Corder. *Optical Forces on Metastable Helium. PhD. Dissertation*. PhD thesis, Stony Brook University, 2014.

[19] H. Metcalf and P. van der Straten. Cooling and trapping of neutral atoms. 244(4-5):204–286, 1994.

[20] C.J. Foot. *Atomic Physics*. Oxford University Press, New York, 2005.

[21] L. Allen and J.H. Eberly. *Optical Resonance and Two-Level Atoms*. Dover, New York, 1987.

[22] R. Feynman, F. Vernon, and R. Hellwarth. Geometrical representation of the schrödinger equation for solving maser problems. 28(1):49–52, 1957.

[23] X. Miao. *Optical Forces on Atoms with Periodic Adiabatic Rapid Passage Sequences. PhD. Dissertation*. PhD thesis, Stony Brook University, 2006.

[24] J. Söding, R. Grimm, Yu.B. Ovchinnikov, P. Bouyer, and C. Salomon. *Phys. Rev. Lett.*, 78(8):1420–1423, 1997.

[25] R. Grimm, G. Wasik, J. Söding, and Yu.B. Ovchinnikov. In A. Aspect, W. Barletta, and R. Bonifacio, editors, *Proceedings of the Fermi School CXXXI*, page 481, Amsterdam, 1996. IOS Press.

[26] A. Goepfert, I. Bloch, D. Haubrich, F. Lison, R. Schütze, R. Wynands, and D. Meschede. *Phys. Rev. A*, 56(5):R3354–R3357, 1997.

[27] M. Cashen. *Optical Forces on Atoms in Polychromatic Light Fields*. PhD thesis, Stony Brook University, 2002.

[28] C. Corder, B. Arnold, and H. Metcalf. Laser cooling without spontaneous emission. *Physical Review Letters*, 114:043002, 2015.

[29] J. Reeves. *Neutral Atom Lithography Using the 389 nm Transition in Metastable Helium*. PhD thesis, Stony Brook University, 2010.

[30] A. Abragam. *The Principles of Nuclear Magnetism*. Oxford Univ. Press, Oxford, 1961.

[31] D. Sawicki and J. H. Eberly. Perfect following in the adiabatic limit. *Optics Express*, 217(4), 1999.

[32] Daniel Stack, John Elgin, Petr M. Anisimov, and Harold Metcalf. Numerical studies of optical forces from adiabatic rapid passage. *Phys. Rev. A*, 84:013420, 2011.

[33] P. Ehrenfest. Bemerkung über die angenäherte gültigkeit der klassischen mechanik innerhalb der quantummechanik. 45:455, 1927.

[34] S. S. Hodgman, R. G. Dall, L. J. Byron, K. G. H. Baldwin, S. J. Buckman, and A. G. Truscott. *Phys. Rev. Lett.*, 103:053002, 2009.

[35] H. Metcalf and P. van der Straten. *Laser Cooling and Trapping*. Springer, 1999.

[36] J. Kawanaka, M. Hagiuda, K. Shimizu, F. Shimizu, and H. Takuma. 56(1):21–24, 1993.

[37] H. Mastwijk. *Cold Collisions of Metastable Helium Atoms*. PhD thesis, Utrecht University, 1997.

[38] D. Stack. *Optical Forces from Periodic Adiabatic Rapid Passage Sequences on Metastable Helium Atoms. PhD. Dissertation*. PhD thesis, Stony Brook University, 2012.

[39] C. Avila. Spectral control of a 1083 nm diode laser. Master's thesis, Stony Brook University, 1998.

[40] C.E. Wieman and L. Hollberg. *Rev. Sci. Instrum.*, 62:1–20, 1991.

[41] M. Prevedelli, P. Cancio, G. Giusfredi, F.S. Pavone, and M. Inguscio. *Opt. Comm.*, 125:231–236, 1996.

[42] A. Yariv. *Optical Electronics in Modern Communications*. Oxford University Press, New York, 1997.

[43] B.E.A. Saleh and M.C. Teich. *Photonics*. Wiley, Hoboken, 2007.

[44] C.R. Ekstrom, C. Kurtsiefer, D. Voigt, O. Dross, T. Pfau, and J. Mlynek. Coherent excitation of a he* beam observed in atomic momentum distributions. 123:505, 1996.

[45] T. Lu, X. Miao, and H. Metcalf. *Phys. Rev. A*, 75:063422, 2007.

[46] This can be found at http://www.math.unifi.it/ brugnano/BiM/index.html. It is written especially for stiff, ordinary differential equations and is quite fast and efficient.

[47] Qian Lin, Mackenzie A. Van Camp, Hao Zhang, Branislav Jelenković, and Vladan Vuletić. Long-external-cavity distributed Bragg reflector laser with subkilohertz intrinsic linewidth. *Optics Letters*, 37(11):1989, 2012.